

**Experimental Investigation of Photonic Mixer Device and
Development of TOF 3D Ranging Systems Based on PMD
Technology**

A dissertation submitted to the
**DEPARTMENT OF ELECTRICAL ENGINEERING AND
COMPUTER SCIENCE AT UNIVERSITY OF SIEGEN**

for a degree of
DOCTOR OF TECHNICAL SCIENCES

presented by
Xuming Luan
from Shandong, China

Siegen, November 2001

**Experimentelle Untersuchungen des Photomischdetektors
(PMD) und Entwicklung der PMD-basierten 3D TOF-
Entfernungsmesssysteme**

Vom Fachbereich Elektrotechnik und Informatik
der Universität Siegen
zur Erlangung des akademischen Grades

Doktor der Ingenieurwissenschaften (Dr.-Ing.)

Genehmigte Dissertation

vorgelegt von

Xuming Luan

geboren am 08.07.62 in Shandong, VR China.

1. Gutachter: Prof. Dr.-Ing. Rudolf Schwarte
2. Gutachter: Prof. Dr.-Ing. Hubert Roth

Tag der mündlichen Prüfung: 22. 11. 2001

To my family

Acknowledgments

This work has been carried out in the institute for signal and data processing at the University of Siegen. First of all, I would like to express all my gratitude to the supervisor of my doctoral thesis: **Prof. Rudolf Schwarte** for giving me this opportunity to do Ph.D. studies under his guidance. His engagement, scientific knowledge, encouragement and continuous support during the past years were crucial not only for the accomplishment of this work, but also for the expansion of my scientific knowledge and my growing interest in the world of Photonics.

I would especially like to thank Dr. Horst G. Heinol and Dr. Zhanping Xu for their personal support, numerous constructive discussions, and valuable suggestions.

I would to express my special thank to Dr. Jürgen Schulte and Zhigang Zhang for all the nice discussions and successful cooperation during the years.

I want to gratefully thank Bernd Buxbaum and Thorsten Ringbeck for their valuable suggestions and for all their technical support.

I especially appreciate Dr. Christos Geogiadis, Dr. Stephan Hußman, Dr. Detlef Justen, Mathias Koscheck, Thomas Krieger, Holger Hess and Jens Fricke for all kinds of help in analog and digital electronic problems during the realization of PMD ranging systems.

I would not forget Arne Stadermann for giving me all the technical support during the time and Margarethe Pufahl for her contribution to the performance of my work.

I would like to thank all my friends and colleges of the institute and the Zentrum für Sensorsysteme (ZESS) for the nice working atmosphere, a steady important factor supporting me to finish this work.

Finally, I want to thank my parents, especially my wife Yuan and my son Siyang for their contribution in every aspect along the years. Without their support it won't be possible for me to finish this work.

Content

CONTENT	I
ABSTRACT	III
KURZFASSUNG.....	V
1 INTRODUCTION.....	1
2 THE OPTICAL 3D MEASUREMENT SYSTEMS.....	4
2.1 OVERVIEW OF 3D OPTICAL MEASUREMENT	4
2.1.1 <i>Triangulation</i>	5
2.1.2 <i>Interferometry</i>	7
2.1.3 <i>Time-of-flight</i>	9
2.1.4 <i>Discussion</i>	11
2.2 TIME OF FLIGHT (TOF) 3D MEASUREMENT SYSTEMS WITH CW-MODULATION	13
2.2.1 <i>Operation principle of the 3D TOF systems</i>	13
2.2.2 <i>Phase shifting technique (homodyne mixing method)</i>	16
2.2.3 <i>3D-data evaluation algorithms</i>	20
3 PHOTONIC MIXER DEVICE (PMD).....	23
3.1 GENERAL DESCRIPTION OF PMD PRINCIPLE	24
3.2 PMD CHARGE TRANSFER PROCESS	26
3.3 TRANSFER CHARACTERISTIC AND FREQUENCY LIMITATIONS OF THE PMD	29
3.4 READOUT TECHNIQUE OF PMD	30
3.5 MEASUREMENT OF THE PHASE AND TOF INFORMATION USING PMD.....	33
4 CHARACTERIZATION OF PMD PIXEL PERFORMANCE	37
4.1 MEASUREMENT SETUP, EXPECTATIONS AND PREDICTIONS	37
4.2 THE SPECTRAL RESPONSIVITY	40
4.3 TRANSFER CHARACTERISTIC OF PMD	42
4.4 MODULATION CONTRAST AND DYNAMIC RANGE OF PMD.....	44
4.4.1 <i>Frequency characteristic of PMD</i>	45
4.4.2 <i>Influence of the optical intensity on the PMD performance</i>	46
4.4.3 <i>The correlation characteristic of PMD</i>	48
4.4.4 <i>Lateral effect and unsymmetrical modulation of PMD</i>	50

4.4.5	<i>Noise performance and dynamic range</i>	52
4.5	INFLUENCE OF THE BACKGROUND ILLUMINATION.....	54
4.6	NON-LINEARITY MEASUREMENT.....	56
4.7	CORRELATED BALANCE SAMPLING (CBS).....	58
5	3D-IMAGING CAMERAS BASED ON PMD	64
5.1	SYSTEM ARCHITECTURE OF THE PMD RANGING CAMERAS.....	64
5.1.1	<i>Optical modulation unit</i>	65
5.1.2	<i>PMD front end module</i>	67
5.1.3	<i>Phase shifting unit</i>	67
5.1.4	<i>Timing control and data processing module</i>	68
5.2	OPTICAL ASPECT OF ILLUMINATION.....	69
5.3	PHASE SHIFT TECHNIQUE.....	71
5.3.1	<i>DDS</i>	71
5.3.2	<i>Fixed phase shifting generation</i>	81
5.3.3	<i>Phase jitter consideration</i>	82
5.3.4	<i>Summary</i>	84
5.4	DATA PROCESSING.....	84
5.4.1	<i>Frame synchronization and data buffering</i>	86
5.4.2	<i>Distance evaluation algorithm</i>	89
5.4.3	<i>Data filtering and thresholding</i>	90
5.4.4	<i>Sub-sampling technique and adaptive integration control</i>	93
5.5	2D RANGE MEASUREMENT.....	96
5.6	3D RANGE MEASUREMENT.....	101
6	THE MEASUREMENT ACCURACY AND ERROR COMPENSATION	106
6.1	DISTANCE ACCURACY OF THE SYSTEM.....	106
6.2	DISTANCE REFERENCE TECHNIQUE.....	109
6.3	NON-LINEARITY ERROR AND PHASE SHIFTING EVALUATION.....	111
6.4	3D DATA CALIBRATION.....	113
6.5	SMEARING EFFECT AND THE DEPTH OF FIELD.....	116
6.6	DISCUSSION.....	118
7	SUMMARY AND PERSPECTIVE	119

Abstract

With permanently increasing demand for 3D-data acquisition and inspection in the industry more and more new 3D ranging systems have been developed. As one of the most important measurement techniques, the 3D-ranging systems based on time-of-flight (TOF) principle are nowadays intensively investigated. Despite of a large variety of 3D TOF ranging system concepts, the growing requirements in applications for 3D-vision have seldom been really satisfied. Either additional 2D spatial scanning must be used in order to obtain the 3D information, resulting low data acquisition rate and low lateral resolution, or their applications are restricted due to the critical requirements on the operation condition, the system complexity or their high cost.

As the key component of a 3D non-scanning TOF ranging system, the novel Photonic Mixer Device (PMD) realized based on the standard CMOS technology, has won intensive, widespread interest from various sides since its appearance in 1997. The unique and astonishing features of PMD, and its easy integration into a sensing array and the flexible arrangement make the realization of extremely fast, flexible, robust and low cost smart 3D solid-state ranging cameras possible.

In this thesis, the experimental investigation of the PMD device was carried out, based on the results of the preceding researches about PMD. A series of properties of PMD device such as the charge transfer characteristic, modulation contrast, noise performance and non-linearity problem etc., as well as the operation performances of different PMD structures were already measured and analysed, which offers an experimental basis for the further optimization in the PMD chip design.

Based on the actually fabricated single PMD chips, we developed the first generation of smart 3D PMD ranging cameras. Without any special expensive system techniques, the implemented system has achieved a ranging accuracy in the order of millimetres, at a modulation frequency of just 20MHz. Because of the outstanding features of PMD device in the electro-optical mixing process, the ranging system based on PMD technology overcomes the typical drawbacks in the conventional time-of-flight measurement techniques and considerably simplifies the system design without any loss of measurement accuracy. Among the possible applications of PMD, this work

treats only the use of PMD in the 3D data acquisition. We believe that with the continuous development of the modern semiconductor technology and further improvement of PMD performance, the PMD will find more and more applications in different areas of the industry in the near future.

Kurzfassung

In der industriellen Fertigung besteht ein derzeit stark wachsender Bedarf nach schnellen, präzisen und berührungslosen optischen 3D-Vermessungssystemen u.a. zur mehrdimensionalen Objekterkennung zur Qualitätsprüfung, Robotvision zur Automatisierung und zur Sicherheitsüberwachung kritischer Fertigungsbereiche. In den letzten Jahren wurden viele neue Messkonzepte zur 3D-Formerfassung auf Basis des Laufzeitverfahrens mit inkohärentem Licht (TOF-Verfahren – Time of Flight) entwickelt und untersucht. Der Stand der 3D-Meßtechnik auf dieser technologischen Grundlage besteht derzeit entweder in der räumlichen Abtastung der 3D-Szene mit einem einzelnen Lichtstrahl über einem hochpräzisen xy-Spiegelscanner, oder in der Kombination von CCD-Kameras mit 2D-EO-Modulatoren zur flächigen Demodulation der empfangenen Reflexionswelle (z.B. mit Pockelszellen). Typische Nachteile solcher Ansätze sind die u.a. die aufwendige Nachverarbeitung der gewonnenen Datensätze, die kritischen Anforderungen an die Applikationsbedingung sowie sehr hohe Kosten. Daher ist der Einsatz solcher Systeme bisher in vielen möglichen Anwendungsfällen nur vergleichsweise selten erfolgt.

Als Schlüsselkomponente in einem neuartigen 3D-TOF-Formerfassungssystem ermöglicht der sogenannte Photomischdetektor PMD die Realisation schneller, flexibler, robuster und hochauflösender 3D-Solid-State-Kameras. Die einzigartigen PMD-Features eliminieren die Hauptfehlerquellen konventioneller Ansätze, und bieten auch deutliche Vorteile hinsichtlich Robustheit und Preis.

Im ersten Teil der vorliegenden Arbeit ist im Wesentlichen die umfangreiche experimentelle Untersuchung und Spezifikation von PMD-Sensoren, insbesondere zur fortschrittsgemäßen Optimierung des Chipdesigns, dokumentiert. Es wurde die DC-Übertragungsfunktion und die Sensordynamik, sowie das AC-Modulationsverhalten unterschiedlicher PMD-Strukturen unter verschiedenen Arbeitsbedingungen (d.h. Modulationsfrequenz, Photostrom und Hintergrundbeleuchtung) intensiv untersucht.

Im zweiten Teil der Arbeit werden realisierte PMD-Entfernungsmesssysteme, basierend auf unterschiedlichen PMD-Testsamples, systematisch vorgestellt. Es wird u.a. dargestellt, wie der Aufbau eines PMD-basierten Entfernungsmesssystems enorm

vereinfacht werden kann, da die einzigartigen PMD-Eigenschaften die teuren und fehleranfälligen HF-Komponenten konventioneller Ansätze ohne zusätzlichen Mehraufwand ersetzen. Wie in den Messungen gezeigt werden konnte, sind Genauigkeiten im mm-Bereich ohne weiteres zu erreichen. Es ist zu erwarten, dass mit der Weiterentwicklung der PMD-CMOS-Technologie und adäquater Optimierung des Chipdesigns, zukünftig viele neue Einsatzgebiete der PMD-Sensorik in verschiedensten Anwendungen gefunden werden.

1 Introduction

With the rapid development of the technology nowadays, different types of solid-state imaging sensors, such as CCD (Charged Coupled Device) and CMOS cameras [Boy][Fos][Vie], satisfying requirements in different applications, have been developed. It is obvious that although the imaging sensors can offer images with high lateral resolution, they can see only radiance and color, not the depth information of the scene.

Most applications in industrial measurement and inspections, localization and reorganization, reverse engineering and virtual reality, however, require not only data about the 2D-geometrical features but also shape information of objects in 3D-space. The 3D-data are, compared to the 2D-information obtained by imaging sensors, invariant against rotation and motion of objects, alteration of illumination and soiling. To satisfy the requirement mentioned above, enormous efforts have been made in the development of 3D optical sensors. Based on the measurement principle of sensors and the limitations of measuring uncertainty, 3D optical ranging systems can be classified in general into following three main categories: triangulation, time-of-flight and interferometry [Scw-2].

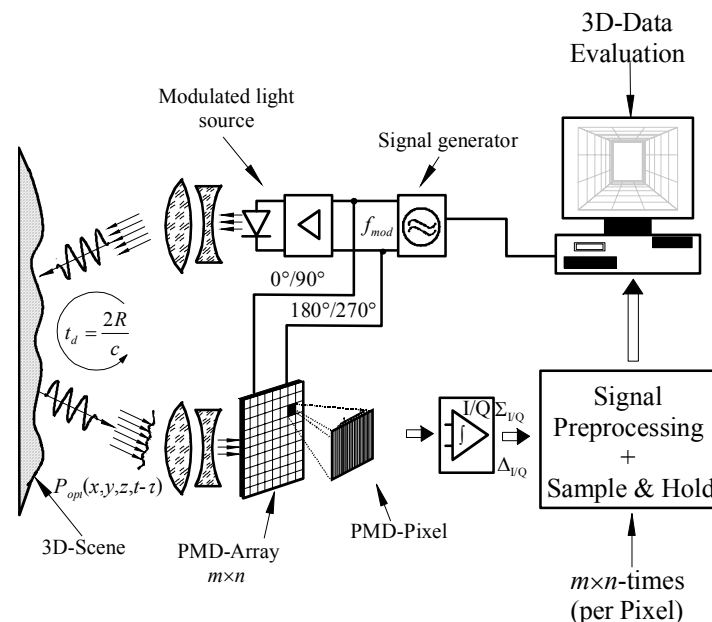


Fig. 1.1 Block diagram of 3D TOF ranging systems based on PMD sensing array

Time-of-flight (TOF) ranging is one of the most widely used techniques for optical 3D measurement. The distance to the object or the depth information d can be determined by the echo time τ of the modulated light signal back scattered from the object which yields

$$d = \frac{c \cdot \tau}{2}$$

where $c = 3 \times 10^8$ m/s represents the transmitting velocity of the light signal in the median. In stead of using spatial scanning at 1D/2D ranging sensors to get the required whole 3D information, a variety of non-scanning 3D-ranging systems based on the TOF techniques with CW-modulation have been developed to satisfy the increasing demands for 3D ranging applications in the industry.

The key component of such 3D TOF ranging systems is the 2D electro-optical modulator or mixer (EOM) which in principle mixes the RF-modulated optical wave front reflected from the target scene with the reference signal, resulting a RF-interferometry. Typical examples among 3D ranging systems are the CCD-array combined with 2D-EO modulator such as Pockels cells or image intensifier [Scw-2][Höf][He-1][Xu-1]. The main drawbacks of these systems, e.g. high operation voltage (up to 1000V), relative lower modulation depth, dependence of the angle of view and of the optical wavelength as well as higher cost and system complexity limit the applications in the industry. A new novel electro-optical mixer – **Photonic Mixer Device (PMD)** based on the CMOS technology – opens a fully new aspect in the 3D measurement [Scw-3]. This concept is based on the creative idea of Prof. R. Schwarte, on the institute of signal processing, Zentrum fuer Sensorsysteme (ZESS) and later on S-TEC GmbH since 1997. The PMD device offers a high potential for optical sensory systems due to the simple and powerful procedure of electro-optical mixing and correlation. With the advantage of easy integration of PMD pixels into a PMD line or a PMD sensing array, this new concept presents a very attractive solution for realization of fast, robust and low cost 3D solid-state sensors [He-2][Xu-1]. It is to expect that with its continuous development, the PMD device will find more and more applications in the near future. **Fig. 1.1** shows the block diagram of the 3D TOF ranging camera based on the PMD technology.

This dissertation is aimed at the investigation of the performance and correlation characteristics of different PMD structures with regard to real application conditions in the optical measurement as well as the realization of the first 3D PMD ranging system, using the phase shifting CW-modulation technique, based on the actual fabricated PMD samples.

This work is arranged into five main sections. We begin with an overview of the different non-contact optical measurement solutions and discussions about the 3D TOF measurement based on the phase shifting modulation technique (homodyne mixing method) in chapter two, followed by the functional description of PMD device in chapter three. In chapter four we report the PMD specification. The measured results of single PMD structures from different processes under various operation conditions are presented. And finally, we describe the realizations of 1D-, 2D- as well as 3D-PMD TOF-ranging systems based on the different actual fabricated engineering PMD examples in chapter five. The measurement results are presented as well. And the main factors influencing the distance accuracy and measurement errors are discussed in the last chapter of this work.

2 The optical 3D measurement systems

2.1 Overview of 3D optical measurement

The most important optical 3D range measurement techniques can be divided into the following three categories: (1) triangulation, (2) time-of-flight and (3) interferometry. In order to obtain the depth information of the objects, most of these methods require the active scene illumination, which covers the light wavelength generally from 400 to 1000 nm, i.e. visible and NIR spectrum. **Fig. 2.1** gives a hierarchical description of the non-contact 3D measurement techniques [Scw-1].

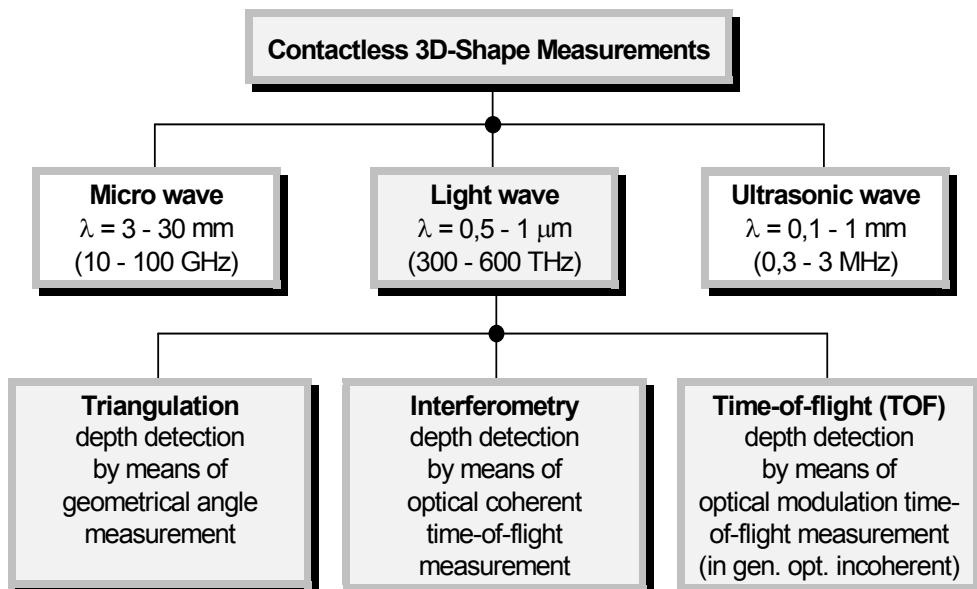


Fig. 2.1 Family tree of non-contact 3D measurement techniques [Scw-1]

Of course there can be found a lot of applications that use microwave ($\lambda = 3\sim 30\text{mm}$) and ultrasonic wave ($\lambda = 0.1\sim 1\text{m}$) techniques (e.g. differential GPS, microwave radar and SAR interferometry). However, both measurement techniques are due to their diffraction limitations not suitable for range measurements with high angular resolution.

In this section we give first a rough description of fundamental principle of the optical measurement techniques of three categories mentioned above and some examples related to each principle. The advantages and disadvantages of these principles will be then discussed. More detailed discussions and broader overviews over optical 3D

object measurement technique can be found in the references [OFHB] [Bre] [Eng] [Scw-1].

2.1.1 Triangulation

We start with the triangulation technique. It is a very common ranging technique used by the nature. As illustrated in **Fig. 2.2** and **Fig. 2.3**, the triangulation measurement technique is in principle a geometrical method. One point of the object surface and other two points of the measurement system together build a geometrical triangle. It is uniquely defined if the angles α and β and the baseline b are all known. The distance of the target from the observation point can then be determined by measuring the triangle's angles or the triangulation base.

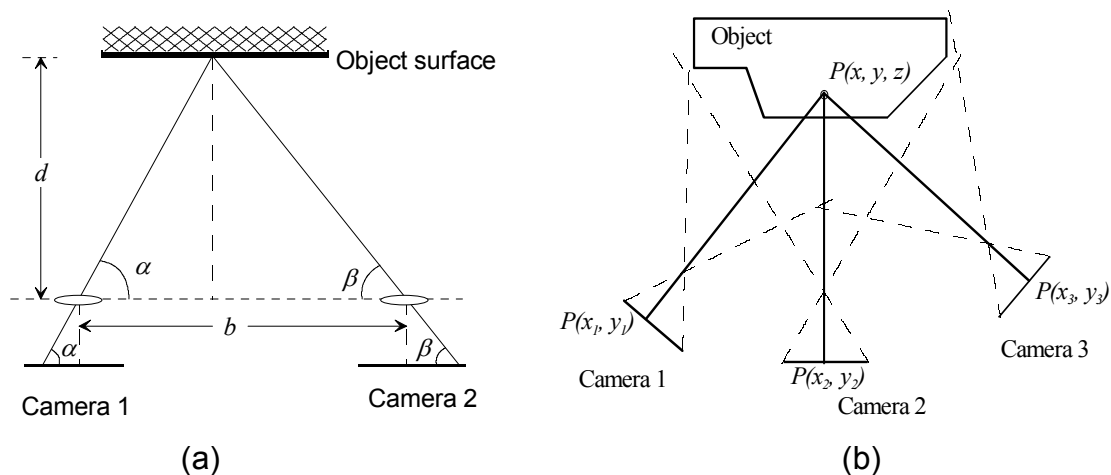


Fig. 2.2 Principle of passive triangulation measurement.

The principles of the triangulation technique are normally divided into two groups: passive and active triangulation methods. Digital photogrammetry and Theodolite systems belong to the passive triangulation technique. Observing the same point from two different points A and B with known distance b , and measuring the observing angles α and β , the distance to the observed point d can thus be obtained using the following equation:

$$d = \frac{b}{\frac{1}{\tan \alpha} + \frac{1}{\tan \beta}} \quad (2.1)$$

Since each point to be measured must be identified from both viewing positions unambiguously, high scene contrast is usually required. The typical features of the object surface are found and compared in both image pairs with help of 2D-correlation. From the position of each feature's centroid in both images, the angles α and β are deduced and the distance is then calculated using equation 2.1, with assumption that the cameras are calibrated, i.e., the distance of the cameras to each other and their orientation are predefined. According to the concrete applications two or more camera systems can be used (**Fig. 2.2b**). The stereoscopic measurement systems with more cameras work pretty well in some industrial inspections for such scenes with rich image contrast. The accuracy of the measurement S_{xyz} can be reached to better than $20\mu\text{m}$ for a $2\text{m} \times 2\text{m} \times 2\text{m}$ volume, if high resolution cameras, e.g. Kodak DCS460 with objective of 18mm are used [Luhm].

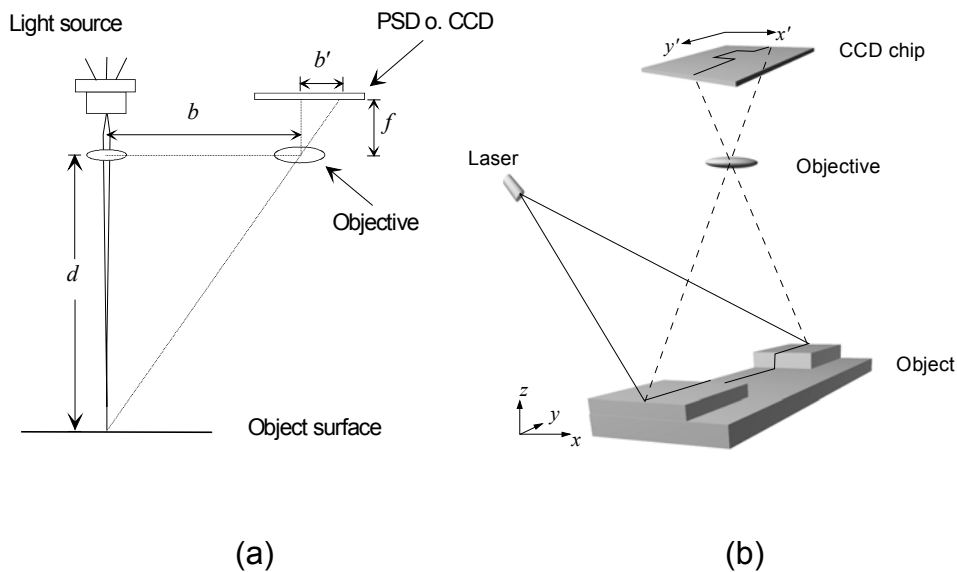


Fig. 2.3 Principle of active triangulation measurement. (a) 1D-active triangulation system. (b) Light sectioning measurement principle.

Like other triangulation techniques, the shadowing effect is also the typical problem for stereovision systems. Although it can be minimized by using the multi-viewpoint triangulation systems, this improvement must, on the other hand, be paid for by enormous increase of data processing and cost with increasing number of cameras. The

Theodolite system is another famous passive triangulation technique, which can reach an accuracy of ca. 1:200,000 but needs usually very long processing time [OFHB].

As illustrated in **Fig. 2.3a**, in the active triangulation technique one laser projector and one position sensitive detector, together with the point of the object surface, build the triangle, in which the distance of the object d is proportional to the lateral displacement of the light spot on the image detector b' . With the focal length f of the objective known, the distance of the target can simply be calculated by following equation:

$$d = f \cdot \frac{b}{b'} \quad (2.2)$$

The 1D triangulation can be easily extended to the 2D triangulation, which is the well known light sectioning principle. It uses a light source that projects a line on the surface of target. At the side of image detector, normally a CCD sensing array is used in stead of CCD line or linear PSD (**Fig. 2.3b**). Looking to the profile line from the viewpoint of the camera, the line appears to be curved in the image. If the position of light source, the orientation of the project plane, and the position and orientation of CCD camera are all known, the depth information of all points on the bright projected line can be determined. For acquisition of 3D object information only 1D-scanning needs to be performed [Kra][Vir]. The relative long processing time (20s) of such systems to get full depth information from the whole 3D scene with, say, a normal video camera (25 frames per second) is for many industrial applications not acceptable.

With further advanced techniques the direct 3D triangulation measurement without mechanical scanning is allowed, where 2D structured light projections are used. The most important methods are Graycode approach [Wah], Phase shifting projected fringe [Bre][HaLi], Coded binary patterns [Mal], Phase shifting Moiré [Dor] or color-coded triangulation measurement [Scu].

2.1.2 Interferometry

The optical interferometry is a coherent time-of-flight (TOF) measurement method, as shown in **Fig. 2.4**. It is described by the superposition of two coherent waves of the

same frequency ν , one reflected directly from the target and the other, split by a beam splitter and back scattered from the mirror, as the reference [OFBH]. Both waves mix and correlate on a 2D sensing array, resulting in an interferogram or correlogram after integration. The phase information of the interferogram, which is proportional to the distance of the 3D scene being measured, can be valued out by using corresponding phase shift methods. The unambiguous range of only half of the wavelength $\lambda/2$ and the relative distance measurement are the principle drawbacks of the classical interferometry [Scw-1].

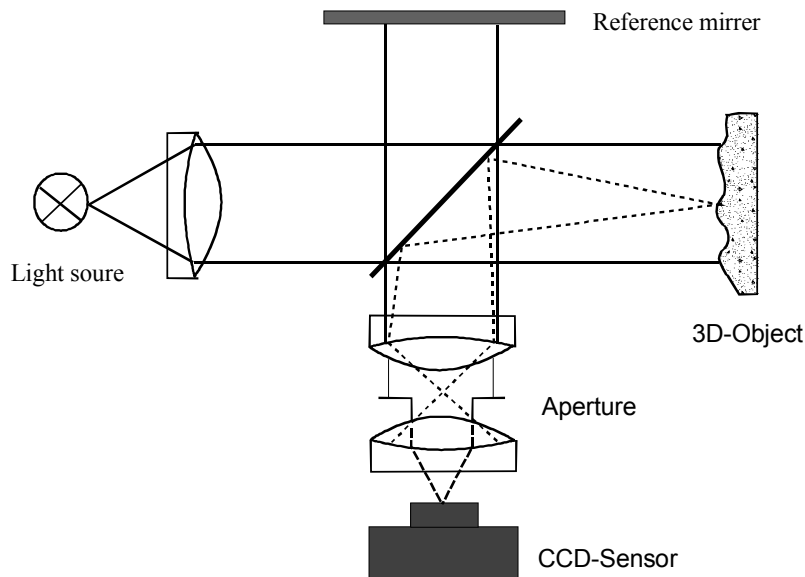


Fig. 2.4 Principle of instrument setup of interferometry

Many enhanced approaches such as Multiple-wavelength interferometry, electronic speckle pattern interferometry (ESPI) and white-light interferometry or coherent radar overcome this restriction. With development of computer and CCD camera techniques it is very common today to achieve the measurement precision with a fraction of optical wavelength of $\lambda/200$. Interferometry finds its applications predominantly in the measurements with high accuracy ($\lambda/100 \sim \lambda/1000$) over small distances ranging from micrometers to several centimeters.

2.1.3 Time-of-flight

The basic principle of the time-of-flight measurement is to measure the absolute time delay of the wave fronts reflected from the object surface, since we know the speed of light very precisely $c = 3 \times 10^8$ m/s. If the echo time t_d between the transmitting and receiving light signals is known, the distance d of the target can be then determined by $d = c \cdot t_d / 2$. As a measured time of 6.6ps corresponds to a distance of 1 mm, the basic problem of establishing a TOF ranging system is obviously the realization of a high accuracy time measurement. According to the different operation modes the TOF measurement are mainly divided into three groups [Scw-2]:

Pulsed modulation

Pulsed TOF technique measures directly the turn-round time of the light pulse. The actual time measurement is performed by correlation of start and stop signal with a parallel running counter. The advantage of using pulsed light modulation is its large unambiguous distance measurement. However, it requires at the same time a receiver with high dynamics and a large bandwidth. Also the current laser diodes limit the required pulse rising/falling time and high repetition rates of the pulses.

Continuous wave (CW) modulation

Compared to the pulsed modulation, the phase difference between the sent and received signals is generally measured, rather than the direct measurement of echo time of light pulses. If the modulation frequency is known, the measured phase delay corresponds directly to the time of flight. For CW-modulation a large variety of light sources is available. Different shapes of modulation signals such as sinusoidal waves or square waves can be used.

Similarly to optical interferometry, the RF-modulated light signals of a phase delay t_d , reflected from the object, is mixed and correlated with the reference RF-signal at the receiver, resulting in an ORF-interferogram which represents the total depth information of the target:

$$I(t_d) = s(t) * s'(t - t_d) = \lim_{\Delta T \rightarrow \infty} \frac{1}{\Delta T} \int_{\Delta T} s(t) \cdot s'(t - t_d) dt \quad (2.3)$$

where $s(t)$ and $s'(t)$ represent the reference RF-signal and back scattered light signal respectively. If we ignore the nonlinear effects and the noise behavior of the systems and assume the sinewave modulation, i.e.

$$s(t) = a_0 + a_m \cdot \cos(2\pi f_0 t) \quad (2.4)$$

the reflected signal $s'(t)$ has the same form as $s(t)$ but distinguishes itself with the coefficients a'_0 and a'_m and the echo time delay t_d .

$$s'(t) = a'_0 + a'_m \cdot \cos(2\pi f_0 (t - t_d)) \quad (2.5)$$

From equation (2.3) we can express the ORF-interferogram or the so called auto-correlation function as

$$\begin{aligned} I(t_d) &= A \cdot [a_0 + a_m \cdot \cos(2\pi f_0 t)] * [a'_0 + a'_m \cdot \cos(2\pi f_0 (t - t_d))] \\ &= \Gamma \cdot [1 + M \cdot \cos(2\pi f_0 t_d)] \end{aligned} \quad (2.6)$$

where A defines the system attenuation factor and

$$\begin{aligned} \Gamma &= A \cdot a_0 \cdot a'_0 \\ M &= \frac{1}{2} \cdot \frac{a_m \cdot a'_m}{a_0 \cdot a'_0} \end{aligned}$$

A large variety of methods can be used for the evaluation of the time delay t_d from equation (2.3). The most applied CW-modulation techniques among them are heterodyne technique (frequency shifting), homodyne technique (phase shifting) and FM-chirping modulation technique [Scw-2]. A detailed description of all these techniques can found in [Xu-1]. The ambiguity problem for the CW-modulation will not occur if the ranging distance of the system is less then the half of the RF-wavelength, which is normally in an order of some meters. This method therefore satisfies most industrial applications. For measurement beyond the unambiguous phase range unwrapping technique is required [Loff]. We focus in this work on the homodyne technique (phase shifting method), as discussed in more details in section 2.2.

Pseudo-Noise modulation

Pseudo-Noise (PN) modulation technique, which is widely used in applications in communication technique, combines the advantage of quasi-stationary CW-operation with the large unambiguous range of the pulse-modulation through the high pulse compression of the auto-correlation function of the PN-signals [Li][Scw-2]. Due to this

feature it finds nowadays more and more applications in the TOF ranging systems. **Fig.2.5** shows typical structure of TOF distance sensing system based on the principle of time-of-flight measurement.

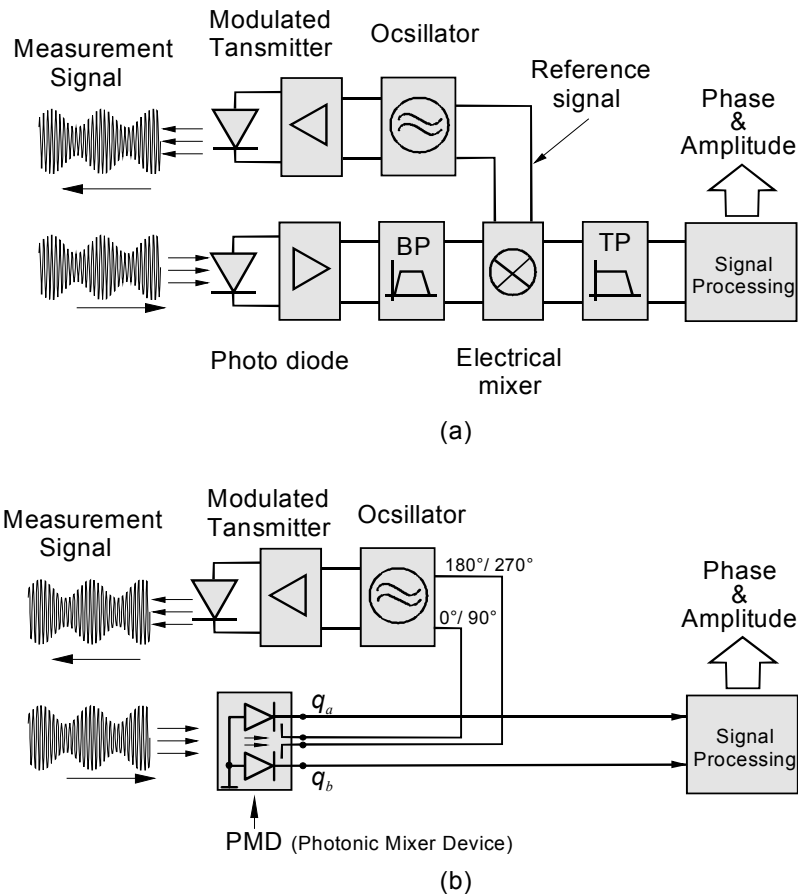


Fig. 2.5 Principle of time of flight measurement. (a) Conventional CW-modulation TOF-measurement; (b) The measurement principle of a PMD TOF-ranging technique.

2.1.4 Discussion

The three basic optical measurement principles: triangulation, interferometry and time-of-flight, are introduced in the previous sections. In the praxis many measurement systems based these three principle concepts are in developing for different applications. **Fig. 2.6** shows a comparison of available implementations in terms of distance range and resolution [Scw-1].

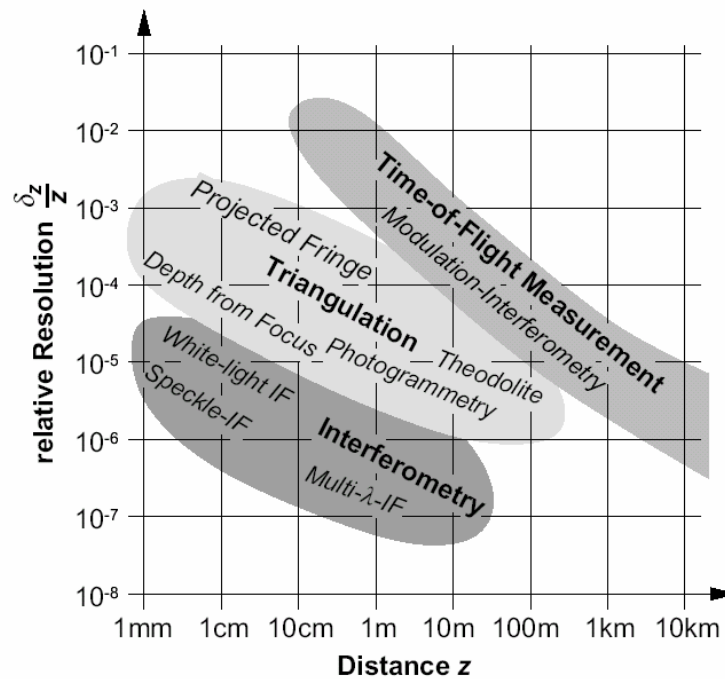


Fig. 2.6 Performance of different optical 3D ranging systems. The performance of ranging systems based on PMD is not included [Scw-1].

Independent of the progress and steady improvements in ranging sensors, we experience during the last years a continuously improving and rapidly growing field of industry: microelectronics. There is no doubt that each of the optical ranging methods introduced before has profited in its own way from the ongoing miniaturization in microelectronics. However, while triangulation and interferometry saw more cost-effective implementations, their measurement accuracy was not substantially affected. In the case of triangulation, the measurement range and precision is critically determined by the triangulation baseline. Obviously, miniaturization of the complete system leads to a reduced triangulation baseline and therefore to reduced accuracy. The precision in interferometry is basically given by the wavelength of the employed coherent light source, a parameter that cannot be influenced greatly. The situation is completely different for time-of-flight ranging techniques. They are not only becoming more and more cheaper, smaller and simpler to realize, their measurement accuracy is steadily improved. This is because, generally speaking, with decreasing minimum

feature size, devices become faster and hence, a better time resolution is possible. Therefore, we believe that the time-of-flight measurement principle will be used in more and more future applications.

2.2 Time of flight (TOF) 3D measurement systems with CW-modulation

2.2.1 Operation principle of the 3D TOF systems

In the previous section we discussed briefly different measurement techniques of getting 3D depth information. For the 3D-TOF ranging systems without scanning, the key function is the 2D-modulation and demodulation of the emitted and reflected light signals [He-2][Scw-4][Xu-3]. As illustrated in **Fig. 1.1**, the whole 3D-scene is illuminated simultaneously with the RF-modulated light, instead of scanning the 3D scene line by line. The back scattered wave front from the object arrives the 2D EO-mixer in the receiver, where it is mixed again with the reference signal, before an RF-interferogram can be formed at the sensing array after integration. One can see that this 2D-correlation process delivers the phase-correlation function related to each voxel of the 3D scene within the receiving aperture in a parallel way. Upon the acquired RF-correlation pattern, the complete 3D-information can be then extracted using e.g. phase shifting technique [Xu-1].

Modulated light sources

For a 3D-TOF ranging systems, as illustrated in **Fig. 1.1**, the simultaneous 3D scene illumination is required instead of scanning the whole scene using projected light beam or line. Compared to the optical interferometry, the emitted light is not longer restricted in the coherent light, so a large variety of incoherent light sources such as LEDs or laser diodes can be selected for use.

LEDs are relatively inexpensive and can be modulated up to some 100 MHz with nearly 100% modulation depth and high linearity. They cover a wide range of wavelengths from blue (400 nm) to the near infrared (1200 nm) with an optical power of up to several milliwatts. Lasers, even laser diodes, are relative more expensive than LEDs but offer more optical power and are suitable for modulation up to some GHz at a wide range of wavelengths. While both LEDs and laser diodes allow the direct modulation of light

intensity by controlling the driving current, other light sources require additional electro-optical modulator [Sal]. The typical solution of 2D illumination is to build an array of LEDs or laser diodes with direct modulation control. In order to obtain a possible homogeneous scene illumination, the combination of microlens array and lens or diffractive optical element (DOE) is usually employed (**Fig. 2.8**) [Tai].

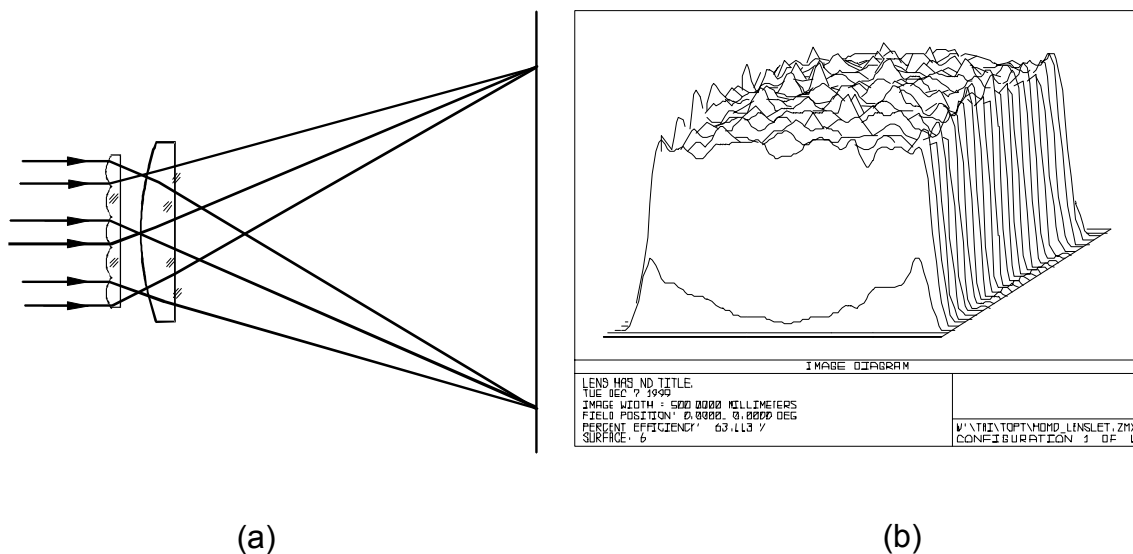


Fig. 2.7 (a) Configuration of the through microlens array or DOE, (b) Simulated result of illuminant distribution [Tai].

2D-electro-optical (EO) mixers

The key component of the 3D-TOF ranging systems is the 2D mixing device which functions as 2D-modulator of transmitting light signal required in some measurement concepts [He-1] and as 2D-mixer or demodulator on the receiver side.

Conventional 2D modulator concepts such as Kerr-cells, Pockels-cells [Xu-1] and FTR-modulator [He-1] are developed for 3D measurement. Kerr-cells are based on the quadratic electro-optic effect, that the polarization of a polarized light beam is rotated depending on the applied voltage. Together with a polarizer, the polarized incoming light can be modulated in intensity, through varying the modulated control voltage of the cell. The modulation frequency of Kerr-cells can reach up to 10 GHz. The modulation voltage of as high as 30 KV must be applied. Pockels cells, which make use of linear electro-

optic effect (Pockels effect), work very similarly and require a driving voltage of a factor of 10 lower than that of Kerr cells. Although the cut-off frequency of Pockels cell of 25GHz is even higher, the modulation frequency in the practical use, however, limits in several hundred MHz because of the cell's capacitance [He-2][Xu-1]. The optical to electrical conversion and integration after demodulation is realized by an 2D detector arrays such as CCD or CMOS active pixel sensors (APS).

The mechanical shutters or liquid crystal shutters are also reported to be used as modulators. But their use is usually limited in the measurement applications with low modulation frequencies (some kHz) [Sal].

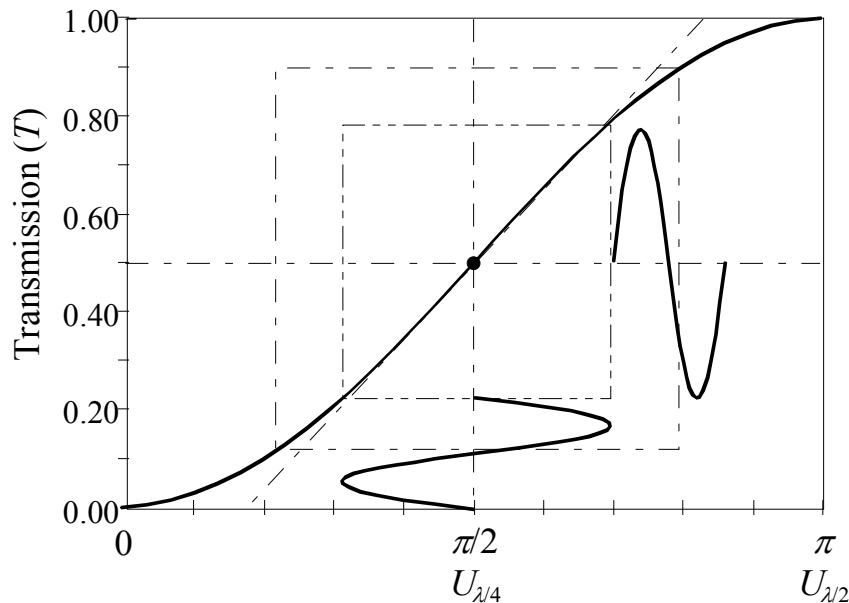


Fig. 2.8 The modulation characteristic of a Pockels cell [He-1]

The development of a new smart 2D mixer array, Photonic Mixer Device (PMD) based on standard CMOS technology, overcomes the restriction of conventional 3D-TOF measurement techniques. This innovative technique combines 2D mixing and correlation processes in one step. Each PMD pixel in the array is an independent demodulation and detection unit. More detailed discussion of PMD technique is presented in the next chapter. Other related architectures based on CCD principle are CCD lock-in pixel [Spi] [Lan] and CCD-range finding sensor [Miy].

Signal processing and 3D-data evaluation

As discussed in the following sections, the 3D-information can be acquired by implementing corresponding 3D-recovering algorithms. Since the output signal of PMD, representing the depth information, is in the practice corrupted by non-linearity of PMD and system noises or RF-cross-talk (RF noise) in time domain, the pre-processing techniques such as sub-sampling, low-pass filter or adaptive filter is necessary before the evaluation is performed.

2.2.2 Phase shifting technique (homodyne mixing method)

As mentioned above, phase shifting method is one of the important phase measurement techniques in the TOF ranging systems. The system block diagram shown in **Fig. 2.9** gives a simplified description of the operation principle. Similarly to the optical interferometry, the frequency of the RF-signal generator, providing a signal base for both transmitting and receiving channels, is set to be fixed while the initial phase of the RF-signal on either of the channels is shifted with a different phase shifting steps. The measurement of distance requires at least three frames of interference patterns.

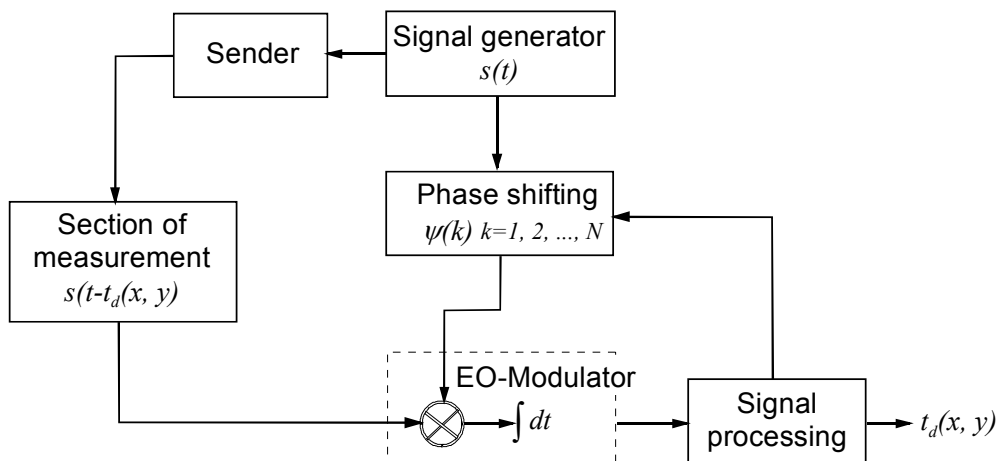


Fig. 2.9 Block diagram of 3D-TOF ranging system using phase shifting technique

The light source may be any incoherent light sources with constant intensity I_0 . It is modulated with the fixed frequency f_0 . The parameters $t_d(x,y)$ and $h(t)$ represent the echo time delay of light corresponding to each point from the 3D scene and the transfer function of the system respectively. The back scattered wavefront and the reference signal with phase shift φ_k are correlated in the detecting array at the receiver. The interferogram $I_k(x,y)$ is obtained after integration. The general description of the interferogram can be expressed by

$$I_k(x,y) = f(t_d(x,y)) = I_0 \cdot s'[t - t_d(x,y)] * h(t) * s(t + \varphi_k / 2\pi f_0) \quad (2.7)$$

where

$$k = 1, 2, \dots, N \text{ for } N \geq 3$$

and (x, y) denotes here the corresponding pixel position on an sensing array (e.g. PMD or CCD). $h(t)$ described the influence of the filters, band limitations and non-linear distortions of the system. For a fixed modulation frequency f_0 , $I_k(x,y)$ is the function of $t_d(x,y)$. It is obviously very difficult to find an analytical expression for equation (2.7) because of the complexity of $h(t)$ and applied signal forms. Instead of that, Z. Xu gives an intelligent solution in his work by using the theory of Fourier series expansion, which can be described as follows [Xu-1]:

Considering $h(t)$ being understood as modification of the signal form of the transmittance with the corresponding system attenuation factor $A(x,y)$, equation (2.7) can be rewritten as

$$I_k(x,y) = I_0 \cdot A(x,y) \cdot s(t + \varphi_k / 2\pi f_0) * s'[t - t_d(x,y)] \quad (2.8)$$

Since both $s(t)$ and $s'(t)$ are periodic signals of any signal form for the CW-modulation technique, they can be expressed by Fourier series expansion.

$$s(t) = \sum_{n=0}^{\infty} [a_n \cdot \cos(2\pi n f_0 t + 2\pi n \varphi_k) + b_n \cdot \sin(2\pi n f_0 t + 2\pi n \varphi_k)] \quad (2.9)$$

Similarly,

$$s'(t) = \sum_{n=0}^{\infty} [a'_n \cdot \cos(2\pi n f_0 t + 2\pi n \varphi_s) + b'_n \cdot \sin(2\pi n f_0 t + 2\pi n \varphi_s)] \quad (2.10)$$

where φ_s represents an initial phase offset of the system.

Under the condition that the RF-modulation signal has the frequency in general from some tens of MHz up to several GHz, much higher than the sampling frequency f_s in a range of some KHz, i.e. $f_0 \gg f_s$, the function system, $\cos(2\pi n f t + 2\pi n \varphi)$ and $\sin(2\pi n f t + 2\pi n \varphi)$ for all $n = 1, 2, 3, \dots$, composes a quasi-orthogonal system over an integration time period of $\Delta T = 1/f_s$. Substituting the Fourier expansions of the signals in (2.9) and (2.10) into equation (2.8), the auto-correlation function of the system can be expressed by

$$\begin{aligned}
I_k(x, y) &= \frac{I_0 \cdot A(x, y)}{\Delta T} \cdot \int \sum_{\Delta T m=0}^{\infty} \sum_{n=0}^{\infty} [a_m \cos(2\pi n f_0 t + 2\pi n \varphi_k) + b_m \sin(2\pi n f_0 t + 2\pi n \varphi_k)] \cdot \\
&\quad [a'_n \cos(2\pi n f_0 (t - t_d(x, y)) + 2\pi n \varphi_s) + b'_n \sin(2\pi n f_0 (t - t_d(x, y)) + 2\pi n \varphi_s)] \cdot dt \\
&= I_0 A(x, y) a_0 a'_0 + \\
&\quad \frac{I_0 A(x, y)}{\Delta T} \sum_{m=1}^{\infty} \sum_{n=1}^{\infty} a_m b'_n \int_{\Delta T} \cos(2\pi n f_0 t + 2\pi n \varphi_k) \cdot \cos(2\pi n f_0 (t - t_d(x, y)) + 2\pi n \varphi_s) \cdot dt + \\
&\quad \frac{I_0 A(x, y)}{\Delta T} \sum_{m=1}^{\infty} \sum_{n=1}^{\infty} b_m b'_n \int_{\Delta T} \sin(2\pi n f_0 t + 2\pi n \varphi_k) \cdot \sin(2\pi n f_0 (t - t_d(x, y)) + 2\pi n \varphi_s) \cdot dt + \\
&\quad \frac{I_0 A(x, y)}{\Delta T} \sum_{m=1}^{\infty} \sum_{n=1}^{\infty} a_m b'_n \int_{\Delta T} \cos(2\pi n f_0 t + 2\pi n \varphi_k) \cdot \sin(2\pi n f_0 (t - t_d(x, y)) + 2\pi n \varphi_s) \cdot dt + \\
&\quad \frac{I_0 A(x, y)}{\Delta T} \sum_{m=1}^{\infty} \sum_{n=1}^{\infty} b_m a'_n \int_{\Delta T} \sin(2\pi n f_0 t + 2\pi n \varphi_k) \cdot \cos(2\pi n f_0 (t - t_d(x, y)) + 2\pi n \varphi_s) \cdot dt
\end{aligned} \tag{2.11}$$

Equation (2.11) can be rewritten according to the orthogonal characteristics of sinusoidal functions

$$\begin{aligned}
I_k(x, y) &= I_0 A(x, y) a_0 a'_0 + \\
&\quad \frac{I_0 A(x, y)}{2\Delta T} \sum_{n=1}^{\infty} a_n a'_n \int_{\Delta T} \cos[2\pi n f_0 t_d(x, y) + 2\pi n (\varphi_k - \varphi_s)] dt + \\
&\quad \frac{I_0 A(x, y)}{2\Delta T} \sum_{n=1}^{\infty} b_n b'_n \int_{\Delta T} \cos[2\pi n f_0 t_d(x, y) + 2\pi n (\varphi_k - \varphi_s)] dt - \\
&\quad \frac{I_0 A(x, y)}{2\Delta T} \sum_{n=1}^{\infty} a_n b'_n \int_{\Delta T} \sin[2\pi n f_0 t_d(x, y) + 2\pi n (\varphi_k - \varphi_s)] dt +
\end{aligned}$$

$$\begin{aligned}
& \frac{I_0 A(x, y)}{2\Delta T} \sum_{n=1}^{\infty} b_n a'_n \int_{\Delta T} \sin[2\pi n f_0 t_d(x, y) + 2\pi n(\varphi_k - \varphi_s)] dt \\
& = I_0 A(x, y) a_0 a'_0 + \\
& \frac{I_0 A(x, y)}{2\Delta T} \sum_{n=1}^{\infty} (a_n a'_n + b_n b'_n) \int_{\Delta T} \cos[2\pi n f_0 t_d(x, y) + 2\pi n(\varphi_k - \varphi_s)] dt + \\
& \frac{I_0 A(x, y)}{2\Delta T} \sum_{n=1}^{\infty} (b_n a'_n - a_n b'_n) \int_{\Delta T} \cos[2\pi n f_0 t_d(x, y) + 2\pi n(\varphi_k - \varphi_s)] dt \tag{2.12}
\end{aligned}$$

Introducing following constants to further simplify the expression

$$\begin{aligned}
A_n &= a_n a'_n + b_n b'_n & B_n &= b_n a'_n - a_n b'_n \\
\Gamma(x, y) &= I_0 A(x, y) a_0 a'_0 & M_n &= \sqrt{A_n^2 + B_n^2} / 2a_0 a'_0 \\
\cos \vartheta_n &= A_n / \sqrt{A_n^2 + B_n^2} & \sin \vartheta_n &= B_n / \sqrt{A_n^2 + B_n^2}
\end{aligned} \tag{2.13}$$

The general expression of the ORF-interferogram using the phase shifting technique can be expressed by

$$I_k(x, y) = \Gamma(x, y) \left\{ 1 + \sum_{n=1}^{\infty} M_n \cos(2\pi n f_0 t_d(x, y) + 2\pi n(\varphi_k - \varphi_s) + \vartheta_n) \right\} \tag{2.14}$$

The coefficient Γ in equation (2.14) is the local mean intensity that is similar to the gray tone of the 2D image. $\{M_n\}$ defines the fringe contrasts of the 2D correlation pattern corresponding to different harmonic waves and $\{\vartheta_n\}$ the fixed phase offsets. Since the function $I_k(x, y)$ has the same period as the modulation signal, the unambiguous range of the distance measurement corresponds to the half of the modulation period i.e. $\lambda/2$, where $\lambda = 1/f_0$ if without the phase unwrapping.

We discuss now the ORF-interferogram in the special case of using sinusoidal and square wave modulation signals. For the sinewave modulation, only the coefficients a_0, a_1, a'_0, a'_1 are not zero. Equation (2.15) is in this case reduced to

$$I_k(x, y) = \Gamma(x, y) \left\{ 1 + M_1 \cos(2\pi f_0 t_d(x, y) + 2\pi(\varphi_k - \varphi_s)) \right\} \tag{2.15}$$

with $\Gamma(x, y) = I_0 A(x, y) a_0 a'_0$ and $M_1 = a_1 a'_1 / 2a_0 a'_0$.

If we ignore the lateral indices and the initial phase offset φ_s , i.e. $\varphi_s = 0$, equation (2.15) is just the same as equation (2.6). Similarly, if the signals in both transmitting and receiving channels are square wave modulated and the non-linearity of the system is ignored, all odd elements of the fringe contrasts are not zero while all other items corresponding to the even harmonic waves vanish, i.e.

$$M_n = \begin{cases} b_n b'_n / 2a_0 a'_0 & \text{for } n = 1, 3, 5, \dots \\ 0 & \text{for } n = 2, 4, 6, \dots \end{cases} \quad \text{and } \{\mathcal{G}_n\} = 0, \text{ for all } n \quad (2.16)$$

The correlation result of the square wave modulation in this case has the form of a triangular function. In the practice, however, many factors such as the band limitation and non-linear distortion of the system, will have influence on the correlation result, which leads to a distorted auto-correlation waveform, therefore, it is in most cases not possible to obtain the desired depth information $t_d(x, y)$ analytically. Additional evaluation algorithms for the 3D-data acquisition are necessary.

2.2.3 3D-data evaluation algorithms

The problem of acquisition of desired 3D-depth information in the system is to the extract the time of flight t_d from the interferogram given by equation (2.14). The phase evaluation algorithm should be simple, accurate, fast and noise reducible. Since the terms in the equation (2.14), Γ , $\{M_n\}$ and t_d , are undefined, so more independent interferograms of the same 3D scene are needed to acquire the echo time delay t_d . For case of the harmonic modulation, at least three phase shifting steps are necessary. The phase shifting steps are normally chosen to be equidistantly distributed over one 2π -period for fast evaluation

$$\varphi_k = \frac{2\pi}{N} k \quad k = 1, 2, 3, \dots, N \quad \text{with } N \geq 3. \quad (2.17)$$

Letting $\varphi_k = 0$ and ignoring the position indices x and y for simplicity of the expression, equation (2.14) is rewritten

$$I_k = \Gamma \left\{ 1 + \sum_{n=1}^{\infty} M_n \cos(2\pi n f_0 t_d + n \varphi_k + \mathcal{G}_n) \right\} \quad (2.18)$$

for $k = 1, 2, 3, \dots, N \quad \text{with } N \geq 3.$

In a real 3D TOF-ranging system based on the CW modulation method, the non-linearity problem arise not only from the eletro-optical mixer itself but also from other system components such as light source (LEDs or laser diodes), signal generator, phase shifting unit or processing circuits. Although nonlinear distortion can be partly minimized through band-pass filter and modulation waveform design, appropriate algorithms have to be derived to further reduce the system errors reduced by non-linearity and noise, ensuring high accuracy of 3D-data reconstruction. The nonlinear evaluation algorithm based on the least square criterion gives an optimal solution especially in case of Gaussian noise [Mar][Xu-1].

For N measurements performed according to different phase shifting steps, the sum of the square errors is defined as

$$E = \sum_{k=1}^N \left\{ I_k - \Gamma \left[1 + \sum_{n=1}^{\infty} M_n \cos(n\varphi_d + n\varphi_k - \mathcal{G}_n) \right] \right\}^2 \quad (2.19)$$

To find the values of the parameters Γ , $\{M_n\}$ and φ_d that minimize equation (2.19) means

$$\frac{\partial E}{\partial \Gamma} = 0, \quad \frac{\partial E}{\partial M_n} = 0 \quad \text{and} \quad \frac{\partial E}{\partial n\varphi_d} = 0 \quad (2.20)$$

$$\text{for } n = 1, 2, 3, \dots, l.$$

Considering the limited bandwidth in the practice and the coefficients of the high order items in Fourier expansion vanish very quickly, l is normally truncated to a finite value, say 10. The parameter φ_d can be obtained by solving equations in (2.20) [Xu-2]

$$\varphi_d = \frac{1}{n} \left\{ \arctan \left[\frac{- \sum_{k=1}^N I_k \sin(n\varphi_k)}{\sum_{k=1}^N I_k \cos(n\varphi_k)} \right] + \mathcal{G}_n \right\} \quad (2.21)$$

$$\text{for } n = 1, 2, 3, \dots, l.$$

We have the distance estimation within the unambiguous range, with the light speed known, i.e. $c = 3 \times 10^8 \text{ m/s}$

$$d(x, y) = \frac{c}{2} \cdot t_d(x, y) = \frac{c}{2f_0} \cdot \frac{\varphi_d(x, y)}{2\pi} \quad (2.22)$$

The intensity image can be obtained by

$$\Gamma(x, y) = \frac{1}{N} \cdot \sum_{k=1}^N I_k(x, y) \quad (2.23)$$

For 4-phase shifting modulation technique, the evaluation algorithm obtained according to the least square principle is given by [Scw-3]

$$\varphi_d(x, y) = \arctan \left[\frac{I_3(x, y) - I_1(x, y)}{I_2(x, y) - I_4(x, y)} \right] \quad (2.24)$$

where $\varphi_d(x, y) = 2\pi f_0 t_d(x, y)$, for $x, y = 1, 2, 3, \dots, M, N$. $\{I_k\}$ for $k = 1, 2, 3$ and 4 represent the measured interferograms at different phase shifts with $\varphi_k = 0^\circ, 90^\circ, 180^\circ$ and 270° respectively.

3 Photonic Mixer Device (PMD)

As already discussed in the previous sections, high resolution ranging measurement using CW-modulation technique systems requires very high precision of determination of phase delay t_d . In a conventional CW-system as described in **Fig. 2.5a**, extremely complicated mixing and processing circuitry, which is designed for error compensation and noise suppression, introduces itself, on the other side, new noise sources, time delay and drifting errors. Even with such a high consume in the circuit design it is hardly realizable for a high ranging accuracy e.g. of 1mm in the conventional system concepts.

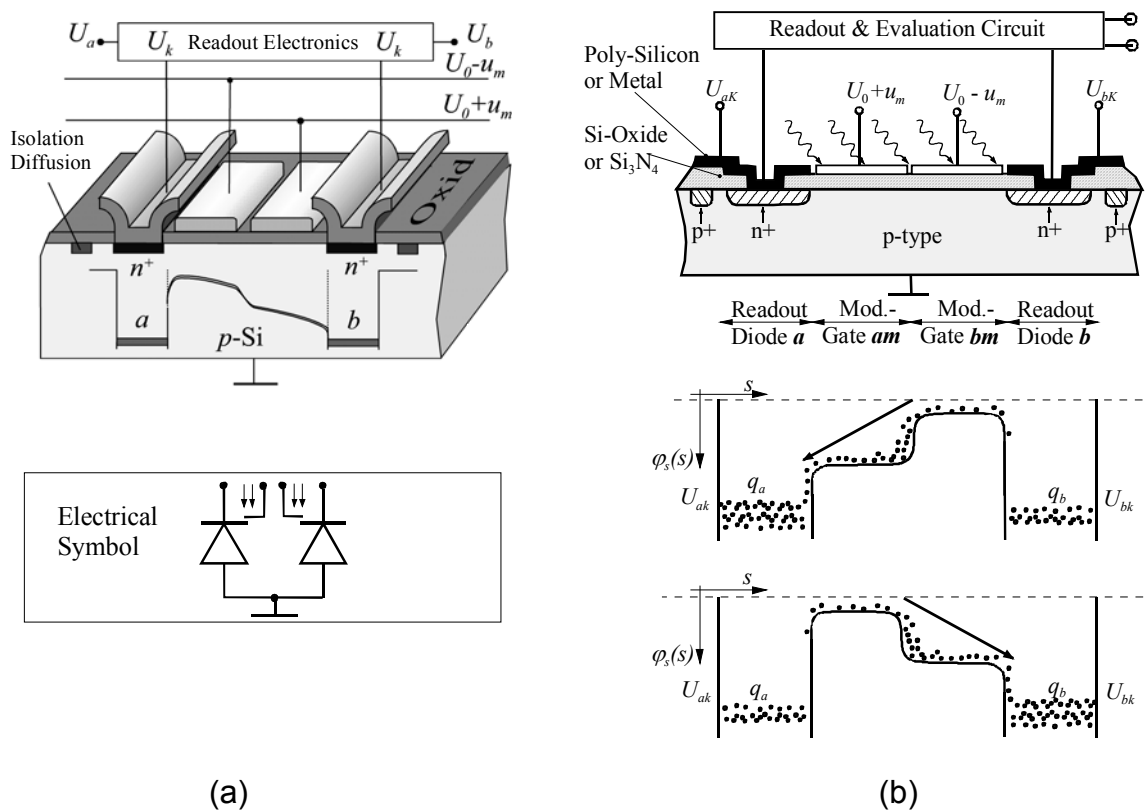


Fig. 3.1 (a) The typical simplified 2-gate surface channel PMD structure and the electrical symbol of PMD. (b) The schematic illustration of the cross-section of PMD and the principle of charge transfer under the control of gate modulation signals [Scw-3].

The new novel semiconductor sensor structure – Photonic Mixer Device – has being developed based on the creative idea of Prof. R. Schwarte, on the institute of signal processing of university Siegen, Zentrum fuer Sensorsysteme (ZESS) and later on S-

TEC GmbH since 1997. Due to its unique operation principle of performing simultaneous mixing and charge integration procedure in the photosensitive area of the PMD, it offers an excellent solution to overcome the most typical difficulties in the conventional 3D-ranging system design with CW-modulation. Each smart PMD pixel itself is an independent ranging unit, in ability of delivering the range related information. The characteristic of easy integration of PMD pixels into a PMD line or PMD matrix allows the realization of compact, flexible, fast and robust low-cost 3D TOF solid-state ranging systems.

3.1 General description of PMD principle

The PMD is a surface channel semiconductor device which is in principle comparable to CCDs in the charge transfer mechanism. The cross-section of a simplified two modulation gates PMD-structure, realized based on standard CMOS technology, is shown in **Fig. 3.1**. The two conductive and transparent MOS photogates build the optical sensitive zone of PMD for receiving RF-modulated optical signals. Adjacent to them are two reverse biased (n^+p) diodes with common anodes on the ground potential for charge sensing. If the push-pull modulation signals of arbitrary waveforms (e.g. sinusoidal, square waves) are applied to both electrodes connected on the photo gates, the potential distributions inside the device function like a seesaw, resulting in a balanced mixing effect, where the photo-generated charge is separated and moved to either the left or the right in the potential well. The average photo current is then sensed out by the on-chip integrated readout circuit.

The photo gate is also known as MOS diode or MOS capacitor, which can be located in accumulation, depletion or inversion mode, according to the applied photogate voltage [Sze]. If at the moment the photogate is biased with a positive voltage, a depletion zone appears underneath the photogate. Under the equilibrium condition, the minority carriers, here the electrons for p-type substrate, drift to the semiconductor surface and build there an inversion layer. This assumption is usually valid for MOS transistor but not suitable for PMD. Similarly to CCDs, PMD operates in a dynamic process, which means the photogates of PMD work in the deep depletion mode, as shown in **Fig. 3.2a**. This occurs at the beginning that the voltage is applied to the gate. Since the minority

carriers can not follow the abrupt changes of the gate signal at this moment, the depletion region extends deep into the semiconductor resulting in a deep space charge region, until the equilibrium condition is restored after the relaxing time (usually several 10 ms). Because PMD works normally with very high frequency (i.e. from some 10 MHz to several 100 MHz), the signal applied on the modulation gate of PMD changes very fast so that the gate remains at non-equilibrium state during the whole process. The relation of the gate voltage V_G and the surface potential ψ_s in the case without any illumination is given by equation (3.1) [Xu-1]

$$V_G - V_{FB} = \frac{\sqrt{2\epsilon_s q N_A \psi_s}}{C_{ox}} + \psi_s \tag{3.1}$$

with V_{FB} the flat band voltage, q the element charge, N_A the acceptor state density and C_{ox} the capacitance of oxide.

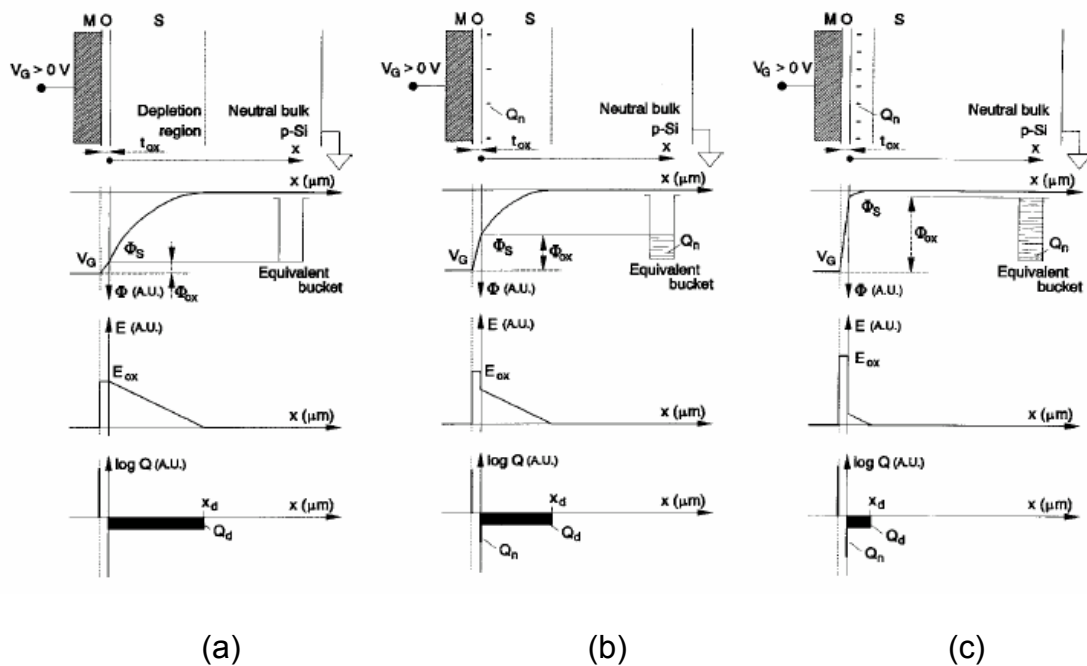


Fig. 3.2 Band model of a typical MOS diode (capacitor) in p-silicon in different modes: (a) deep depletion, (b) weak inversion after integration of optically generated photoelectrons, (c) strong inversion – saturation of photogate [Teu].

If there exists available free carriers (electrons), they can be then collected in the space charge region evolved below the gate. With the increasing of the charge stored in the

space charge region, the surface potential decreases. Compared to CCD, however, the generated charge would be shifted very fast to the readout port due to the high modulation frequency of PMD. The available free carriers (electrons) for PMD are either optically (optical signal) or thermally (dark current) generated charge.

3.2 PMD charge transfer process

With the optical generation of electron hole pairs, free charge carriers become available. The electron-hole pairs are separated in such a way that the minority carriers (electrons in our case) drift to the semiconductor surface while the majority carriers (holes) are rejected into the bulk. Since the push-pull signals are applied to the gates of PMD, a gradient of the surface potential distribution in the active optical area of PMD is built along the charge transfer direction, which switches from one side to the other with the modulation frequency f_0 . **Fig. 3.3** shows the simulated 3D-potential distribution over the whole device at three typical situations under the control of modulation signal applied on the modulation gates of PMD.

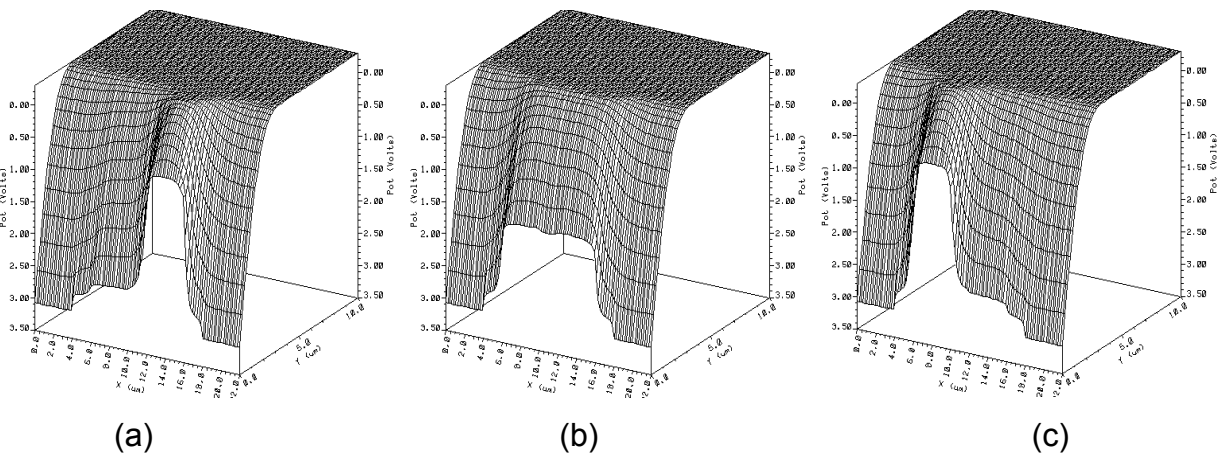


Fig. 3.3 Simulated 3D potential distribution of a typical 2G-PMD structure under the control of modulation signal applied on the modulation gates of PMD. (a) $u_a=U_0+u_m$ and $u_b=U_0-u_m$, (b) $u_a=u_b=U_0$, (c) $u_a=U_0-u_m$ and $u_b=U_0+u_m$ [Frk].

Three mechanisms are involved in the charge transfer process of the PMD, which are listed as follows [Xu-1][Bux-3]:

- Self-induced field drifting
- fringing field drifting
- Thermal diffusion

The self-induced drifting is caused by the field generated due to the inhomogeneous distribution of the carrier concentration. This transfer mechanism can only be important for the case that the local carrier concentration is relatively high, e.g. in CCD sensors. Its contribution for the charge transfer in the PMD operation, however, is not expected to be large. Because of the high modulation frequency, there is only a little charge accumulated in the potential well, which is permanently sensed out by the readout circuit. Therefore, the self-induced field in PMD is, compared to CCD, much weaker, even under the exposure with extremely high illumination. The other two processes dominate mainly the transfer of generated charge in PMD operation. The thermal diffusion effect plays an important role at the beginning of the charge transfer, compared to the fringing field which arises from the potential distribution in the active optical area due to the applied voltage swing on adjacent modulation gates of PMD [Xu-1].

Assuming that the RF-modulated optical signal of the same frequency as the PMD modulation signal, with a full modulation depth of 100%, is set in phase with the modulation signal on the left PMD gate a_m (0° phase shifting). In the half period that the optical signal is exposed to the optical active area, the photo generated charge drifts mostly to the left due to the surface potential distribution as shown in **Fig. 3.3a**, which is further coupled to the corresponding readout diode. In case of the light signal setting in phase with the right PMD gate b_m (180° phase shifting), the most generated charge moves to the right potential well (**Fig. 3.3c**). For a phase shift of 90° , the charge drifts to both sides and sensed by both diodes are just the same (**Fig. 3.3b**). Being the average photo currents from the both readout diodes \bar{i}_a and \bar{i}_b respectively, it is apparent that both currents \bar{i}_a and \bar{i}_b are the function of the phase delay of the modulated optical signal referred to the gate modulation signal. If we consider that this time delay of the light t_d is related to the distance to the target, the relations between the outputs \bar{i}_a and \bar{i}_b of PMD and the optical signal can be then represented by equation (2.8). The sum of

the outputs ($\bar{i}_a + \bar{i}_b$) gives the total photo current corresponding to the optical intensity, while the differential output of both ($\Delta\bar{i}_{ab} = \bar{i}_a - \bar{i}_b$) stands for the correlation product of the reflected optical signal and the reference signal. **Fig. 3.4** shows the measured outputs of a PMD test pixel with the phase delay of optical signal corresponding to 0° , 90° and 180° , referred to the PMD reference signal, respectively.

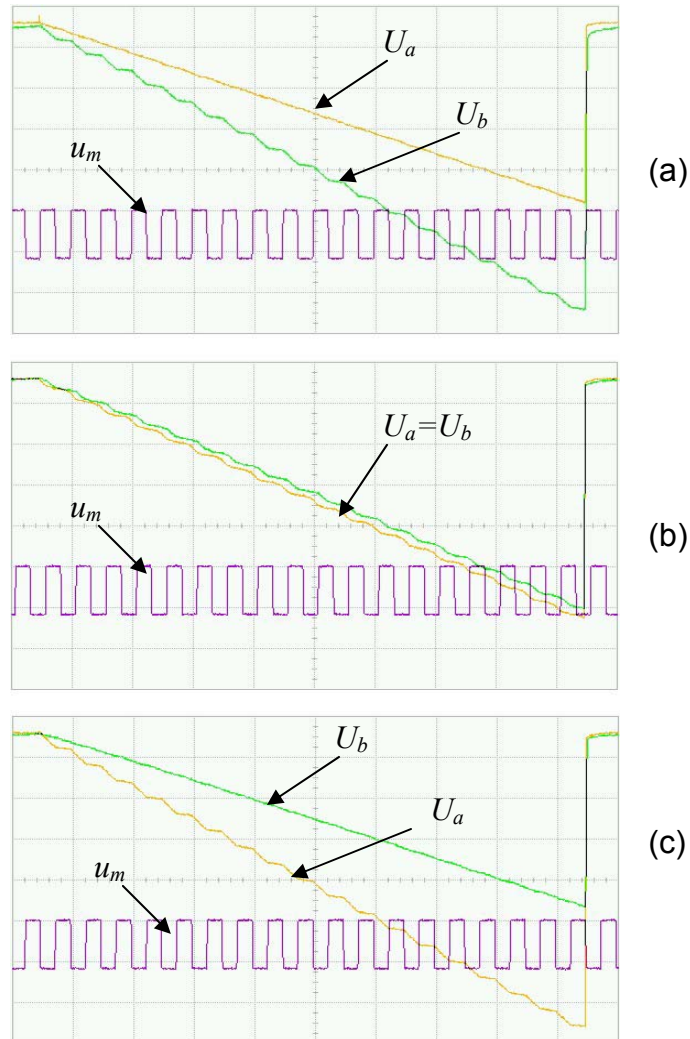


Fig. 3.4 PMD output signals U_a and U_b referred to the phase delay of optical signal at (a) 0° , (b) 90° and (c) 180° respectively. PMD test chip: STP17.5-2F-No.1.2-Z3. $f_{mod} = 40\text{KHz}$. Squarewave modulated.

3.3 Transfer characteristic and frequency limitations of the PMD

As an electro-optical modulator (EOM), the transfer characteristic of PMD is one of the important norms for judging the PMD performance concerning the linearity and the charge separation efficiency, in dependence on the frequency and the amplitude of the gate modulation voltage. Different from the definition of the transfer characteristic of such conventional EOMs as Pockels cells, which is the ratio of the output intensity of light to the input intensity of light [He-1][Scw-4], the output of PMD is no longer an optical signal while its input is still the same. To compare the output with the input of PMD, the optical input needs to be converted to the electrical quantity. The transfer characteristic of PMD is defined by the following equation [Scw-5][Xu-1]

$$T_a(f, u_{am}) = \frac{1}{2A \cdot q \cdot \int G(x) \cdot dx} \left\langle \frac{\partial Q_s(u_{am}(t))}{\partial t} \right\rangle \quad (3.2)$$

in which $G(x)$ is the electron-hole generation rate at distance x from surface of the semiconductor and Q_s the signal charge under the modulation gate of an area A and the modulation frequency f .

As can be seen in **Fig. 3.5**, an absolute 100% of separation of the generated charge is in practice not possible due to the surface potential distribution in the optical active area of PMD and the charge transfer inefficiency, since the charge transfer is forced in the operation to be terminated within the modulation period $T_{am} = 1/f$ that is normally much shorter than the relaxation time [Xu-1]. If the modulation frequency becomes extremely high, the generated charge can not follow the changes in the surface potential distribution. The maximum frequency should be limited with the carrier velocity that tends to its saturation velocity v_{sat} in the semiconductor. The cut-off frequency of PMD can be proximately predicted by equation [Bux-1] [Xu-1]

$$f_c = \frac{\mu_n E_f}{2\pi L \left(1 + \frac{\mu_n E_f}{v_{sat}}\right)} \quad (3.3)$$

where μ_n is the carrier mobility, L the total channel length of PMD and E_f the fringing field which is defined by

$$E_f = \frac{\Delta V}{l} \cdot \left[\frac{6.5d_{ox}/l}{1+6.5d_{ox}/l} \right] \cdot \left[\frac{5W/l}{1+5W/l} \right] \quad (3.4)$$

with the depletion depth W , the gate length l , the thickness of the oxide d_{ox} and the voltage swing applied to the modulation gates. As illustrated in **Fig. 3.5**, given a voltage swing and oxide thickness, a PMD with a long channel length has longer transfer time than short channel PMDs, therefore lower cut-off frequency [Xu-1]. From this point, the finger structure PMD offers an optimal solution [Scw-6] [Xu-1]. With its comparable optical active area and short channel length it increases not only the operation frequency of PMD at similar light sensitivity but also minimized the lateral sensitivity and asymmetrical effect in the optical active area, as measurement results shown later in the following chapter.

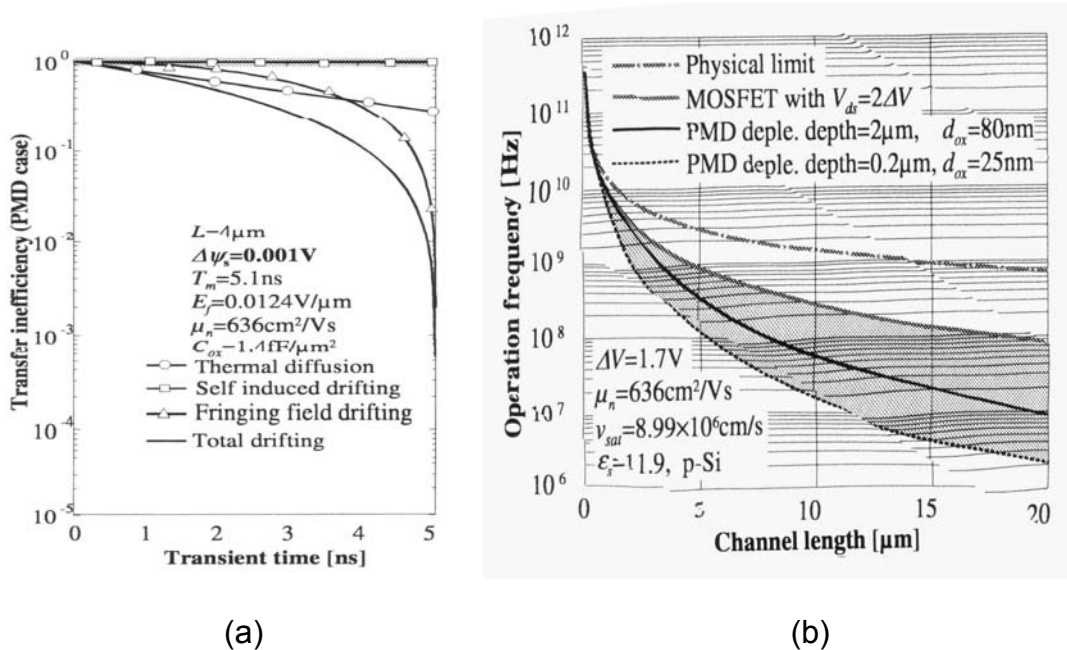


Fig. 3.5 Charge transfer inefficiency of PMD (a) and the operation frequency dependent on PMD channel length (b) [Xu-1].

3.4 Readout technique of PMD

The charge sensing of PMD can be realized in principle either by using current-sensing technique or voltage-sensing technique. Similarly to the imaging sensing arrays (e.g. CCD or CMOS), the readout circuits can also be integrated on chip directly in the near

of the PMD structure, forming an active pixel, allowing the realization of PMD sensing array with help of the modern CMOS-technology.

Fig. 3.6a shows a typical current sensing circuit of the PMD [Sci]. The photo generated charge accumulates in the external capacitance C_A . The voltage of the readout diode is steady fixed to a constant potential through the feedback loop composed of transistors T1, T2 and T3, so that the mixing process in the optical active area is not influenced during the whole integration period. It performs also the conversion of the generated photo charge to the voltage ΔU_{out} . The output of the sensing circuit at the end of an integration period T_{int} is given by

$$\Delta U_{out} = \frac{\bar{i}_{ph} \cdot T_{int}}{C_A + C_G} \quad (3.5)$$

where C_G is the equivalent gate capacity of the following readout buffer.

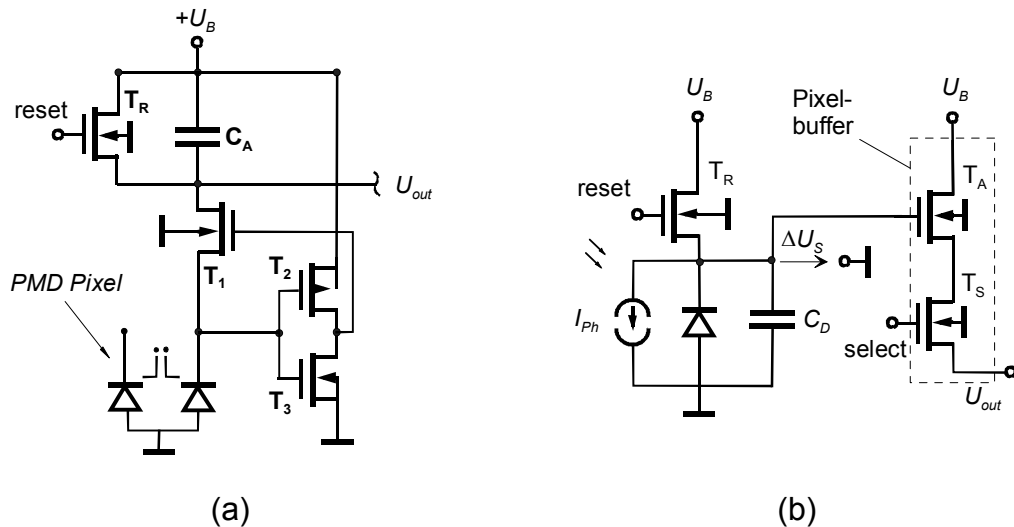


Fig. 3.6 The typical applied readout techniques for PMD. (a) The principle of current sensing technique. (b) The typical voltage readout technique.

The voltage sensing technique is the most frequently used readout technique in the CCD sensors and in the APS-CMOS sensors as well. The voltage sensing is also called floating diffusion technique, as illustrated in **Fig. 3.6b**, since the charge is collected, in addition to the external capacitance, also on the diffusion capacity of the readout diode that is however voltage dependant during the integration period. The sensed voltage

ΔU_s can also be determined by equation (3.5), in which the gate capacity C_G is alone that of transistor T_A .

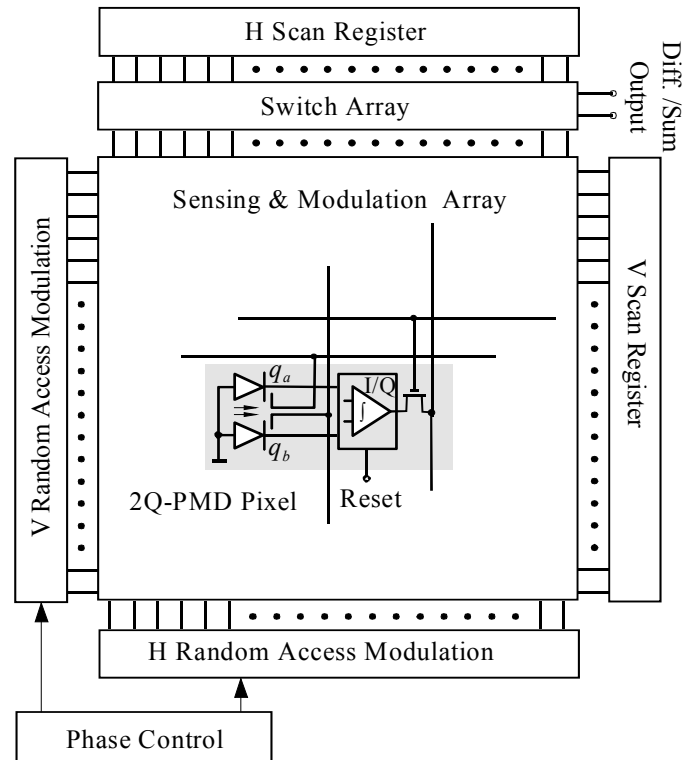


Fig. 3.7 Architecture of a PMD array used for 3D-ranging system with Phase shifting technique [Scw-6].

Both charge sensing techniques have their advantages and drawbacks. The current sensing technique has higher linearity in the output which depends merely on the accuracy of the integration capacitance, while the performance of the voltage sensing is negatively influenced by the non-linear behavior of the capacitance-voltage dependency. The fixed voltage of the readout diode in the current sensing circuit ensures the PMD-mixing process being not affected over the whole integration time. But in the voltage sensing, the potential of the readout diode varies during the integration, which further influences the PMD mixing process through interfering the potential distribution of the optical active area, causing some non-linear distortion. As main drawback of the current sensing concept presented in **Fig. 3.6a** is the relative low bandwidth and limitation of the maximum modulation frequency of PMD due to the slow control loop. For the voltage sensing, in comparison, there is no such problem. Since

the PMD is compatible to the CMOS technology, single PMD pixels can be easily integrated into a PMD sensing array with the modern CMOS-technology nowadays, leading to smart 3D-camera systems with high quality, as illustrated in **Fig. 3.7**.

3.5 Measurement of the phase and TOF information using PMD

As already discussed in the previous sections, PMD offers an excellent solution for 3D TOF ranging system. This new concept overcomes the typical drawbacks of conventional TOF ranging systems with its unique features of balanced electro-optical mixing function and simultaneous integration of the signal charge generated in the photosensitive area of the PMD. Since the correlation process occurs in the PMD photosensitive area, only readout circuitry of low bandwidth is necessary, which is easily integrated together with PMD as on-chip periphery. This extremely simplifies the design of the 3D ranging systems using PMD as key component. In the following we list some typical ranging system concepts based on the PMD technology.

- PMD ranging system with CW – modulation

The CW-modulation is the widely used modulation technique applied in the TOF measurement systems. The configuration of such ranging systems based on PMD is considerably simplified. In addition to the phase shifting modulation technique (quasi-heterodyne technique), which has been discussed in the previous sections, other CW-modulation methods such as the so called heterodyne modulation method is also an often used technique, in which either the PMD or the optical signal is modulated with changing frequencies [Xu-1]. **Fig. 1.1** shows the configuration of a 3D PMD-ranging system using phase shifting CW-modulation. Based on at least three measurements the distance information of each pixel can be obtained according to the phase evaluation algorithm. Although arbitrary signal forms can be used in the CW-modulation, squarewave and sinewave are still the most applied modulation signals in practice.

- PN - modulation

The pseudo-noise (PN) sequence modulation technique is an important method both for ranging and communication systems [Li][Scw-2]. The most significant feature of PN modulation is its anti-interference capability and for the distance measurement the large

unambiguous range, in contrast to the CW – modulation. **Fig. 3.8** shows the output signals of PMD in case of 15-bit PN-modulation. The discriminator function of PMD can be obtained based on two measurements, one in phase and one with one bit delay T_B , the phase delay t_d referred to the distance of target is proportional to the amplitude of output in the first bit, which is given by

$$t_d = T_D + \frac{T_B}{2} - \left(\frac{D_\Delta(\tau)}{D_\Sigma(\tau)} \right) \cdot \frac{T_B}{2} \quad (3.6)$$

where $D_\Delta(\tau)$ and $D_\Sigma(\tau)$ represent the discriminator output and the intensity value of PMD respectively

$$\begin{aligned} D_\Delta(\tau - T_D) &= (\bar{i}_a - \bar{i}_b) - (\bar{i}_c - \bar{i}_d) = \Delta\bar{i}_{ab} - \Delta\bar{i}_{cd} \\ D_\Sigma(\tau - T_D) &= (\bar{i}_a - \bar{i}_b) + (\bar{i}_c - \bar{i}_d) = \Delta\bar{i}_{ab} + \Delta\bar{i}_{cd} \end{aligned} \quad (3.7)$$

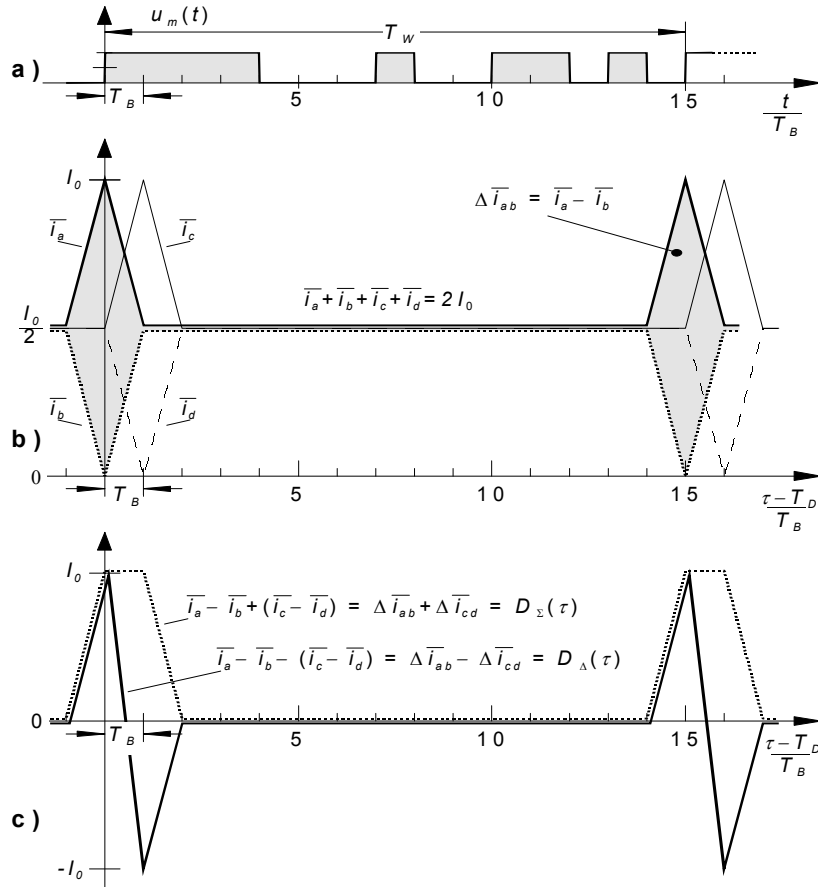


Fig. 3.8 PN-modulation and the PMD output. (a) Ideal 15bit PN sequence, (b) the ideal correlation outputs of PMD and (c) the discriminator characteristic and the intensity value of PMD.

- PMD ranging with phase locking technique

In a real system the influences of noise sources, the band-limit as well as the non-linearity of the system must be taken into account. The correlation output of the PMD will not look like that shown in **Fig. 3.8**, rather more or less distorted. The accuracy of distance evaluation according to equation 3.6 might not be acceptable in some distance range due to the distortion. **Fig. 3.9** shows a discriminator characteristic of PMD under influences of noise disturbance and non-linear distortion.

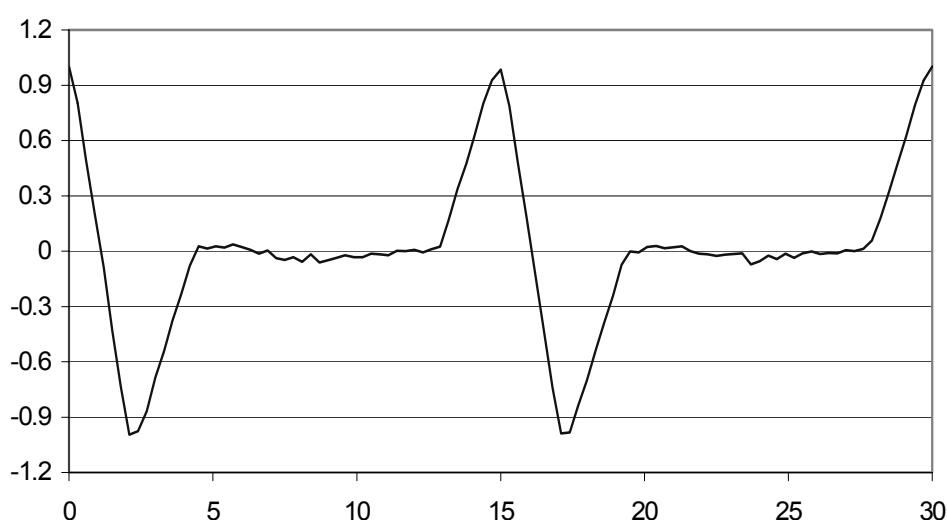


Fig. 3.9 The discriminator characteristic of PMD in case of band limitation and non-linear distortion.

Instead of solving directly the time delay t_d as described above, a number of sophisticated ranging methods based on the phase locking techniques which have been mostly used in laser radar systems can be adapted for the PMD ranging system. An attractive solution of PMD ranging systems, the so-called PMD-PLL, is based on the principle of phase locked loop (PLL), where the differential output of PMD can be directly used to drive the VCO, which in turn offers the corresponding modulation signal of PMD, to the lock-in point, representing the phase delay of the back scattered optical signal. According to its structure, such PMD ranging system can be configured as open-loop PMD-PLL system [Rin-1][Rin-2] or closed loop system [Bux-4][Klein]. **Fig. 3.11** shows the block diagram of the PMD-PLL ranging system. The measurement accuracy

of the system is dominantly dependent of the lock-in precision of the PLL. The most significant advantage of this concept is the possibility of on-chip integration of PLL with PMD, offering another 3D PMD ranging solution. Another variant is the PMD-DLL ranging system based on the Delay Locked Loop (DLL), in which, similarly to the PMD-PLL, the phase of the PMD modulation signal is permanently locked into the zero-crossing of the wavelet of PMD [Bux-2]. The use of modern phase shifting techniques such as direct digital synthesizer (DDS) in the DLL ensures the high measurement precision.

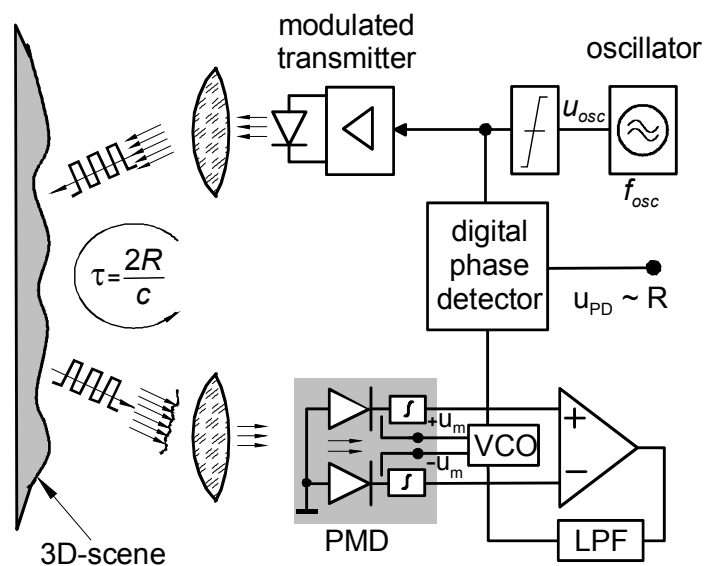


Fig. 3.10 Block diagram of the PMD-PLL ranging system [Rin-2]

4 Characterization of PMD pixel performance

In this section we report the experimental results for the different PMD structures. The measurement results give a quantitative description of the typical properties of PMD, which is the reference for further PMD investigation and redesign. The measurement provides also the specification for the PMD application.

4.1 Measurement setup, expectations and predictions

- **Optical measurement setup**

Fig. 4.1 shows the optical setup for the measurements of the PMD test pixels. The PMD test chip is mounted on a XY-plate. The position of a PMD pixel can be finely adjusted either manually or by means of a computer controlled high precision positioning nanomover. As the light source, a laser (or LED if necessary) module is used for the illumination of the PMD. The light beam is exactly focused through a pinhole and the lens system on the optical active area of the PMD, with a large adjustable range of optical power. By changing the illumination intensity and the size of the light spot, the total optical power exposed to the optical active area of the PMD pixel can be controlled as required for different measurements.

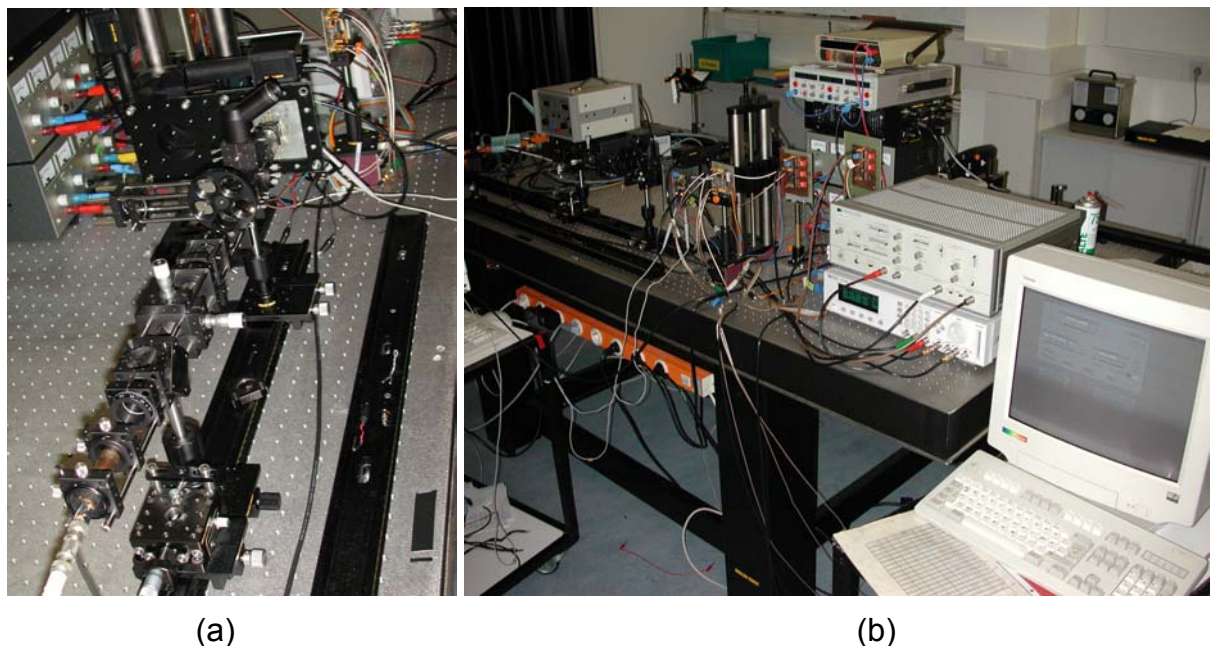


Fig. 4.1 Measurement system for PMD specification: (a) The optical setup for illumination of PMD. (b) The data acquisition, control and evaluation setup of PMD.

The modulation of the light signal and the demodulation signals of the PMD are generated by two square wave generators of high quality. The phase shifting, the amplitude, the frequency, the duty cycle and the rising/falling edges of the output signals can be adjusted in a large range. The analog outputs of the PMD are sampled using a 12 bit A/D converter. **Fig. 4.2** shows the configuration of the PMD pixel measurement system. Both signal generators are synchronized with each other. One of them is controlled by the host computer through the GPIB interface. Using the strobe out of the signal generator as the reference signal, the timing module generates the necessary control signals for the PMD read out circuit and the sampling module that accomplishes the digitizing of PMD analog outputs automatically. The integrated control software allows an easy modification of all parameters and therefore rapid measurements, either automatically or manually.

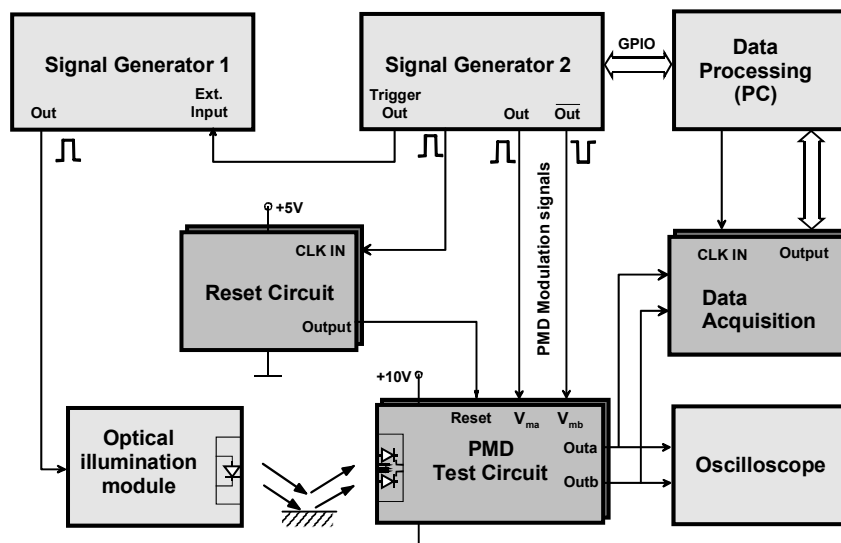


Fig. 4.2 Block diagram of the PMD pixel measurement system.

The optical power of the pixel illumination is controlled through the corresponding neutral density filters or the polarization plates, rather than the direct light density control by using electrical methods, e.g. by controlling the amplitude of the modulation signal of the laser module. This ensures a very flexible and accurate adjustment of the optical intensity without introducing additional phase errors in the RF-modulation signals.

- **Optical input and PMD modulation signals**

The optical signal is square wave intensity modulated. To ensure the correct and reliable evaluation from the measurement results of the PMD, stable modulation signals of high quality are required. The applied digital signal generator – HP8110A – provides a wide range of frequency modulation up to 160MHz and high precision of phase-shifting. Compared to the digital signal generator, it is quite more difficult to get the modulated optical output satisfying the requirement within the whole modulation frequency range. **Fig. 4.3** shows the measured modulated optical output signal of an 635 nm laser module used in the experiments and the corresponding demodulation signals of PMD, as reference, for different modulation frequencies.

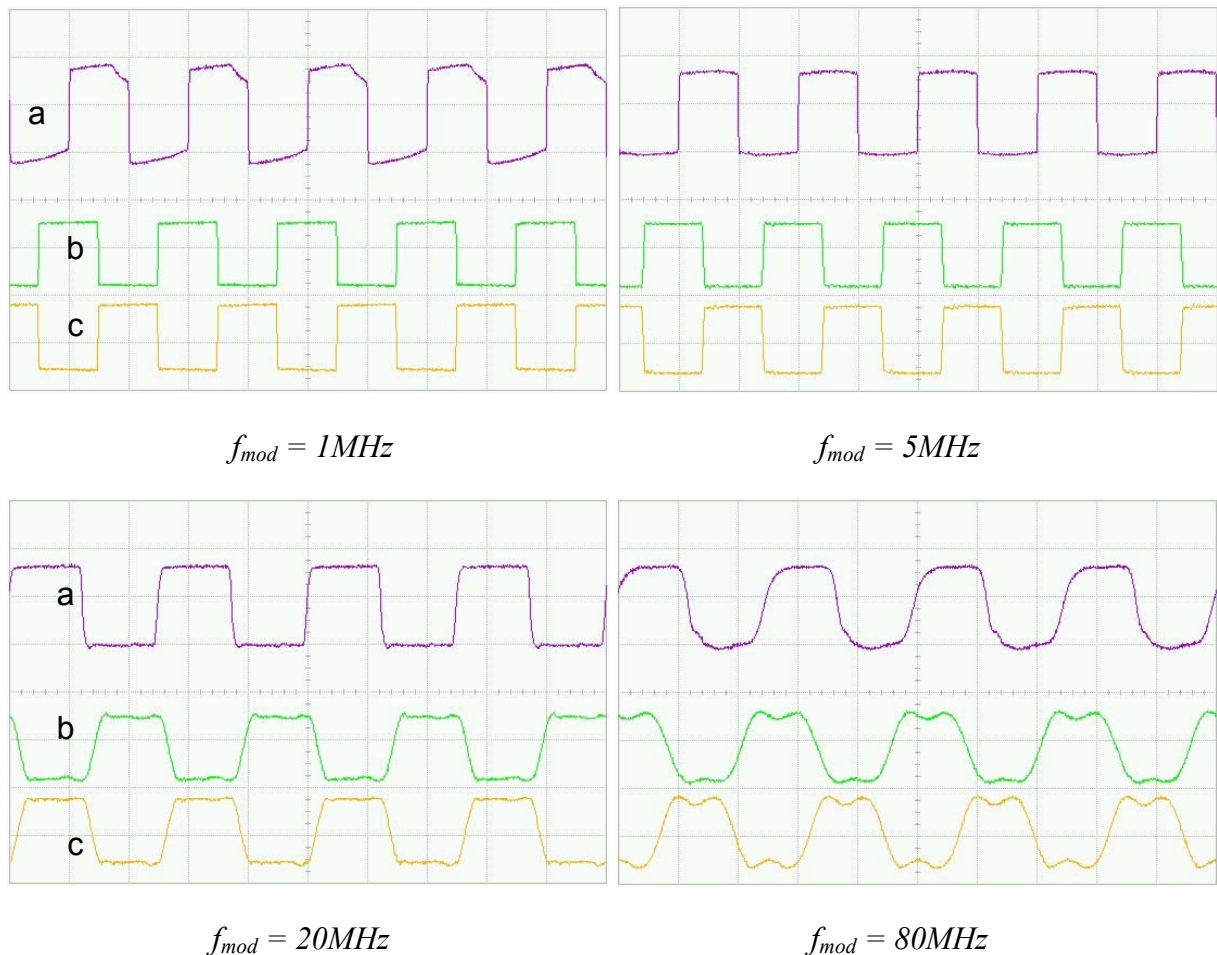


Fig. 4.3 Optical signal and modulation signals of PMD for different frequencies. Laser module: GFO-KD6304P, $\lambda = 635nm$, $P_{max} = 3mW$; Optical detector: FEMTO HSA-S. a: optical signal, b - c: PMD modulation signals U_{am} and U_{bm} .

One can see from the measurements that the fluctuation in the frequency band of the laser module leads to a distortion of the square wave signal and worse modulation depth for lower frequencies. So for the measurement of PMD in low frequency range another laser module was applied. Due to the low-pass characteristic of the applied laser module the optical output signal looks gradually sinusoidal for frequencies at the higher end (i.e. for $f_{mod} > 100\text{MHz}$).

Like many other laser diode modules, the total optical output power of the light source applied in the PMD measurements can not remain constant within the whole frequency band. The optical power reached an maximum at $f_{mod} \approx 2\text{MHz}$ and maintained nearly unchanged for higher modulation frequencies, where the most measurements were performed for the PMD specification. As described in the previous section, additional optical filters were used between the optical light source and the PMD test chips, ensuring a precise and flexible adjustment of the required optical power for the pixel illumination. This makes the measurement relatively independent of the optical performance of different light sources applied for modulated illumination in the measurement.

4.2 The spectral responsivity

As a semiconductor device, the spectral responsivity of PMD depends on many factors. Firstly, the absorption coefficient is dependent of the wavelength of the optical signal. For light of long wavelength it has normally a deeper penetration length in the semiconductor bulk. Since the PMD is in principle a surface semiconductor device, the probability that the generated charge carriers are detected decreases as they are generated further away from the surface, an effect leading to lower the spectral responsivity. On the other hand, for the optical signals with very short wavelength, the absorption of photons occurs already in the covering thin-film layers (passivation layers and polysilicon layers) resulting in weak responsivity towards blue light and UV. In addition, the thin-film multi-layer structure can cause the interference effect in certain wavelengths, resulting in the spectral response fluctuation.

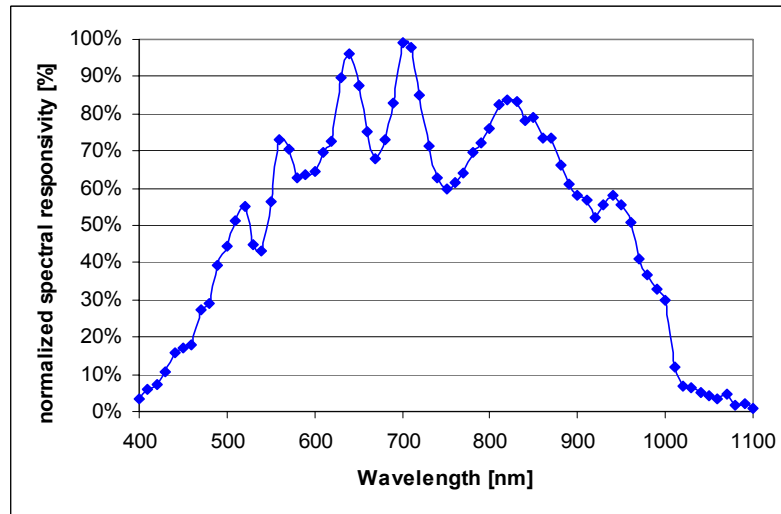


Fig. 4.4 The measured spectral responsivity of a typical PMD pixel realized in CMOS-technology. Test pixel: STP20-2F-No.7-T2. The PMD modulation frequency: $f_{mod} = 20\text{MHz}$. $t_{rise} = t_{fall} = 4\text{ns}$.

The measurement was carried out based on a PMD test pixel with finger structure fabricated from the T2 – process. The spectrum analyzer [INS] was used to generate light of the required wavelength in a range of from 400nm to 1100nm, based on a white light source coupled to the instrument. The quantum efficiency of PMD referred to the wavelength of the light can be calculated due to both the optical power of illumination and the correspondingly generated photo current

$$\eta(\lambda) = \frac{i_{PMD}(\lambda)}{P_{opt}(\lambda)} \quad (4.1)$$

where P_{opt} is the measured optical power referred to different wavelength and i_{PMD} the total generated average photo current which can be obtained according to the measured output voltage at both output channels A and B of PMD

$$i_{PMD} = i_a + i_b = \frac{C_{int} \cdot (\Delta U_a + \Delta U_b)}{T_{int} \cdot G} \quad (4.2)$$

in which C_{int} is the integration capacity of the PMD pixel, G the gain factor of the corresponding readout driver, ΔU_a and ΔU_b the outputs of PMD at the end of the integration time interval T_{int} . The measured results of a PMD pixel was illustrated in **Fig.4.4**. As mentioned above, one can see the interference peaks appeared in the

measured spectral responsivity curve. Based on the measurement result, the laser modules with the wavelength of $\lambda = 635\text{nm}$ was selected for the specification of PMD.

4.3 Transfer characteristic of PMD

As already discussed in section 3.3, the transfer characteristic describes the charge handling capability of PMD, as well as the modulation linearity and modulation dynamic as an eletro-optical modulator on the other hand. Since the outputs of the PMD are proportional to the input optical power under the same integration time condition, which is directly measured in the experiment, the transfer characteristic corresponds to the ratio between the outputs of PMD and its modulation gate voltage. In the experiments the optical sensitive area of the pixel was exposed to a constant illumination. Both the outputs ΔU_a and ΔU_b of PMD were measured as the amplitudes of the gate modulation signals varied step by step from 0V to 0.8V, with an offset voltage set at $U_{offset} = -0.45\text{V}$. **Fig. 4.5** shows the typical output signals of PMD at a modulation frequency of 20 kHz. The measurement results based on a $60\mu\text{m}$ two-gate PMD test structure and an optimized short-channel PMD finger structure are illustrated in **Fig. 4.6**. The output of the PMD was normalized due to the fact that the total generated charge of PMD remains constant.

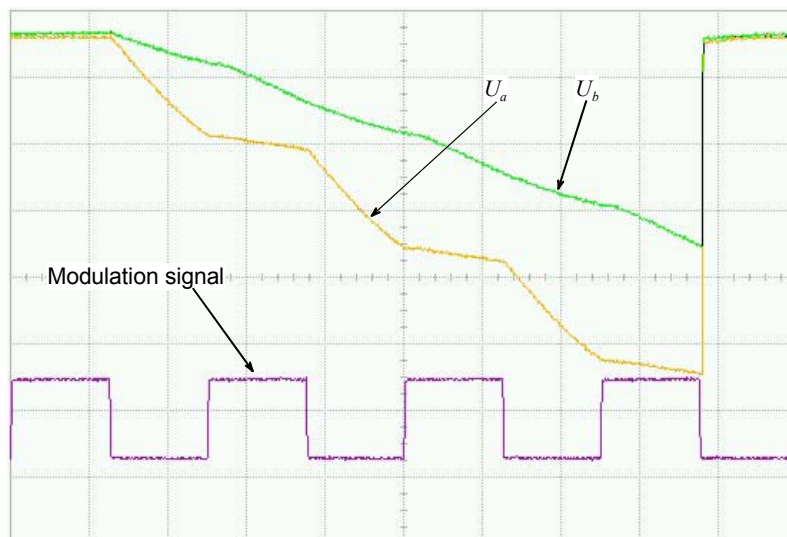


Fig. 4.5 The measured output signals of a PMD pixel under the modulation frequency of $f_{mod} = 20\text{ KHz}$.

From the results it can be seen that an area of high linearity appears in the middle of the curves where the outputs of PMD keeps quasi-linearly the changes of the modulation amplitude. With the amplitude of modulation of approximately 500mV the PMD reached the maximum charge separation efficiency. Further increase of the amplitude of modulation signals has not longer contribution to charge transfer ability of PMD. The high charge separation capability of PMD under small modulation signals leads to high sensitivity of the new device, compared to the other EO modulators. The results keeps very good with the expectations and the simulations in the previous researches [Xu-1] [Bux] [Fri].

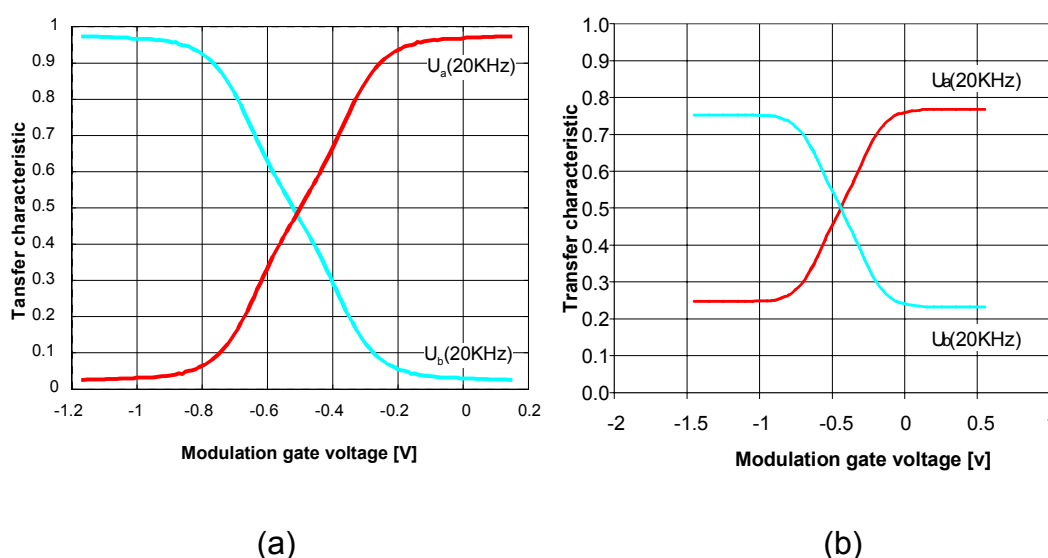


Fig. 4.6 The measured transfer characteristic of different PMD test pixels: a) the measured curve of a $60 \times 60 \mu\text{m}^2$ 2-gate PMD. b) The measurement of the PMD pixel with $17.5 \mu\text{m}$ finger structure.

The fact that the maximum charge separation doesn't reach the limit of 100%, as have been discussed in the previous sections, is mainly due to the surface potential distribution in the optical sensitive area of the PMD, as shown in **Fig. 3.5**. Independent of the modulation frequency and signal forms, there is permanently a little amount of the total generated charge flowing to the adjacent connected readout diode, resulting in an inefficiency of charge separation. Further reasons might be e.g. charge diffusion and the

dark currents of PMD and the effects of corresponding readout circuits [Scw-5][Xu-1]. Although the two-gate PMD structure shows, as depicted in **Fig. 4.6a**, relative more effective charge separation, one should keep in mind that not only the modulation amplitude but also the modulation frequency has influence on the transfer characteristic of PMD, as already mentioned before. And the latter is more important since the TOF ranging requires normally rather high modulation frequencies. Compared to the short channel PMD, its modulation performance could be restricted at high frequency since the transfer efficiency in this case is much lower due to the longer gate length. In addition the larger modulation gate of PMD leads to a high lateral sensitivity. Inhomogeneous illumination causes unsymmetrical output signals which introduce a DC offset, however, this lateral effect can be compensated using the PMD finger structure.

4.4 Modulation contrast and dynamic range of PMD

The modulation contrast of the PMD is another important feature judging the performance of the charge separation in the PMD. It describes the maximum charge separation capability of a PMD structure which can be obtained, without consideration of such factors as non-linearity and asymmetry. In optics the modulation contrast is defined as follows:

$$K_m = \frac{I_{\max} - I_{\min}}{I_{\max} + I_{\min}} \quad (4.1)$$

For PMD, the outputs at the end of the integration time present a direct measure of PMD. The modulation contrast is similarly defined as:

$$K_{PMD} = \frac{\Delta U_{\max} - \Delta U_{\min}}{\Delta U_{\max} + \Delta U_{\min}} \quad (4.2)$$

Here ΔU is the measured difference between the reset voltage and the corresponding output of PMD at the end of the integration. We remind that the modulation signals applied to the PMD gates are push-pull square signals, which means, if the output in one of the PMD output ports A and B reaches the maximum, the minimum will arrive at the same time in another channel. With consideration of the possible asymmetrical effect caused by inhomogeneity of illumination and the duty cycle of the modulation signals, the contrast is evaluated based on two measurements, one with 0° phase shifting and one with 180° phase shifting. Equation (4.2) is then modified by

$$K_{PMD} = \frac{1}{2} \cdot \left(\left| \frac{\Delta U_a(180^\circ) - \Delta U_a(0^\circ)}{\Delta U_a(180^\circ) + \Delta U_a(0^\circ)} \right| + \left| \frac{\Delta U_b(180^\circ) - \Delta U_b(0^\circ)}{\Delta U_b(180^\circ) + \Delta U_b(0^\circ)} \right| \right) \quad (4.3)$$

with $\Delta U_a(0^\circ)$ and $\Delta U_b(0^\circ)$ defined as the outputs of both PMD ports A and B , when the modulated light signal is in-phase with the signal at gate A , and $\Delta U_a(180^\circ)$ and $\Delta U_b(180^\circ)$ as the corresponding outputs of PMD when the optical signal and the modulation signal of the gate A are out-phase.

Instead of directly measuring the incident optical power each time, we use the averaging constant photo current which can be easily obtained in the experiments. The photo current is calculated according to equation 4.4

$$\bar{i} = \frac{C_{int} \cdot \Delta U_a(90^\circ)}{T_{int} \cdot G} \quad (4.4)$$

in which $\Delta U_a(90^\circ)$ the output of PMD for the case of 90° phase shifting of the signal on gate A over the integration interval T_{int} , referred to the modulated optical signal. For a given modulation frequency f_0 , equation (4.4) can be calculated as follows:

$$\bar{i} = \frac{C_{int} \cdot \Delta U_a(90^\circ) \cdot f_0}{N_{int} \cdot G} \quad (4.5)$$

with N_{int} the corresponding integration periods at the integration time interval T_{int} . In the following sections the influences of several factors such as the modulation frequency, intensity of the illumination and signal forms *etc.* on the performance of PMD will be discussed based on the results of the measurements.

4.4.1 Frequency characteristic of PMD

Frequency characteristic of PMD defines the relation between the modulation performance of PMD and the modulation frequency. It is apparent that higher modulation contrast contributes to a better phase accuracy which leads to higher distance accuracy, as discussed later at the last part of this document. In this measurement the modulation frequency was changed step by step while the optical intensity of the pixel illumination was set fixed at the value that corresponds to an average photo current of $\bar{i} = 3nA$, which was calculated by using equation (4.5) when both outputs of PMD were, after the same integration period T_{int} , also fixed, i.e.

$\Delta U_a = \Delta U_b = \Delta U(90^\circ)$ in the case of 90° phase shifting, as described above, during the whole frequency range. Since the optical power of the laser varies in the frequency range as mentioned previously, the incident optical intensity should be adjusted each time through additional optical filters before the measurement is started.

The measured curves for a typical two-gate PMD pixel with $60\mu\text{m}$ gate length and a PMD $17.5\mu\text{m}$ -finger structure are presented in **Fig. 4.7**. As one would expect, though the simple 2-gate PMD pixel of large modulation gate reaches a high modulation contrast at low modulation frequency, the modulation contrast breaks down very quickly as the frequency increases due to its long channel length. In comparison, the finger structure PMD pixel with the shorter channel has relative constant modulation contrast over a large frequency range, the -3dB frequency is about 150MHz , neglecting the influences of the signal form distortion of the optical and demodulation signals, as shown in **Fig. 4.3**. This is of essential importance for the distance measurement with CW- or PN-modulation techniques, since the large modulation contrast and the high modulation frequency ensures both the distance accuracy and resolution.

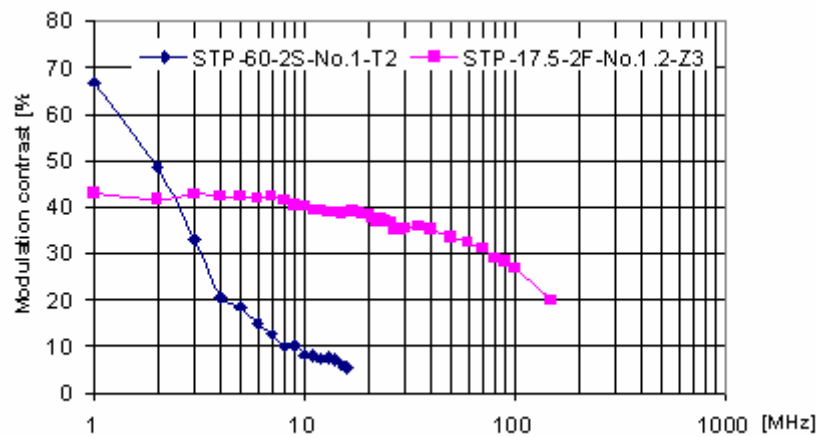


Fig. 4.7 PMD modulation contrast versus frequency.

4.4.2 Influence of the optical intensity on the PMD performance

The optical reflection from the targets varies in the practice very strong due to the surface characteristics of the materials. As the key component for the optical ranging sensors, the behavior of the PMD under different illumination conditions needs to be

studied. Different from typical image sensors, the PMD gives not only the information of the reflected intensity (gray tone) but additionally the phase information. The modulation contrast is the judgment of the PMD performance under different illumination conditions. Similarly to the measurement of the modulation contrast vs. frequency, the PMD pixel was exposed directly to the modulated optical signal, which simulates the reflected optical signal. The optical intensity is controlled by the corresponding optical attenuation filters. The modulation frequency is fixed at $f_0 = 20\text{MHz}$ and other parameters remained the same as in the frequency measurement described in the last section. Instead of measuring the optical power directly, the average photo current was measured based on the PMD outputs. **Fig. 4.8** illustrates the measured results of a PMD test pixel with finger structure.

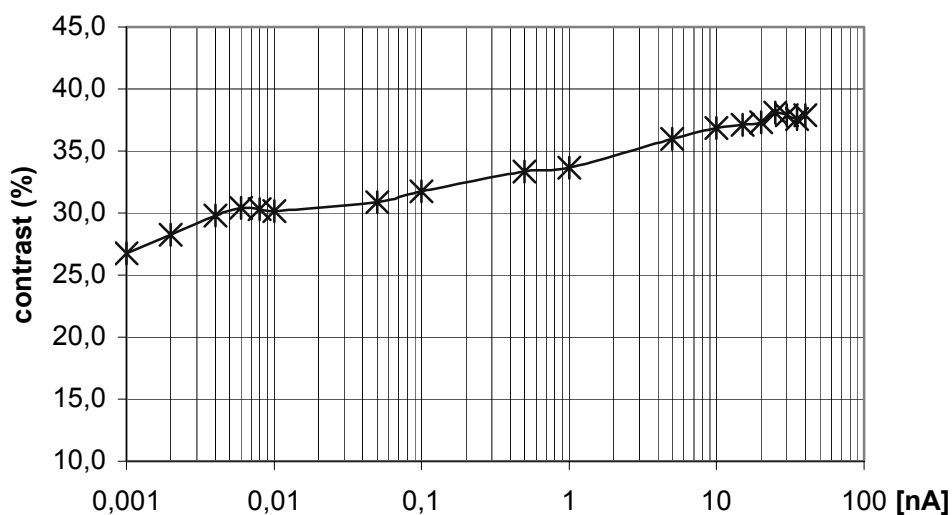


Fig. 4.8 Modulation contrast of PMD vs. photo current.

Testchip: STP17.5-2F-SG-No.2-Z3. Modulation frequency: $f_0 = 20\text{MHz}$.

We see that although the intensity of optical illumination has also influence on the modulation contrast, the PMD pixel delivers still an excellent performance even at extremely weak illumination. The modulation contrast of PMD suffers only a declination of about 11% at an optical attenuation of over 100dB.

4.4.3 The correlation characteristic of PMD

As have been discussed in the last chapter, the PMD is an eletro-optical mixer that performs the correlation of the back scattered RF-modulated optical signal with the PMD modulation signal. Since both the optical RF-signal and the demodulation signals are based on the same signal source, the outputs of PMD can be considered as the product of the auto-correlation of the modulation signals. It is a function of the phase delay induced by the distance of the object. This function gives a direct description of the influences of such factors as system non-linearity, band limitation and signal form distortions. For an ideal PMD without such limitations, the auto-correlation function has a form of sinusoidal function if both the illumination and the PMD are sinewave modulated, and a form of trigonometric function for square wave modulation.

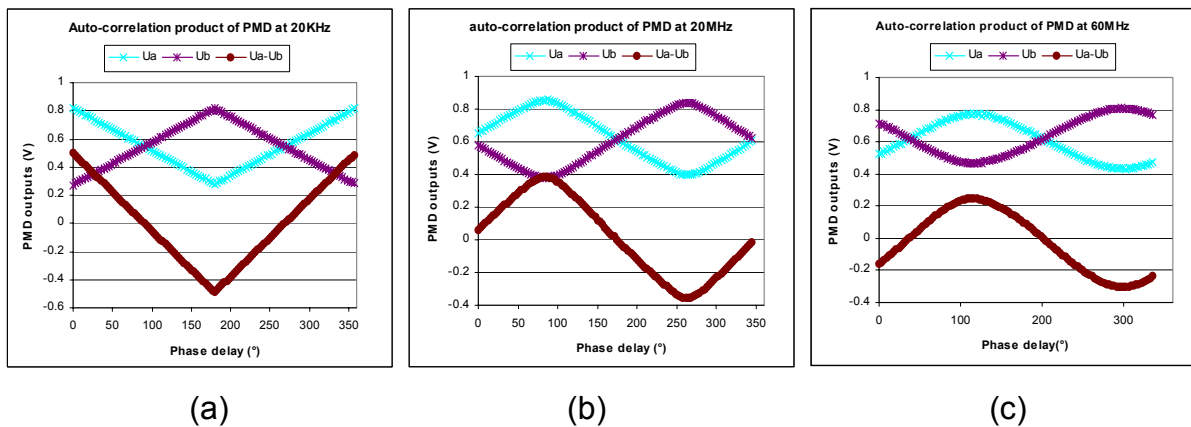


Fig. 4.9 The measured curves of a finger structure PMD pixel STP-17.5-2F-SG-No.2-Z3. (a) The outputs of PMD at a modulation frequency of 20 kHz, (b) the measurement at 20 MHz, and (c) the measured curve of PMD at 60 MHz.

In the experiments, the measurement condition was kept the same as in the measurements described above, with exception that the phase delay of the optical signal was simulated by incrementally changing the phase shifting of the modulation signal. The curves were measured with different modulation frequencies. The results of a PMD test pixel with finger structure at the modulation frequencies of 20 kHz, 20 MHz and 60 MHz respectively are presented in **Fig. 4.9**. The different initial phase offsets shown in the graphics are due to intrinsic additional phase delays induced from the

connected cables and filters in the measurement system at different frequencies, as already mentioned in the previous sections.

We see that the correlation result of the PMD at low frequencies in case of square wave modulation shows the exact trigonometric form. The differential output of PMD contains a linear relation with the phase delay of the optical signal within the range of 2π . With the further increase of modulation frequencies, however, the correlation performance of the PMD will be more and more attenuated due to the band limitation of the PMD. The correlation curve of PMD at a high modulation frequency comes gradually to the form of a sinusoidal function, since the contribution of high order harmonic terms decreases considerably, as depicted in the measured result of PMD pixel at 60 MHz. The linear region of the correlation curve is much more restricted than in the cases of lower modulation frequencies.

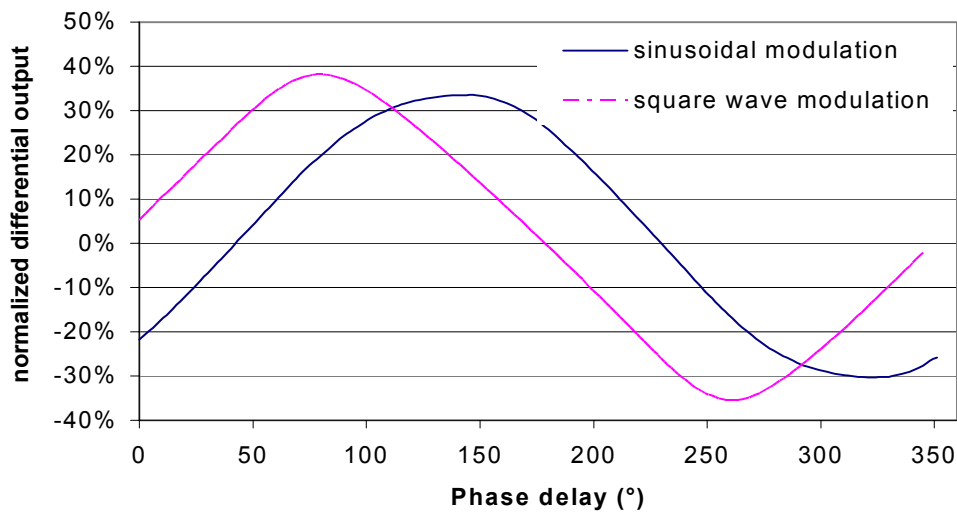


Fig. 4.10 The correlation results of the PMD pixel measured with sinusoidal and square wave modulations at 20 MHz and $i_{photo} = 1\text{nA}$. The optical signal was, however, squarewave modulated in both cases. The initial phase offset is caused by the low-pass filter.

With reference to the square wave modulation, we measured the correlation output of PMD in another experiment, letting only the modulation signal at the modulation gates of PMD sinusoidal modulated and the optical signal remaining further square wave

modulated. The results of measurement are presented in **Fig. 4.10**. The measured curve has the same form of a sinusoidal function that is the same as in the case of sinusoidal modulation on both the optical and the PMD sides. This is quite easy to understand. The Fourier expansion of the square wave optical signal can be explained as

$$s'(t) = \frac{1}{2}a'_0 + 2a'_0 \left(\frac{\cos 2\pi f_0 t}{\pi} - \frac{\cos 3 \cdot 2\pi f_0 t}{3\pi} + \frac{\cos 5 \cdot 2\pi f_0 t}{5\pi} + \dots \right) \quad (4.6)$$

Compared to equation (2.10), we see that all even coefficients a'_n and all b'_n in the expansion are zero. In case of sinusoidal modulation at PMD gates, so only the DC part and the coefficient of the fundamental harmonic remain in equation (2.9), resulting that all the high order terms of harmonics disappear in the RF-interferogram described by equation (2.15), i.e.

$$M_n = 0 \text{ for all } n > 1 \quad (4.7)$$

This result is in the practice very interesting for the distance measurement using phase-shifting method, in which LEDs and laser diodes are usually used as light source. Firstly the square wave modulation of LEDs or laser diodes is easier to realize than the sinusoidal modulation and secondly a large modulation depth of up to 100% can be reached. Since the contribution of high order harmonic waves do not appear in correlated outputs of the PMD, so just a 4-phase shifting method could satisfy the requirements in the most 3D-ranging applications, where the time consume of the corresponding data processing, measurement rate, and the hardware cost would grow drastically with increasing dimensions of the sensing array.

4.4.4 Lateral effect and unsymmetrical modulation of PMD

In this section we present the measurements showing the influence of the lateral effect on the PMD modulation characteristic, based on two typical PMD structures: the simple two-gate PMD and the finger structure PMD. Both PMD structures are illustrated in **Fig. 4.11**. The lateral effect may arise in practice from the inhomogeneous illumination, strong contrast scene or near the edges of 3D object. In the experiment we simulated this situation by placing the modulated light spot at different positions within the optical active sensing area of PMD pixel, as shown in **Fig. 4.11a**. For the two-gate simple PMD structure, the change of position of the light spot leads to unbalanced outputs of PMD.

The measured correlation curves related to the three light spot positions are illustrated in **Fig. 4.11 (a1-a4)**. It is apparent that the lateral effect will induce unsymmetrical modulation of PMD, resulting in a DC offset at the discriminator output ΔU_{ab} of PMD which is dependent of the light spot position or inhomogeneity of illumination.

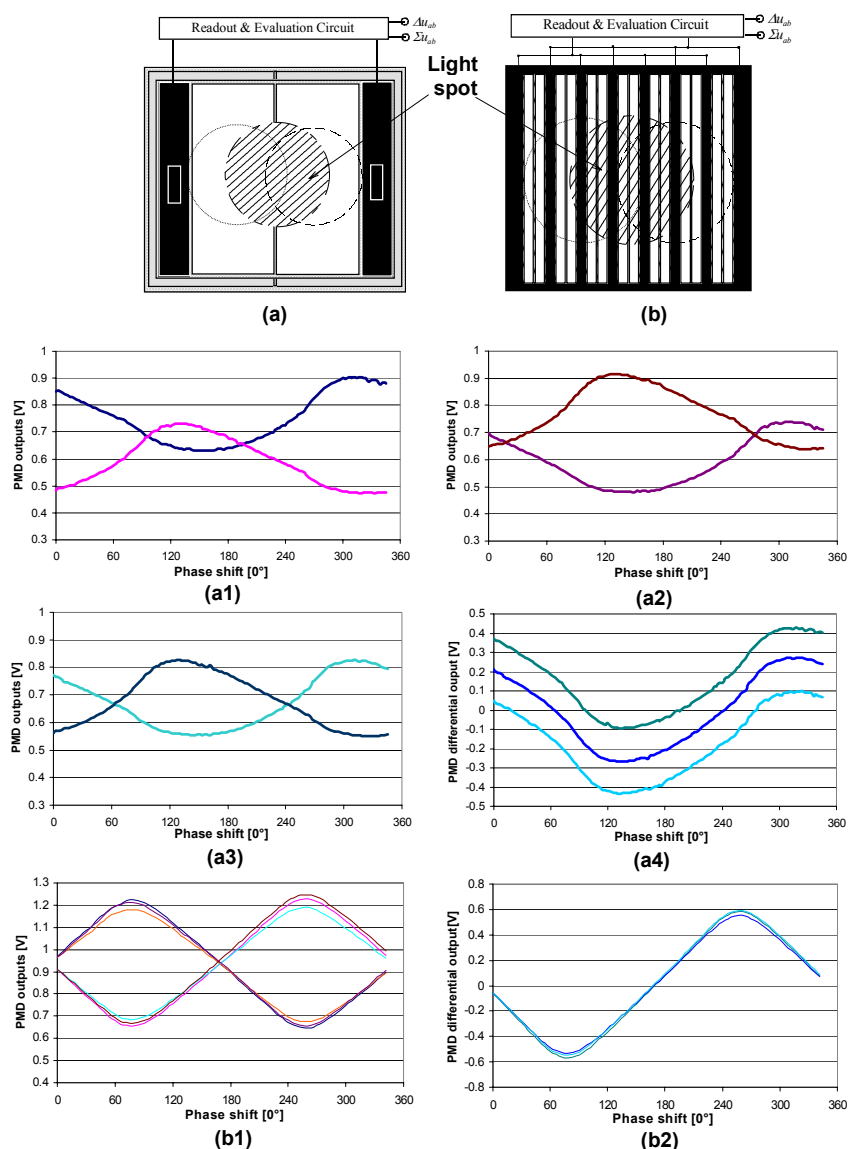


Fig. 4.11 The lateral effect and the PMD structure. a-b: The schematic presentation of lateral effect. a1-a4: The measurement results of a 2-gate PMD: STP60-2S-No.1-T2. b1-b2: The results of the finger structure PMD: STP17.5-2F-No.2-Z3.

This effect is undesirable in the TOF ranging measurement. Although it can be eliminated through the multi-phase shifting evaluation algorithm in the ranging system based on the heterodyne-modulation technique, as discussed later in the following chapters, it may induce distance error in some ranging methods based on the localization of zero-crossing. The best solution to overcome this problem is the implementation of PMD finger structure. It increases not only drastically the operation frequency of PMD, the influence of lateral effect on outputs of PMD is also considerably suppressed, ensuring steady symmetrical modulation outputs, as illustrated in **Fig. 4.11 (b1 and b2)**.

4.4.5 Noise performance and dynamic range

For PMD the main noise sources are photo generated shot noise, dark current shot noise, Trapping noise, KTC noise (reset noise) and flicker ($1/f$) noise [Xu-1]. Among these noise sources the photo shot noise is the dominant noise source in the PMD device. Usually the signal to noise ratio SNR and the dynamic range DR are used to judge the noise performance of a sensing device. From the engineering point of view, the SNR is calculated by

$$SNR = 20 \cdot \log\left(\frac{\Delta U_{signal}}{\Delta U_{noise}}\right) \quad (4.8)$$

where ΔU_{signal} is the voltage swing of the output signal and ΔU_{noise} the rms noise voltage at the output. Compared to the signal to noise ratio, the dynamic range DR of imaging sensors is usually defined as the ratio of the maximum voltage swing ΔU_{max} and the minimum rms noise floor, i.e. dark noise $\Delta U_{dark\ noise}$

$$DR = 20 \cdot \log\left(\frac{\Delta U_{max}}{\Delta U_{dark\ noise}}\right) \quad (4.9)$$

In the practice the dynamic range of PMD is defined as the maximum signal to noise ratio that equals

$$DR = SNR_{max} = 20 \cdot \log\left(\frac{\Delta U_{max}}{\Delta U_{noise}}\right) \quad (4.10)$$

If not taking the noise sources of the readout circuit of PMD into account, the dynamic range could be approximately estimated by using the equation [Xu-1]

$$DR = 20 \cdot \log(\sqrt{N_{photo}}) = 20 \cdot \log(\sqrt{\Delta U_{max} C_{int} / q}) \quad (4.11)$$

with N_{photo} the maximum charge to be collected in the total effective integration capacitance of PMD C_{int} . We see that a large voltage swing and integration capacity will increase the dynamic range of PMD, but on the other hand, the large capacitance will reduce the sensitivity of the photo detection. The maximum voltage swing is typically designed in a range of 1~3V.

A precise measurement of the noise performance of the PMD pixel is rather difficult. In the measurement, it is not possible to separate exactly the noise sources as mentioned above, also the noise sources of the related readout circuits contribute to the measured results. Additional noises from the different parts of the measurement system such as voltage supplies and signal generators might influence the accuracy of evaluation. Nevertheless, the measured results could give an approximation to the description of the PMD noise performance after careful experiment preparations. **Fig. 4.12** shows the measured noise signal at the output of the PMD and the corresponding histogram. With the consideration that the noise of the oscilloscope itself is not correlated with that of the measured system, the measured standard deviation of the total noise signal is measured at about 0.64mV. The measurement condition and the test pixel are just the same as in the contrast measurements. The measured dark current of the PMD pixel is $I_{dark} = 0.13pA$. Referred to the obtained results, the dynamic range of the test PMD pixel corresponds to $DR = 71dB$.

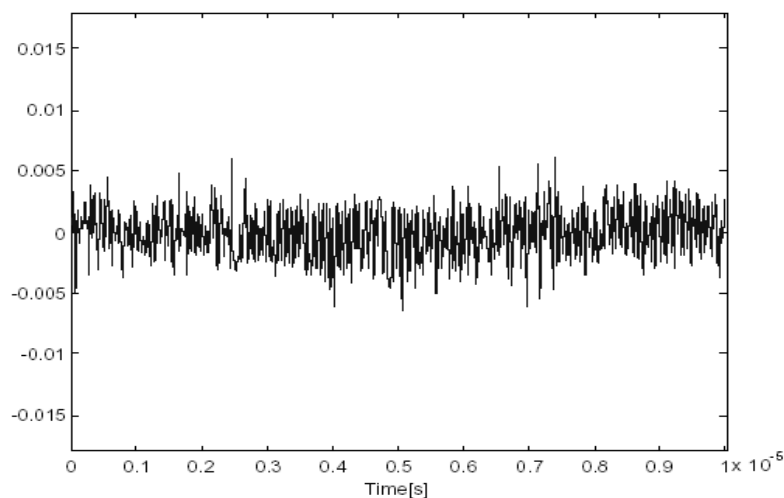


Fig. 4.12 The measured noise signal superimposed on one output channel of PMD.

Similarly to CMOS imaging sensor, the fixed pattern noise (FPN) due to the non-uniformity of the pixels and periphery circuitry is also typical for PMD, which can be eliminated by using the so called correlated double sampling (CDS) technique [WeGu]. As demonstrated later in the discussions in this thesis, the FPN noise, similarly to the asymmetry effect induced from the inhomogeneous pixel illumination, could be directly suppressed in the distance measurement based on the multi-phase shifting evaluation algorithms without additional CDS circuitry, since the FPN noise of an PMD pixel remains nearly unchanged from different reset frames, which can be considered as DC part in the PMD output. **Fig. 4.13** shows the measured result of the FPN of a PMD line sensor with 24 PMD pixels.

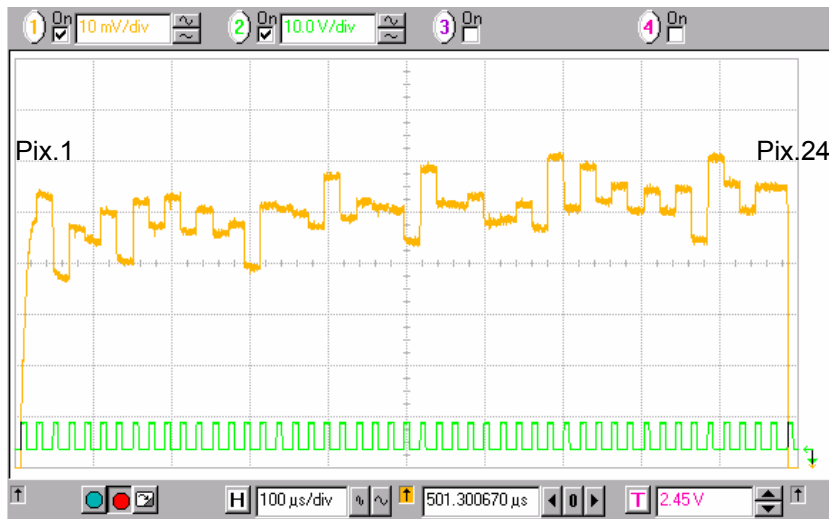


Fig. 4.13 The fixed pattern noise of a PMD line sensor with 24 PMD pixels. The integrated charge of each PMD pixels is serially read out in the order of $A_1, B_1, A_2, B_2, \dots, A_N, B_N$.

4.5 Influence of the background illumination

Referred to the fixed pattern noise, the influence of the background illumination is more important for the PMD device. **Fig. 4.14** demonstrates the performance of PMD in presence of the background illumination. Compared to the case with the pure active illumination shown in **Fig. 4.14a**, the differential output of the PMD has no change with additional background illumination (**Fig. 4.14b**). This property of PMD shows that the background illumination will not lead to additional phase error, since the background

illumination contributes to the common part in the PMD output signals due to the balanced mixing functionality of PMD and can be then completely eliminated from the differential output of the PMD. On the other hand, the presence of the background illumination will reduce the dynamic range of PMD which in turn increases the measurement uncertainty of the ranging system. This can be explained using the concept of modulation contrast. In practice the output signal is usually digitized before being further evaluated. Large modulation contrast will increase the accuracy due to its larger dynamic range for AD-conversion. Assuming K_{PMD} is the modulation contrast of the PMD, as defined in equation (4.2), under additional background illumination, however, the equivalent modulation contrast K of PMD is restricted to

$$K = \frac{K_{PMD}}{1 + P_{background} / P_{opt}} \quad (4.12)$$

where P_{opt} and $P_{background}$ represent the power of optical modulation signal and power of background illumination, respectively. The equivalent contrast decreases with an increase of background illumination.

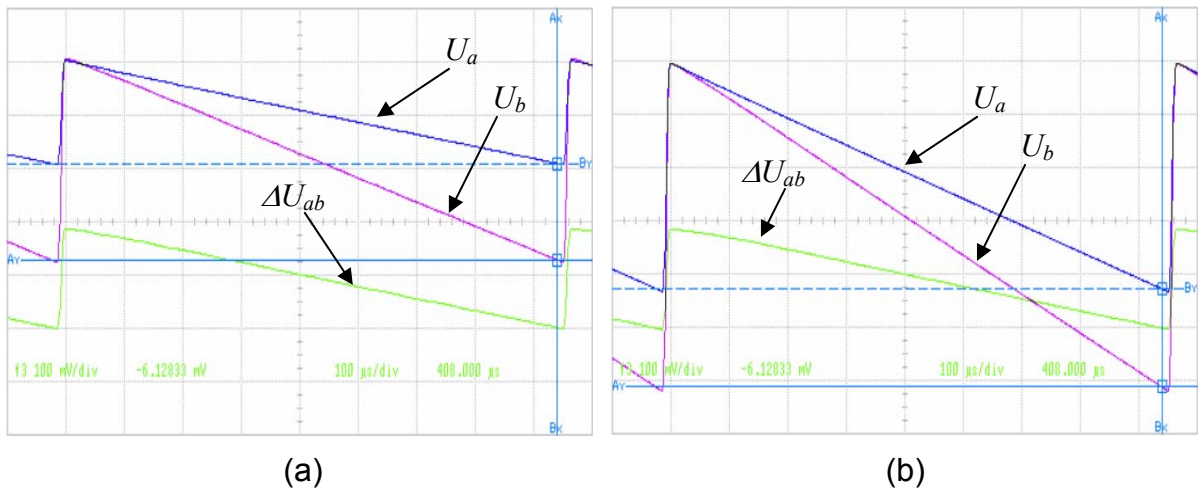


Fig. 4.14 (a) The output signals of PMD during the integration period exposed only to the illumination of optical signal. (b) The outputs of PMD with additional illumination of background light. The differential output ΔU_{ab} remains unchanged in both cases.

The PMD pixel introducing the on-chip background illumination suppression (SBI) circuit can considerably reduce the influence of the background illumination [He-1]. The dynamic range of PMD can thereby be maintained almost unchanged without much loss

of the resulting contrast. **Fig. 4.15** gives a measurement result of the first test PMD pixel with the SBI functionality. Compared to the result in the absence of background illumination, the measured distance in the case of about 20dB background illumination shows a distance error of less than 4.5cm. The new concept of MSM-PMD gives a more effective solution for suppressing the influence of background illumination. Due to the new kind of operation principle of MSM-PMD, both large dynamic and high modulation contrast can be achieved [Scw-7][Bux-5].

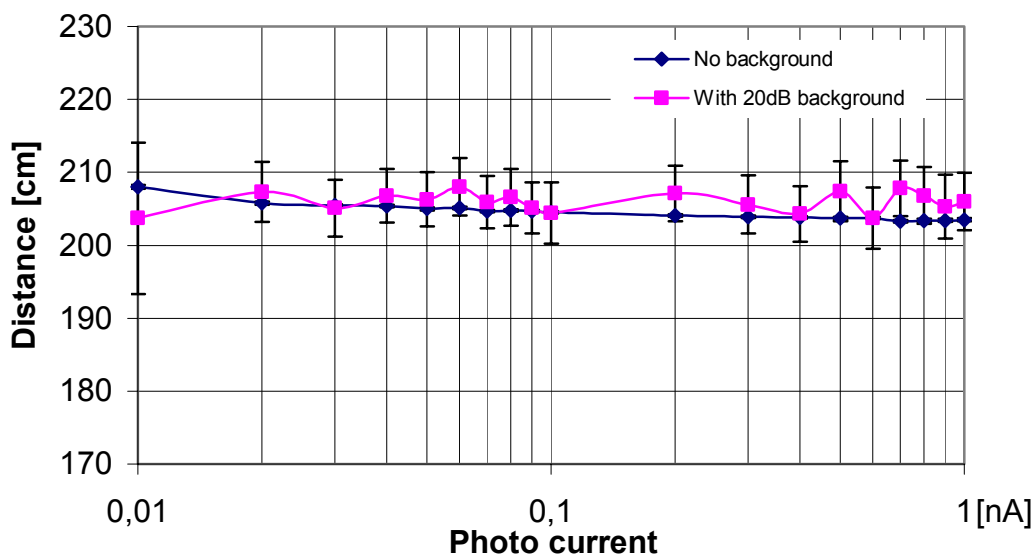


Fig. 4.15 The suppression of the background illumination of a PMD pixel with SBI circuit. $f_{mod} = 20\text{MHz}$.

4.6 Non-linearity measurement

All the discussions we made yet are under the assumption that the PMD operates in the linear region. In the case of the square wave modulation the correlation function of PMD shows the high linearity in a large range of phase delay at a modulation frequency of 20MHz, as shown in **Fig. 4.10**. Besides the non-linearity of PMD transfer characteristic itself, the saturation of charge collection must be also taken into account. In 3D ranging, the reflected optical signal varies normally in a wide range due to the strong image contrast and distinct surface characteristics in a 3D-scene, in the worst case over 100dB. For very strong reflection the integration of PMD drives very quickly into the

saturation, resulting in non-linear operation of the PMD. Such situations can be simulated in the experiment either through increasing the optical power or the PMD integration period. As illustrated in the **Fig. 4.16a**, the output of PMD is no longer linear due to the saturation effect. The corresponding correlation result of the PMD is demonstrated in **Fig. 4.16b**.

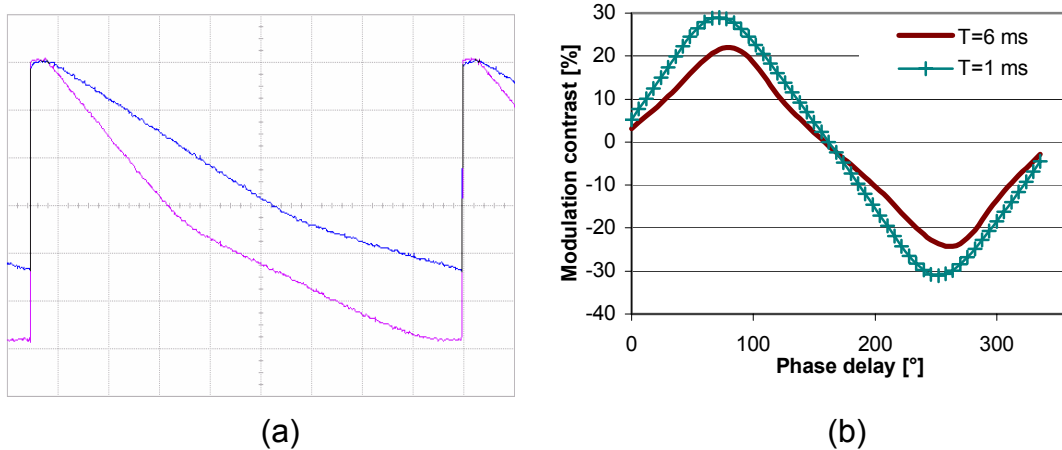


Fig. 4.16 (a) The output signals of PMD due to the saturation effect during the integration period. (b) The corresponding correlation curves of the PMD. The correlation result of PMD at $T_{\text{int}}=1\mu\text{s}$ without saturation effect is illustrated again as a reference.

We see that the correlation curve of PMD is distorted due to the saturation effect under the strong illumination and the distortion is dependent on the optical power or integration time. Of course the adaptive integration time control of PMD referred to the illumination can ensure PMD from the saturation, but this method is most suitable for ranging systems with a single PMD pixel or small PMD line/array. The phase shifting methods with the related evaluation algorithm can suppress the contributions of the high order harmonic waves significantly to the evaluation results [Xu-1].

Fig. 4.17 shows the measurement results employing the 8-phase shifting evaluation method. The distance evaluation was performed by using the corresponding evaluation algorithm described in section 2.2. Under the same experimental condition in the previous measurements with the illumination unchanged, the outputs of PMD at different phase shifting steps were sampled by 12 Bits AD-converter at different

integration time points, corresponding to the different voltage levels of the PMD output signals shown in **Fig. 4.16a**. The absolute measured distance value has no meaning in this experiment, it just represents the fixed phase delay introduced from the measurement system. The result shows very little fluctuation of the distance values at different sampling time of the whole integration period. The evaluation based on the 8-phase shifting method demonstrates the ability of suppressing the influences of the non-linearity problem induced from the saturation effect of PMD.

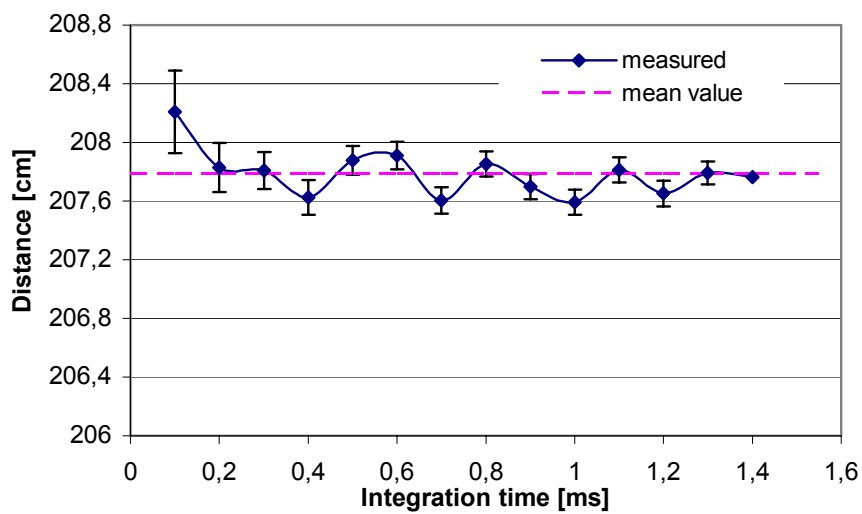


Fig. 4.17 The evaluated results based on the 8-phase shifting algorithm at different integration time, under the condition of fixed illumination power, corresponding to a photo current of $i_{photo}=5\text{nA}$. $f_{mod} = 20\text{MHz}$. The outputs of the PMD are sampled at different integration time.

4.7 Correlated balance sampling (CBS)

Finally, we discuss in this section the handling ability of PMD against the optical disturbing signals. We have known that PMD performs the correlation of the optical and demodulation signals. For a ranging system with CW-modulation, the optical signal is normally of the same frequency and the same signal form with the balanced demodulation signals on both PMD gates. This is the case which has been discussed in chapter two. In practice, the back scattered optical signal from the target includes not only the modulated optical signal but also the background illumination which contains

not always the DC term (e.g. fluorescent lamp). The influence of such disturbances on the PMD outputs should be discussed.

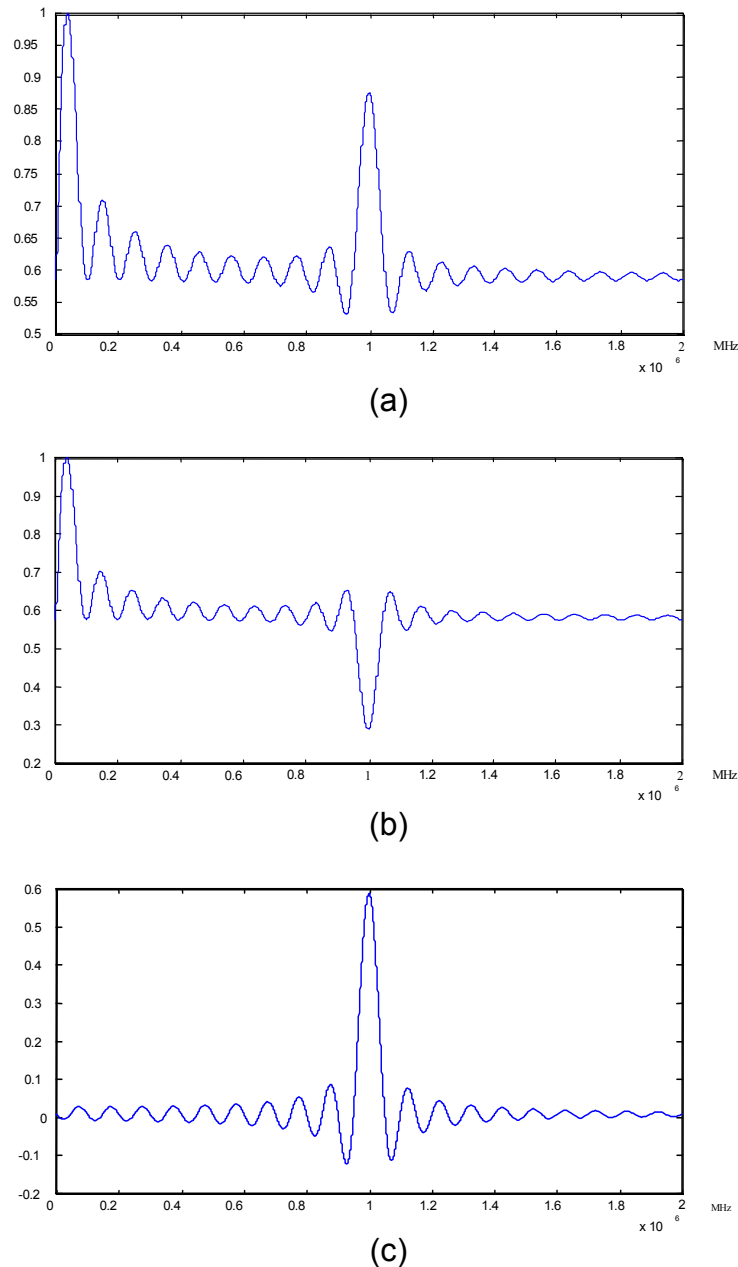


Fig. 4.18 The correlated balance sampling of PMD. (a) The maximum voltage swing of the output channel a of the PMD; (b) the output at the channel b of the PMD; (c) the corresponding spectral distribution of the PMD.

Because any periodic signal can be expanded into a Fourier series of different orders of harmonics, as defined in equation 2.9, for the simplicity, we consider the case of both

the disturbance and the PMD modulation signals with the form of sinusoidal waves of frequencies f_1 and f_0 respectively, as defined by equation 2.4 and equation 2.5. One output of PMD can be written by

$$I_a = I_0 \cdot [a_0 + a_m \cdot \cos(2\pi f_0 t)] * [a'_0 + a'_m \cdot \cos(2\pi f_1 t)] \quad (4.13)$$

As mentioned in the discussion of chapter two, the integration period of PMD ΔT is usually much larger than the modulation period, i.e. $\Delta T \gg 1/f_0$, using the orthogonal properties of the sinusoidal functions, we have the output of the PMD over the integration period $[k\Delta T, (k+1)\Delta T]$

$$I_a = I_0 \left[a_0 a'_0 + a_m a'_m \cdot \frac{\sin(\pi \Delta f \Delta T)}{\pi \Delta f \Delta T} \cdot \cos(2\pi \Delta f \cdot (k + \frac{1}{2}) \Delta T) \right] \quad (4.14)$$

in which $\Delta f = (f_1 - f_0)$ represents the difference between the frequencies of the PMD modulation signal and the optical signal for $\Delta f \ll f_0$. We see from the expression that the output is superimposed with an sinusoidal function that has the frequency $\Delta f = (f_1 - f_0)$. Its amplitude is modulated by a *si*-function, the frequency of which is determined by the product of the frequency Δf and the integration period ΔT .

Simulated result of the PMD is illustrated in **Fig. 4.18**, where the modulation frequency f_0 is set by 1MHz and the integration time by 100 μ s, as the disturbing signal f_i changes from DC to $2f_0$. We see that although the influence of the disturbance of low frequencies increases again at both outputs *A* and *B* of PMD, it is suppressed considerably at the differential output of the PMD. This effect of the PMD is the so called Correlated Balance Sampling (CBS). It works, in the frequency domain, similarly to a band-pass filter, which reduces the contributions of optical disturbance rapidly, as its frequency f_1 deviates from the modulation frequency of the PMD. It is obvious that the bandwidth is dependant on the integration period of PMD.

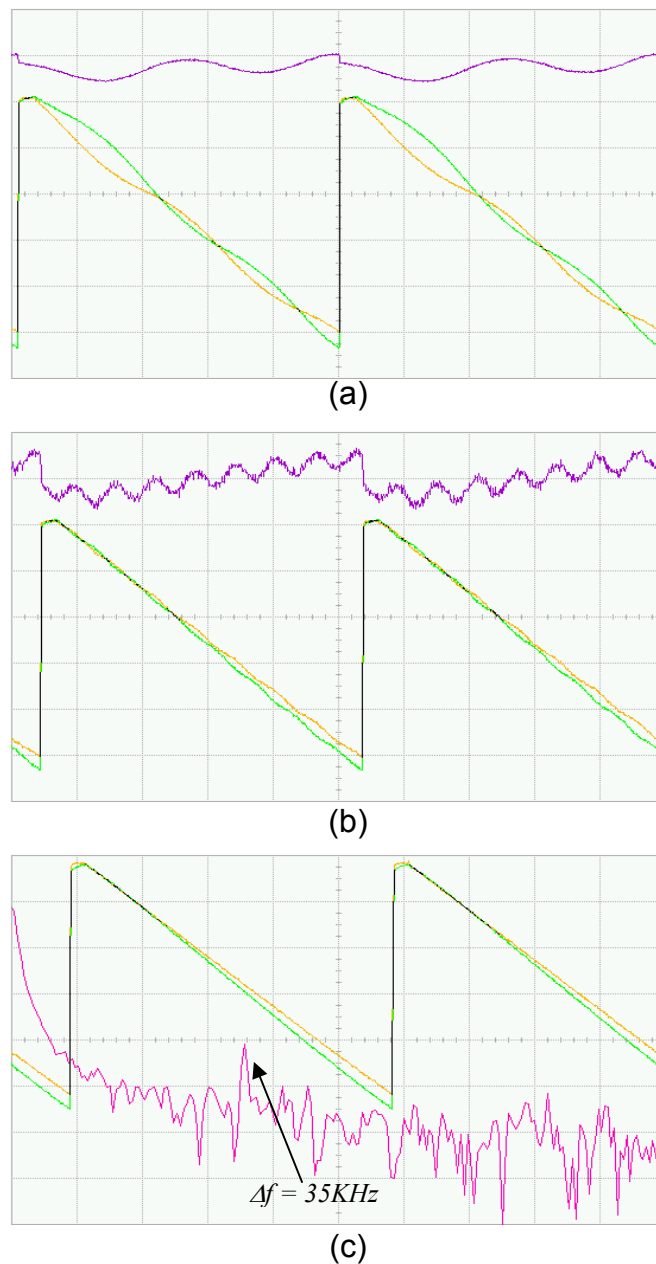


Fig. 4.19 The measured output signals of the PMD pixel. The PMD modulation frequency was set by $f_0=10\text{MHz}$, while the optical signal was modulated with different frequencies. (a) $\Delta f=2\text{KHz}$, (b) $\Delta f=8\text{KHz}$ and (c) $\Delta f=35\text{KHz}$. The integration period was fixed at 1ms. The square wave modulation was used.

In the measurement, the optical signal was modulated with different frequencies while the demodulation frequency of PMD was set by 10 MHz. **Fig. 4.19** shows both the output signals and the corresponding differential output of the PMD test pixel by setting the differential frequency Δf of the modulated optical signals at 2KHz, 8KHz and 35KHz

respectively. We see that the output signals of PMD is now modulated with a sinewave of the beat frequency Δf and its amplitude decreases rapidly with the increasing difference between the frequencies of the optical signal and the PMD modulation signals. Since the output of PMD is normally sampled at the end of the integration time after each PMD reset, so the integration period ΔT represents also the sampling period. It is obvious that the aliasing will be induced for $\Delta f > 1/2\Delta T$ at the outputs of PMD due to the Nyquist theory.

The measured results, normalized on the maximum amplitude obtained at $f_0=f_i$, are listed in the table 4.1. As one can see from the results, the superimposed voltage swing reduces rapidly with the increasing difference between both frequencies of the sending and receiving channels. Since the ranging systems with PMD operates usually in a frequency range of some tens MHz or higher, the CBS effect of the PMD can considerably suppress the disturbances of low frequencies.

Table 4.1 The normalized voltage swing of the PMD outputs according to the difference of both modulation frequencies. The measurement is based on the PMD test structure STP-17.5-2F-No.1.2-Z3.

PMD modulation frequency $f_0=10\text{MHz}$. Square wave modulation.								
PMD-test pixel: STP-17.5-2F-No.1.2-Z3								
Δf [KHz]	1	2	4	6	8	10	12	14
Amplitude [dB]	-7	-13	-21	-29	-30	-33	-38	-44

Both simulation and measurement results have demonstrated the excellent performance of PMD against the optical disturbing signals due to the correlated balance sampling property of PMD. On the other hand, this effect could also be used for the measurement of distance information. The typical method is the frequency shifting modulation (homodyne method) [Xu-1], in which the optical signal is modulated with different frequencies in a step of Δf . Through careful selections of Δf and ΔT , the depth information can be evaluated by using the corresponding algorithm similar to the phase shifting method. The relation between the correlation output and the time delay t_d of the reflected optical signal is given [Xu-1] by

$$I = \Gamma \left\{ 1 + \sum_{n=1}^{\infty} M_n \frac{\sin(\pi \Delta f \Delta T)}{\pi \Delta f \Delta T} \cos(2\pi n \Delta f (k + \frac{1}{2}) \Delta T + 2\pi n t_d + \vartheta_n) \right\} \quad (4.15)$$

As mentioned above, for the CW modulation, if the integration period is short enough, i.e. $\Delta T < 1/2\Delta f$, the sampled output of PMD gives the complete reconstruction of the differential signal described by equation (4.15). **Fig. 4.20** shows the measured result of a 1D-PMD demonstrator by setting the optical signal a frequency shift of 5Hz from the PMD modulation signal. Based on this principle, the velocity of the moving target can be measured. Assuming both light source and PMD are CW-modulated with the same frequency, the doppler-frequency of the moving object corresponds to the beat frequency detected at the PMD outputs which can be further evaluated based on the sample data [Rin-2].

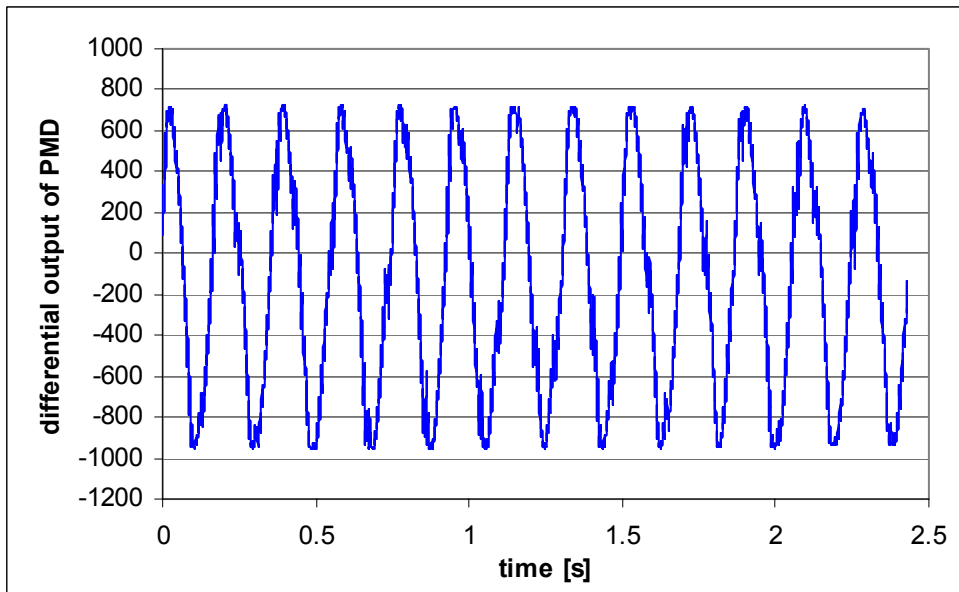


Fig. 4.20 The differential output of a PMD demonstrator. The integration of PMD was set by 900 μ s. The modulation frequency of PMD was 20 MHz and the difference between frequency of the optical channel and that of PMD was set 5Hz through the DDS phase shifting module. The measured signal frequency at the PMD output was 5.19 Hz.

5 3D-Imaging cameras based on PMD

In the previous chapters, we have discussed the PMD operation principle and presented the characterization measurements of the PMD pixels. With this knowledge, we introduce now in this chapter the time of flight PMD ranging systems based on the actually fabricated CMOS-PMD samples.

It is the unique electro-optical correlation property of the PMD device and the easy integration of the PMD pixels into a PMD line or array to make the modular design of smart 3D ranging systems possible. As one can see, the most functional modules used for 1D PMD ranging sensor can be used for the 2D or 3D PMD ranging cameras without any modification. This feature of PMD can reduce considerably the cost of system designs, which is very important for the product development. In the following sections we give first a rough description of the system architecture of PMD ranging cameras and then demonstrate the respective function modules of the ranging systems based on the PMD device. And finally the results of some typical range measurements of the realized PMD sensors will be presented.

5.1 System architecture of the PMD ranging cameras

The PMD time-of-flight ranging cameras using the phase shifting modulation technique in principle consist of following basic function modules:

- Optical modulation unit
- PMD front end module
- Phase shifting unit
- Timing control and data processing module

Fig. 5.1 shows the block diagram of the PMD TOF ranging system. The phase shifting module (DDS) generates the signals of modulating the optical light source and the push-pull signals for the PMD chip. The phase shifting between both signals, which are controlled by CPU through the control interface, can be performed either in the optical modulation channel or at the PMD side. The microprocessor and corresponding periphery supply the required timing pattern for the PMD and perform the digitizing of

PMD analog output for further processing. The special software performs the synchronization of phase shifting and PMD readout timing, the implementation of the multi-phase evaluation algorithm and the output of the obtained target depth information for display.

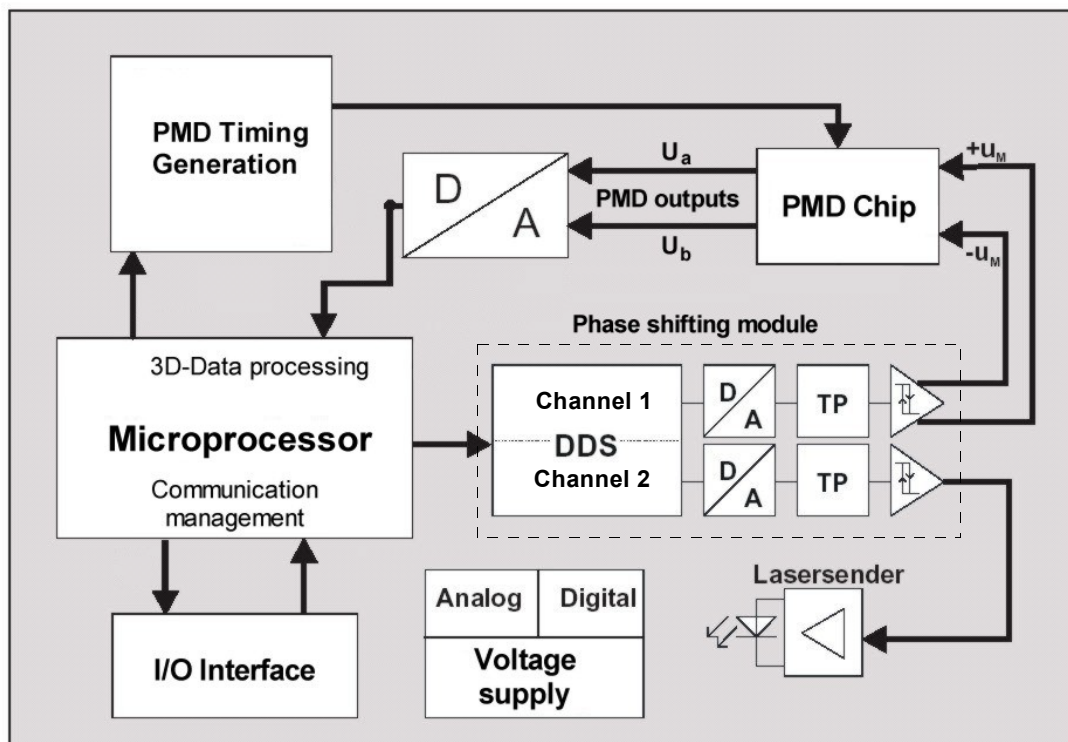
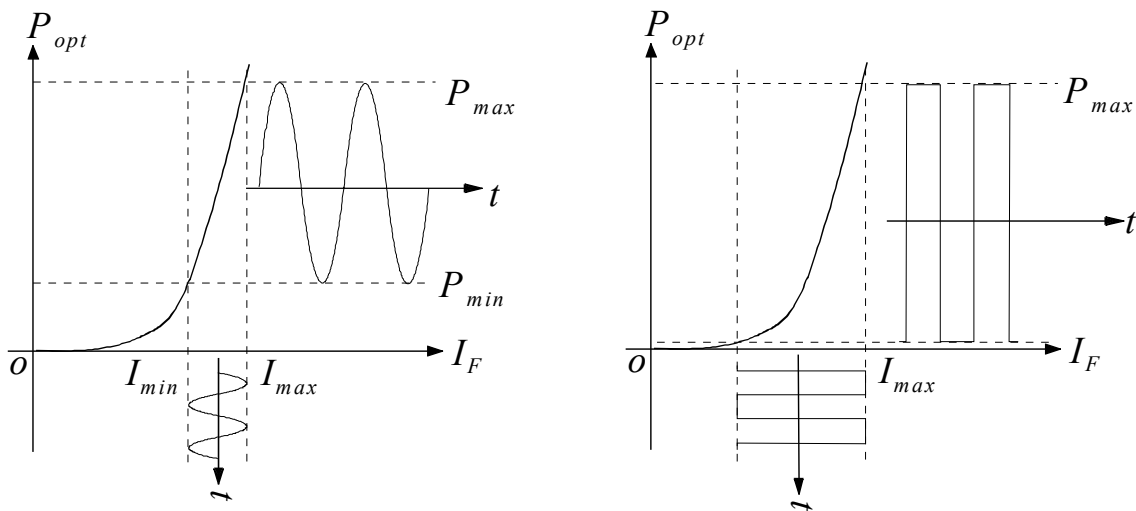


Fig. 5.1 Block diagram of a 3D PMD TOF ranging system using DDS as phase shifting module.

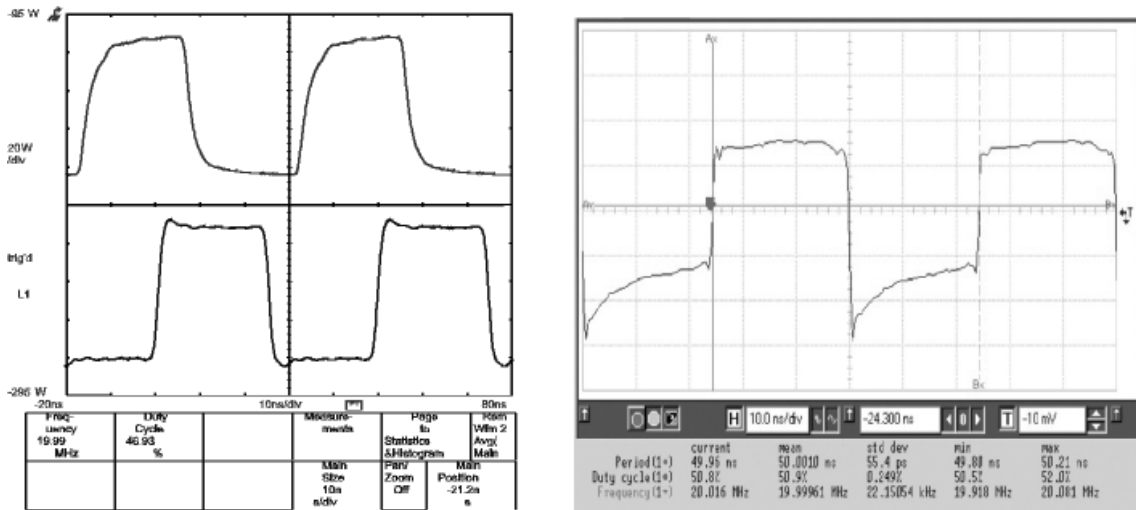
5.1.1 Optical modulation unit

The optical modulation unit generates the optical modulation signal for the illumination of the target scene. It consists of the modulated light source and the corresponding driving circuit. As the light sources of PMD ranging sensors, the laser diode (Toshiba TOLD 9441MC) as well as LEDs (Fietje FQO5502) is used. The laser diode has a center wavelength of $\lambda = 658$ nm with a spectral bandwidth of about 35 nm. The optical power of the laser diode is limited by 1mW, due to the eye safety condition. In comparison, the light source using LEDs has no such problems, so for most 3D-scene illumination applications, where much more optical power is required in order to get enough optical reflection intensity, LEDs are usually used as the light source. The most

applied modulation signal forms for the CW-modulation are sinusoidal or square waves. Compared to the sinewave modulation, the squarewave modulation is not only easy to implement in the practice, but the maximum optical modulation depth of nearly 100% can also be obtained, as shown in **Fig. 5.2a**. Therefore, the optical square wave modulation was used in our applications. **Fig. 5.2b** shows the measured optical modulation signals of the optical module using laser diode and LEDs mentioned above, respectively, at the modulation frequency of $f_{mod} = 20\text{MHz}$.



(a)



(b)

Fig. 5.2 (a) Ideal optical intensity modulation characteristic of LED or laser diode by using sinusoidal or square wave signal. (b) The measured optical outputs of the laser module and LED with squarewave modulation at $f_{mod} = 20\text{MHz}$.

5.1.2 PMD front end module

The main part of PMD front end module is of course the PMD chip itself. Since the PMD performs the optical mixing and integration with its on-chip readout and driving circuit the analog low frequency output signals of PMD can be directly digitized for further processing, so it doesn't need very complicated periphery as usually required in traditional time-of-flight ranging systems. The main task of the PMD front end circuit is the modulation signal level conversions to ensure the optimal operation condition of PMD. The digital control signals from the timing module are connected directly to the PMD. Special attention to the layout design of the front end circuit should be paid to achieve the required low noise performance. Digital switching and power supply noises must be limited from coupling with the analog signal and HF-signals. **Fig. 5.3** shows a realized PMD front end module used for PMD ranging sensors.

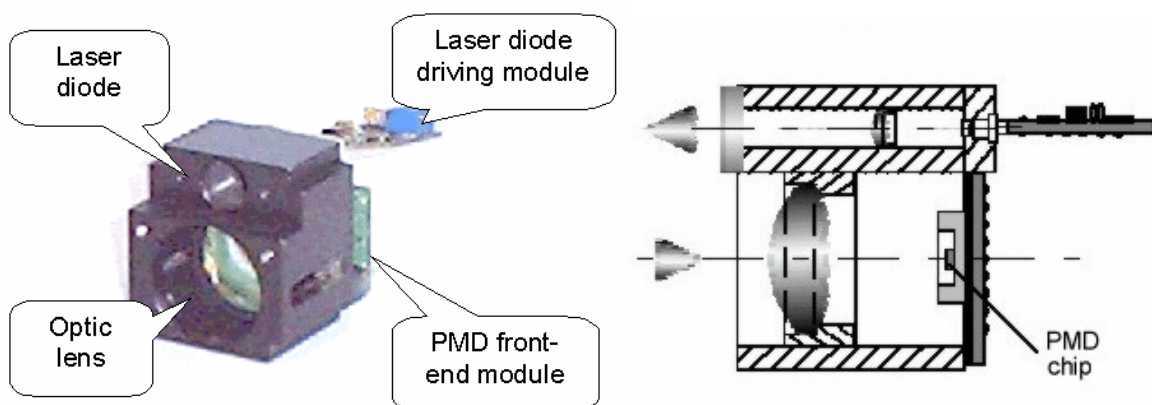


Fig. 5.3 The PMD front end module which is used for 1D and 2D PMD ranging sensors

5.1.3 Phase shifting unit

For the TOF ranging systems with phase-shifting technique, the phase shifting module plays a key role in the system. It supplies not only a signal base of highly precision but also the modulation signals both for the light source and PMDs with very flexible, exact phase shift possibilities. Two concepts of generating phase shifting signals are

implemented in our PMD ranging camera systems: phase-shifting module based on the direct digital synthesizer (DDS) technique and fixed 4/8 phase-shifting module using digital shift registers. With the DDS phase shifting module one can not only construct the PMD ranging system with phase shifting technique but also with frequency shifting or chirping technique [Xu-1], or with DLL technique [Bux-2] due to the variety of different modulation possibilities. Compared to DDS, the fixed phase shifting circuit generates the discrete phase shifts digitally. It can be easily planted to the same chip in the future like other peripheral circuits such as addressing and readout circuits, due to its simple structure. In the next sections we will give more detailed discussion about the realization of phase shifting technique.

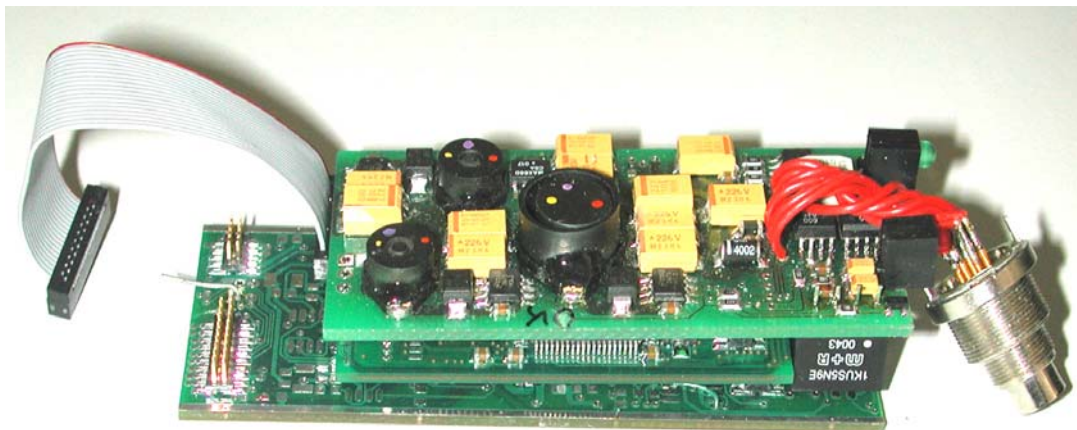


Fig. 5.4 The control and processing board for the PMD ranging sensor.

5.1.4 Timing control and data processing module

Because of the on-chip implementation of the peripheral circuitry of PMD, similar to CCD and CMOS image sensing chips, the timing control of PMD is drastically simplified. For the PMD sensing line as well as arrays, compared to the single PMD pixel, only some additional digital control signals for addressing and readout of PMD analog signals are required. This feature allows us to use the same control and processing module for configuration of different types of PMD ranging sensors. In the current realization, an 16bit RISC microprocessor module based on Siemens C164-CPU overtakes this role. The on-chip integrated periphery of C164 microprocessor, based on

FPGA technique, – the programmable CAPCOM units – allows an easy, flexible generation of required timing pattern without any additional hardware, which works parallel with the CPU after the programming of the corresponding control registers. The developed software synchronizes the PMD integration time, readout frame and the phase shifting of the modulation signals. Based on the implemented processing algorithm, the distance information detected by each PMD pixel will be evaluated.

5.2 Optical aspect of illumination

Since the PMD sensor is based on the time-of-flight principle, the active illumination of the scene is necessary. It is important to have the knowledge of the relation between the optical power of the modulated light source and the optical power collected at each pixel in the PMD sensing array. As illustrated in **Fig. 5.5**, the illumination concepts of the target scene are very different according to the applied light sources (Laser or LED) and the size of the PMD sensing array (one point, line or array). For light sources using laser diode, holographic optical lens (HOE) can be implemented, while the illumination is usually achieved directly through the LED array for LED light source. With the assumption of homogeneous illumination of the target scene and Lambert reflection of the target surface, the optical power of the pixel is given by

$$P_{pixel} = \frac{A_{pixel}}{A_{image}} \cdot \frac{P_{opt} \cdot \rho \cdot G_{lens} \cdot D_r^2}{4R^2} \quad (5.1)$$

- with
- A_{pixel} active optical area of the pixel
 - A_{sensor} total sensing area of the PMD line or array
 - P_{opt} optical power of the light source
 - ρ reflectivity of the target
 - G_{lens} damping factor of the lens system
 - D_r aperture of the lens
 - R distance of the target

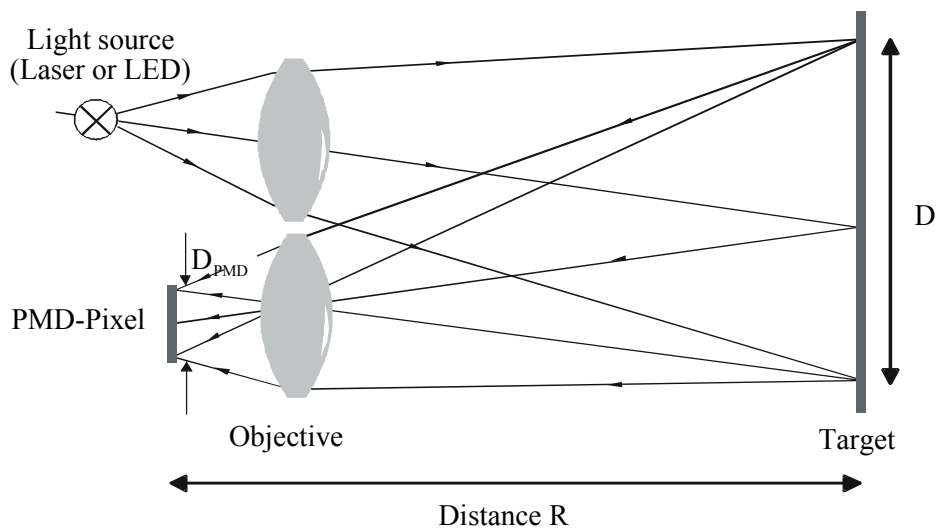


Fig. 5.5 Optical configuration of a PMD ranging camera

One can see from the above relation that receiving optical power is reverse proportional to the square of the distance to target, as illustrated in **Fig. 5.6a**. The intensity distribution of the back-scattered light doesn't depend on the illumination angle in the case of Lambert reflection. The reflected intensity decreases with cosine of the observation angle with respect to the surface normal. For some object surfaces such as Retro-reflectors in traffic signs the equivalent reflection coefficient in certain reflection direction can be much larger than 1 ($\rho = 1$ for a white sheet of paper) and the intensity distribution is dependent of the illumination angle (see **Fig. 5.6b**).

The typical reflection coefficient for Lambert reflectors has the values between zero and one (white paper). The reflectivity of some typical diffusely reflecting materials at a wavelength of 658nm is listed as following:

White paper	up to 100%
Gray paper	32%
Brown paper	27%
Black paper	3%

All the data are normalized in percent referred to the reflectivity of the white paper.

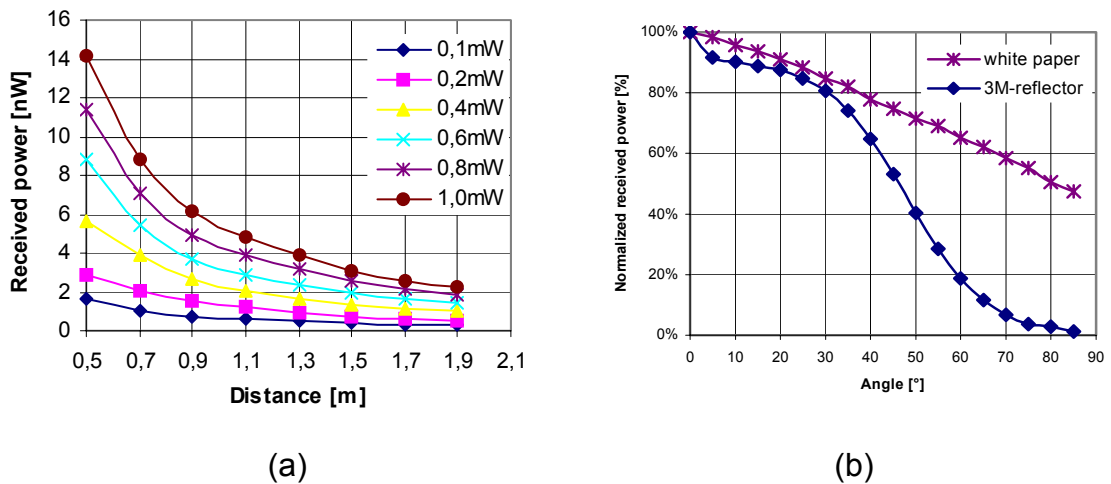


Fig. 5.6 (a) Received optical power versus the target distance in case of Lambert reflection. (b) Optical intensity dependent of the observation angle for white paper and Retro-reflectors. Sender objective: $f = 30mm$, $D = 30mm$; sensing objective: $f = 21mm$, $D = 20mm$; light source: $\lambda = 890nm$.

5.3 Phase shift technique

5.3.1 DDS

Direct digital synthesis (DDS) is a technique for using digital data processing blocks as a means to generate a frequency- and phase-tunable output signal referenced to a fixed-frequency precision clock source. It can be practically defined as a means of generating highly accurate and harmonically pure digital representation of signals, which is then reconstructed with a high-speed digital to analog converter (DAC) to provide an analog output signal, typically sinusoidal waves. Although limited by Nyquist criteria (up to $\frac{1}{2}$ the frequency of the applied clock reference), the order of milli-hertz or even nano-hertz of the phase resolution control can be obtained.

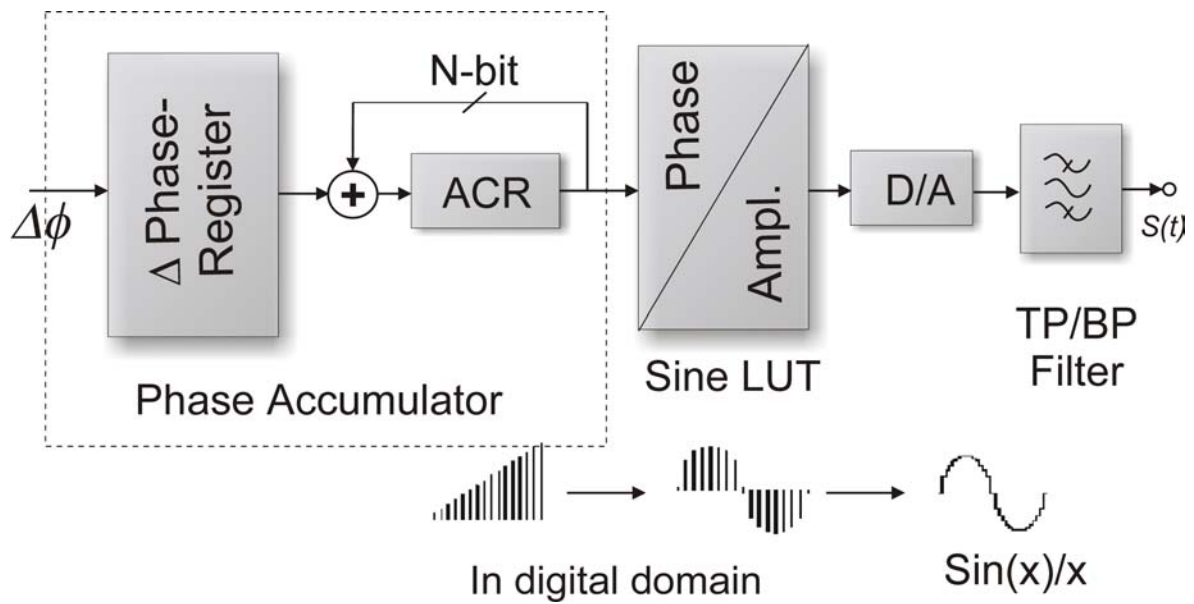


Fig. 5.7 The principle of signal flow through the DDS architecture.

The pure digital processing feature of the DDS device allows the very easy and flexible software configuration of the DDS functionality. The most operation functions of the DDS can be listed as following:

- Phase modulation
- Binary frequency shift keying modulation (BFSK)
- Frequency hopping
- Frequency chirping

As mentioned before, of interest is the phase modulation mode of DDS in the PMD ranging applications. The phase modulation of DDS can be realized either through internal phase modulation that provides extremely fine phase resolution (up to 2^{32} – state phase resolution for the applied DDS module) and external phase modulation where extreme phase modulation of fixed phase shift can be implemented through the corresponding control port.

- **operation principle of DDS**

As illustrated in **Fig. 5.7**, a DDS device consists of register bank, phase accumulator (PAC), the sinewave look-up-table (LUT), digital to analog device (DAC) and low/band-pass filter. The parameters such as phase shifting step or output frequency can be dynamically control by using the corresponding register-bank through the I/O -interface. The phase accumulator is the core of a highly – flexible DDS device in which a delta phase register, an N-bit variable-modulus counter and an accumulator register are implemented. The resulting continuously incremented phase values are used for accessing the contents (the equivalent sine amplitude words) stored in the LUT. A high-speed D/A-converter generates then analog sine waveform in response to the digital input words from the LUT.

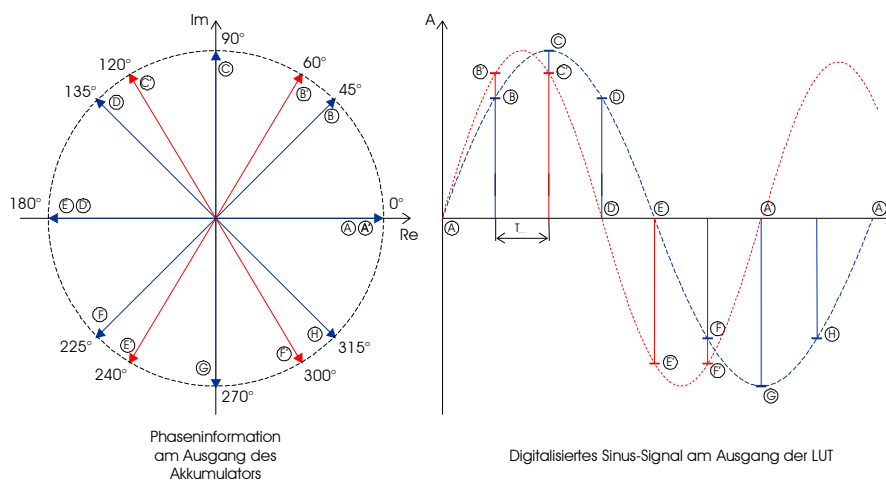


Fig. 5.8 Principle of digital sine wave generation. The phase accumulator of DDS functions as a digital phase wheel.

- **Phase and frequency resolution of DDS**

The phase accumulator in the DDS architecture can be understood as a digital “phase wheel” that visualizes the sinewave oscillation as a vector rotating around a phase circle, as depicted in **Fig. 5.8**. Each designated point on the phase wheel corresponds to the equivalent point on a cycle of a sine wave form. One revolution of the vector around the phase wheel, at a constant speed, i.e. the frequency of the reference clock f_{CLK} , results in one complete cycle of the output sinewave. The phase accumulator is

utilized to provide the equivalent of the vector's linear rotation around the phase wheel. The contents of the phase accumulator correspond to the points on the cycle of the output sinewave.

The content in the delta phase register forms the phase step size between reference clock updates. For a given phase step size $\Delta\phi_T$, the output of the phase accumulator is presented by

$$\phi_T(k) = \text{mod} \left[\sum_{i=1}^k \Delta\phi_T \cdot (k-i), 2\pi \right] \quad (5.1)$$

with $k = 1, 2, 3, \dots, \infty$. Since the number of discrete phase points contained in the "phase wheel", which corresponds to a complete period of the sinewave 2π , is determined by the word length, N , of the phase register, so the phase step size can be defined as

$$\Delta\phi_T = \frac{2\pi}{2^N} \cdot M \quad (5.2)$$

where $M = 1, 2, 3, \dots, 2^N$ represents the binary content of the delta phase register. It is obvious that the phase resolution of the DDS is

$$\Delta\phi_T = 2\pi / 2^N \quad (5.3)$$

For a DDS device with 32bit phase accumulator, the phase resolution corresponds 8.38×10^{-8} grad.

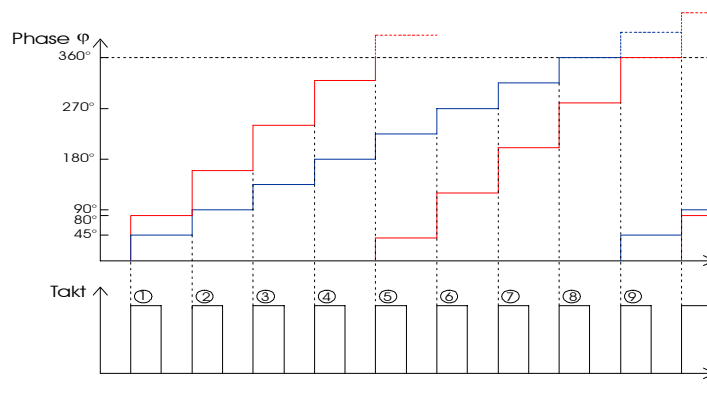


Fig. 5.9 The principle of continuous phase generation of the PAC based on the reference clock.

The relationship of the output frequency and the reference frequency form the basic tuning equation for DDS architecture:

$$f_s = \frac{\Delta\phi_T}{2^N} \cdot f_{CLK} = \frac{M}{2^N} \cdot f_{CLK} \quad (5.4)$$

Similarly, we have the frequency resolution of the DDS, letting $M = 1$,

$$\Delta f_{s,\min} = f_{CLK} / 2^N \quad (5.5)$$

with the consideration of the Nyquist theory which must also be obeyed in this case, the maximum frequency of the output DDS signal is $f_{s,\max} = f_{CLK} / 2$. Taking the DDS module in our application as example, for $f_{CLK} = 65\text{MHz}$ and $N = 32$, the frequency resolution is 0.015Hz and the maximum frequency can be set up to ca. 32MHz . Equation (5.4) gives the definition of the frequency modulation. As demonstrated in the **Fig. 5.8** and **Fig. 5.9**, the changes of the values of M in the DDS architecture result in immediate and phase-continuous changes in the output frequency, so M is also called the frequency tuning word. The phase modulation is simply realized by an addition of the initial phase value ϕ_0 to the phase accumulator register which causes an immediate phase jump in the output signal of the DDS device, with the same phase resolution of the delta phase register defined in equation (5.3).

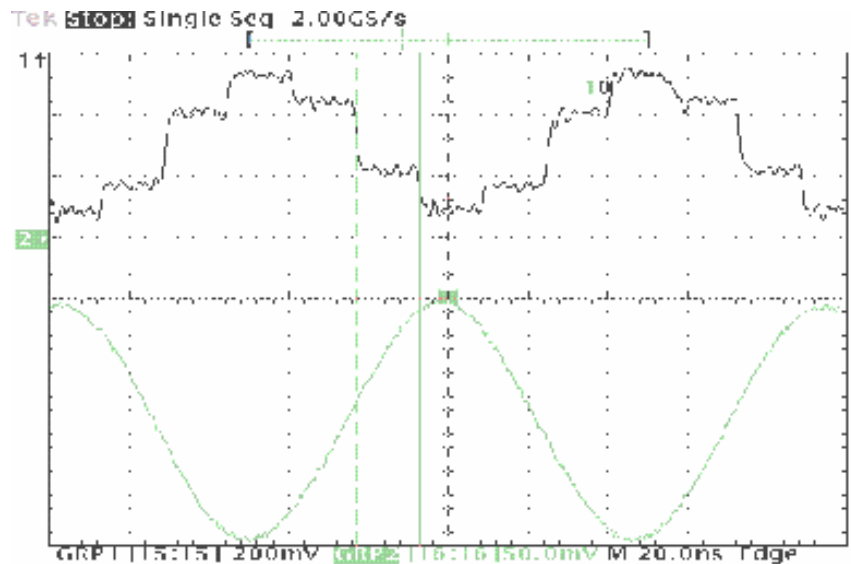


Fig. 5.10 The output signal of DAC and the final output of the sinewave after the filter.

- **Performance of DDS device**

The linear changed phase from the accumulator output of DDS, with a modulus 2π , is converted by the following phase-to-amplitude lookup table into the sinewave amplitude information that is presented to the D/A converter, and the pure harmonic wave is filtered out through the corresponding low-pass or band-pass filter (see **Fig. 5.10**). Most DDS architectures exploit the symmetrical nature of a sinewave and utilize mapping logic to synthesize a complete sinewave cycle from $\frac{1}{4}$ cycle of data from the phase accumulator. The phase-to-amplitude lookup table generates all the necessary data by reading forward then back through the lookup table.

The performance of the DDS is mainly dependent the factors such as the phase noise of the system clock, phase truncation of the LUT and amplitude truncation of DAC. The non-linearity and glitch energy of DAC affect also the spectral purity of the output signals of the DDS.

The reference clock input to the DDS system is the major contributor to the phase noise of the system, even though its effect is reduced by the frequency division process of the DDS. The frequency accuracy of the clock is propagated through the DDS system. The phase noise of the DDS output will show an improvement over phase noise of the clock source itself of $20 \cdot \log(f_{CLK} / f_s)$, where f_{CLK} and f_s are the system clock frequency and the output signal frequency.

The amplitude quantization occurs in the digitizing the sine wave. Since an ideal representation of sinewave requires an infinite number of bits for most values, which is in practice not possible for the DACs, the value must be truncated. The error caused by the amplitude quantization is called the quantization distortion. For a high-speed DACs of N-bit resolution, the broadband signal-to-spurious ratio is given by

$$SNR = 6.02 \cdot N + 1.76 \text{ (dB)} \quad (5.7)$$

The phase truncation of DDS is due to the physical size limitation in the realization of LUT. For a DDS system with a 32-bit phase accumulator, to directly convert 32 bits of

phase to corresponding amplitude would require 2^{32} entries in a lookup table. Even with 8-bit accuracy, this would require 4-gigabytes of lookup table memory, which would be impractical to implement such a design. The solution is the phase truncation, where only a portion (N bits) of the Most Significant Bits (MSB) is used to addressing the sine lookup table. The truncation of the Least Significant Bits (LSB) means loss of the phase information and contributes phase errors. Obviously, the phase errors introduced by truncating the accumulator will result in errors in amplitude during the phase-to-amplitude conversion process in the DDS. Similarly to the effect of amplitude truncation, the maximum SNR turns out to be very closely approximated by $6.02 \cdot N$ decibels. So, a 32-bit DDS with a lookup table of 12-bit word length will yield phase truncation spurs of no more than -72dBc regardless of the output frequency chosen.

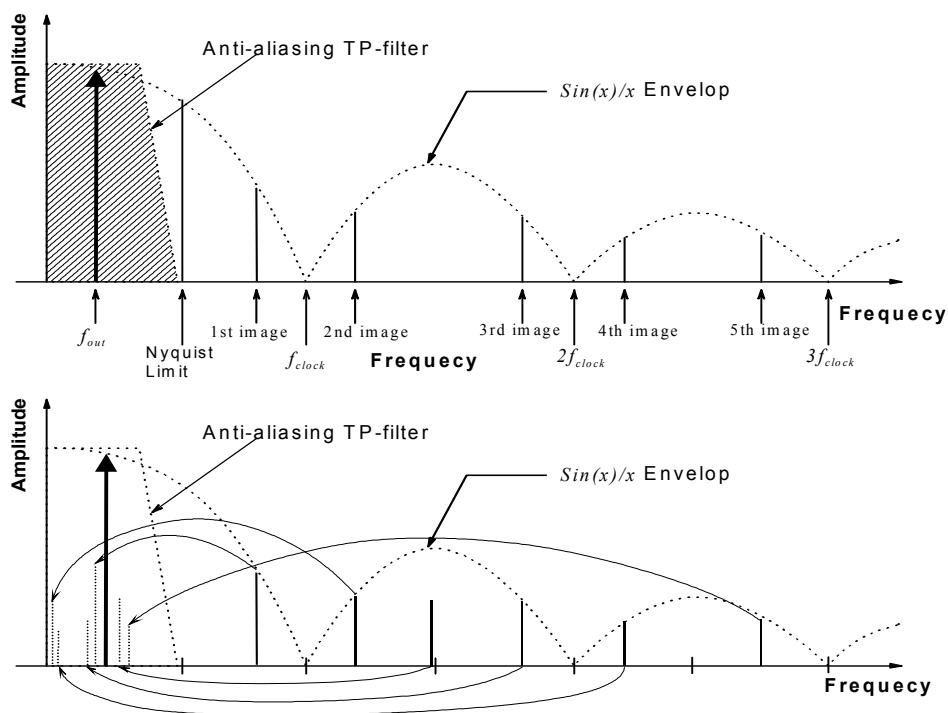


Fig. 5.11 Aliasing effect due to the quantization distortions and phase truncation of the DDS system.

The quantization effect introduces a number of high frequency components superimposed on the fundamental. In the frequency domain, the distortion errors are aliased within the Nyquist band and appear as discrete spurs in the DAC output spectrum, as graphically depicted in **Fig. 5.11**. To precisely analyze the distribution of

phase truncation spurs is quite complicated. A detailed analysis may be found in [NiSa]. The frequencies of the discrete spurs and the amplitude of each depend on the ratio of the system clock frequency f_{CLK} to the generated output signal frequency f_s , as well as the phase relationship of the output waveform to the system clock. The discrete aliased images due to the sample rate aliasing appears at the frequencies of

$$f_{sp} = n \cdot f_{CLK} \pm |f_{CLK} - f_s| \quad n = 0, 2, 3, \dots, \infty \quad (5.8)$$

Careful selections of the clock frequency can eliminate n^{th} order aliased images if $f_{CLK} > (n+1)f_{max}$, where f_{max} is the upper edge of the interested passband. Nevertheless, complete elimination of the alias frequencies of the fundamental is not impractical. Hence, the output section of the DDS is usually followed by a low-pass “anti-aliasing” filter for suppressing the discrete spurs to acceptable levels.

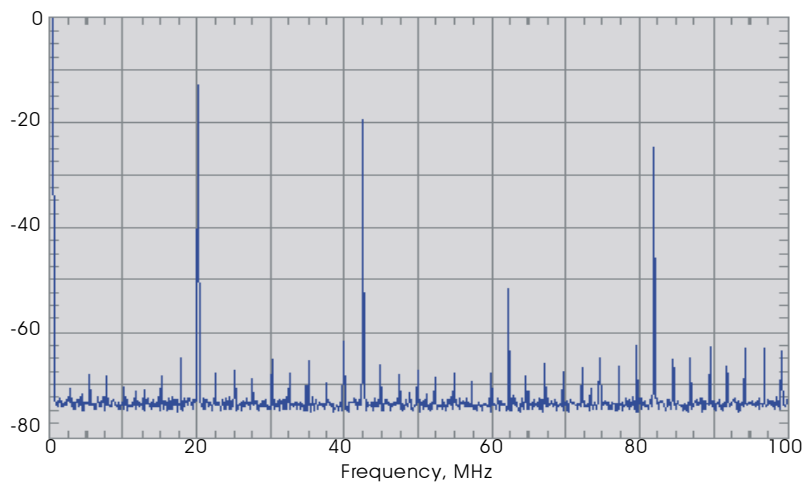


Fig. 5.12 Spectral measurement of DDS output signal by setting the generated frequency at 20MHz.

- **Measurement of DDS phase shifting module**

The implemented phase-shifting module based on the DDS device uses the Qualcomm Q2368 dual direct digital synthesizer with extern 12 Bit DACs (HI5731), followed by the anti-aliasing low-pass filter (SCLF-21.4). The Q2368, driven by a system clock of 62.5MHz, works in the dual modus that allows continuous frequency tuning from 0 Hz until 31.25 MHz and phase modulation over the complete 2π period with very precise steps on both output channels, independent of each other. The measurement was performed by setting the generated frequency of the DDS output signals at $f_s = 20$ MHz,

as the frequency used in the PMD ranging system. **Fig. 5.12** shows the measured wide-band spectral performance of the DDS output signal. As mentioned before, we see from the results really the discrete spurs produced due to the sampling rate aliasing at frequencies 42.5MHz and 82.5MHz.

Fig. 5.13 demonstrates the spurious performance of the DDS output spectrum over a narrow band of 10KHz centered on the DDS output frequency. In addition to the fundamental, there are a number of high order harmonic components in the near. Two factors affect mainly the narrowband spurious performance of DDS output: the high order harmonics of the clock source caused by the timing jitter. This is because that the system clock signal is also the DAC's sample clock. This causes the DAC output signal to be modulated by the clock signal. The result is spurs that are symmetric about the frequency of the DDS output signal. Another factor is associated with the phase truncation effect of DDS, as discussed previously. Compared to the phase truncation distortion, the influence the clock timing jitter on the narrowband spurious performance of DDS output signal is much more significant.

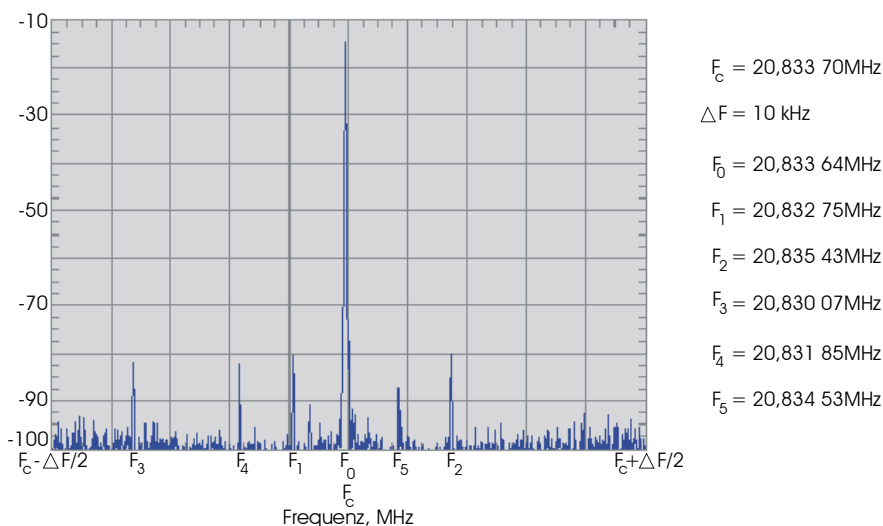


Fig. 5.13 The narrowband spurious performance of the DDS output signal.

In order to improve the output performance of the DDS, the anti-aliasing low-pass filter is implemented direct after the DAC. As shown in **Fig. 5.14**, the frequency sweep of the filter shows the approximately -60dB stopband begins only 25 MHz beyond the cutoff frequency approximately 24.5 MHz passband. The spectrum of the DDS output signal

after the low-pass filter is illustrated in **Fig. 5.15**, where the frequency of the sinewave generated is 20 MHz. One can certainly see that the most alias images of the 20 MHz generated DDS output out of the pass-band in the stop-band are significantly filtered out. The SFDR (spurious-free dynamic range) performance of the DDS is improved to -76 dB. It is obvious that the aliasing and harmonic components near the fundamental can not be eliminated. For further improvement of the DDS output performance the band-pass filter should be used. For the in this work discussed application where the sinusoid is converted into the square wave, more critical is the timing jitter and the phase noise performance of the output signal, since this will further affect the distance evaluation accuracy of the PMD ranging cameras. We will give more detailed discussion in the later sections.

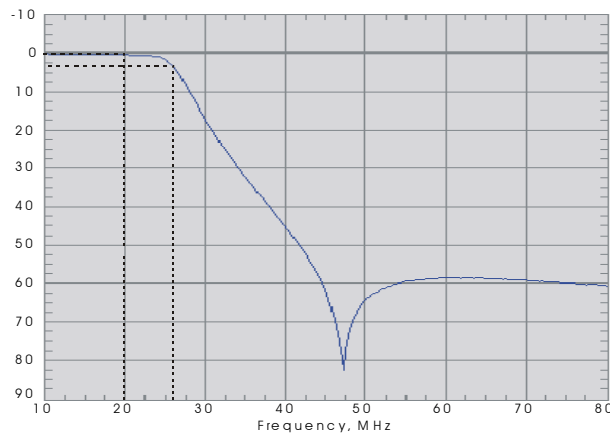


Fig. 5.14 Frequency response of the anti-aliasing low-pass filter SCLF-21.4

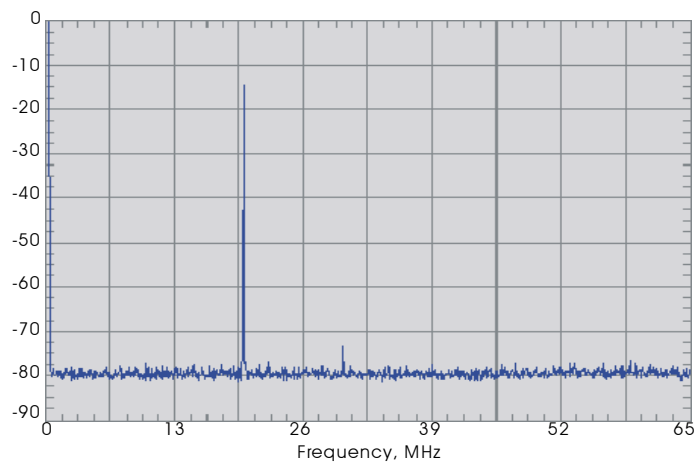


Fig. 5.15 Spectrum of the generated sinewave of the DDS filtered by the anti-aliasing low-pass filter.

5.3.2 Fixed phase shifting generation

The DDS technique provides a wide range of modulation functions with extremely high operation precision. For the TOF ranging systems using square wave phase shifting modulation technique, however, additional conversion of the sinewave of the DDS output to square wave signals should be implemented. Another technique of directly generating the square wave modulation signals with fixed phase shifting is based on the pure digital technique. **Fig. 5.16** shows the block diagram of the phase shifting module. A high precision clock source provides the driving clocks for both shift register banks which output eight parallel square wave signals with eight different phase delays. One register bank is positive flank by the clock signal, the other negative flank triggered. All eight signals are then input to the corresponding multiplexer. According to the control code from the I/O interface, one of the eight signals with corresponding phase delay is selected for output, which is, together with signal of the reference channel, at end clocked out by the system clock.

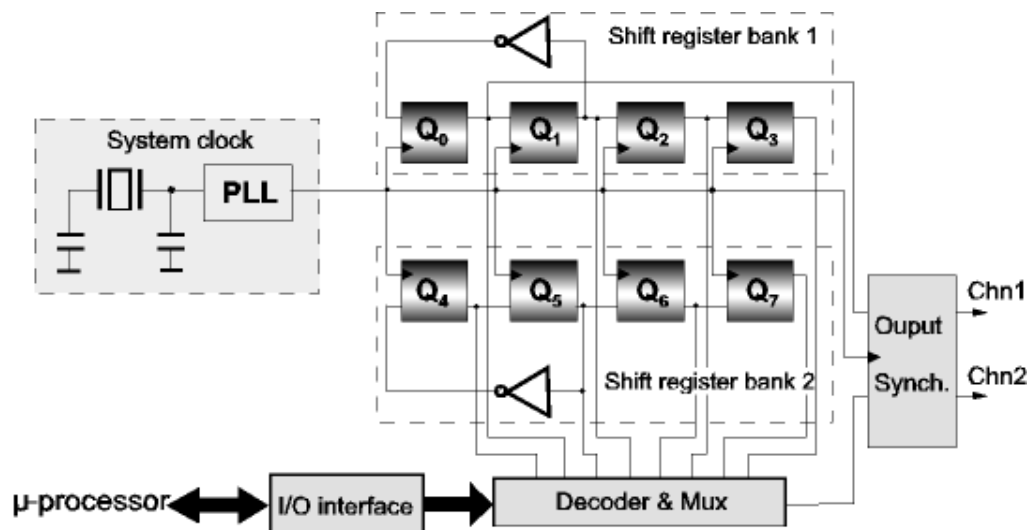


Fig. 5.16 Block diagram of the fixed 8 phase shifting (CPLD) module.

It is obvious that the module provides directly the digital square wave signals, one as reference signal and the other the shifted signals. For the 8-step phase shifting module described in **Fig. 5.16**, the frequency of the output square wave is defined by $f_s = f_{CLK} / 4$, where f_{CLK} is the system clock frequency. The 8 phase shifts are then 0° ,

45°, 90°, ..., 315°. Since both synchronized output signals are derived from the system clock itself, their phase noise performance depends mostly on the spectral purity of the system clock source. **Fig. 5.17** shows the measured the output signals and the swept frequency plotting of one output signals. This module is currently realized on a fast CPLD-chip, driven by a 65-MHz system clock source.

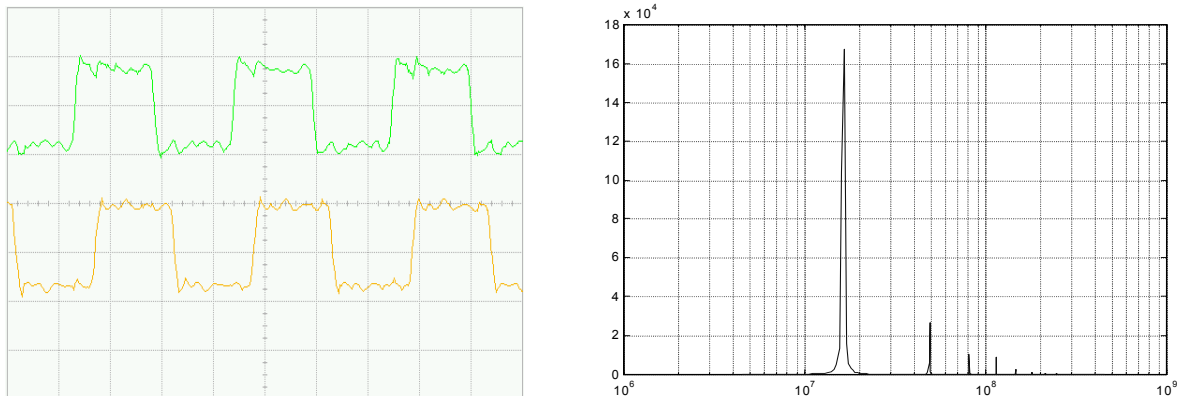


Fig. 5.17 (a) The output signals with 45° phase shift and (b) the spectrum of the square wave output. The system clock frequency is 65MHz. With 8 – step phase shifting.

5.3.3 Phase jitter consideration

For the PMD ranging cameras described in this work, the spectral purity of the output signals of the phase shifting module, which is ultimately caused by the phase jitter, is very important. This feature affects directly the distance accuracy of the evaluation. There are two primary factors that cause the phase jitter on the output signal. The phase jitter of the system clock causes feedthrough interference, since the synthesized sinewave, in the DDS module, is converted by DACs which is driven by the system clock, while in the second method the digital square wave outputs are synchronized by the system clock signal. Coupled noise, on the other hand, can be in the form of locally coupled noise caused by cross-talk and/or ground loops within or adjacent to the immediate area of the circuit. It can also be introduced from sources far removed from the circuit. Proper layout and fabrication techniques are the only insurance against these forms of phase jitter.

The measurements of both phase shifting modules are listed in the table 5.1. As one can see from the results, the output signals of both phase shifting modules have relatively the same order of phase jitter. Without consideration of other system noise sources in the PMD ranging cameras with 20MHz operation frequency, the maximum achievable distance accuracy using 8- phase-shifting method for a phase jitter of 23.4ps corresponds 1.23mm. As we see from the histogram of the phase jitter shown in **Fig. 5.18**, the phase noise of the output signals demonstrates a typical random process with normal distribution.

Table 5.1 the measured phase jitter of the output signals of the phase shifting modules

		DDS MODULE	CPLD MODULE
Output frequency		20 MHz	16.25MHz
Phase jitter	Chn 1	23.4 ps	31.9 ps
	Chn 2	25.9 ps	28.2 ps

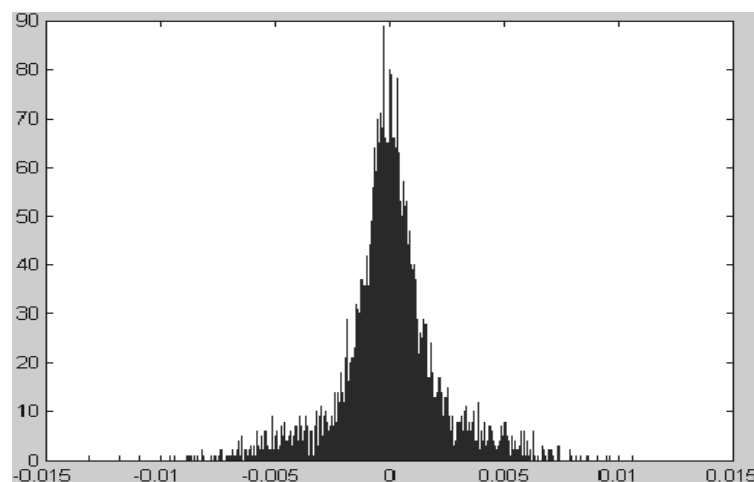


Fig. 5.18 The histogram of the phase noise measured at one output of phase shifting generation module.

5.3.4 Summary

We discussed in this section the realization of the generation of modulation signals and the corresponding phase shifting technique. DDS is nowadays a very sophisticated technique which has been widely used in different application areas such as the communication and radar techniques. The DDS module due to its high operation precision and a wide range of modulation functions can be used for the PMD ranging systems based on different modulation techniques such as phase/frequency-shifting modulation, frequency chirping and PN-sequence modulation [Xu-1]. Since the DACs and the corresponding anti-aliasing low/band-pass filter, as well as the comparators for square wave conversion in our application, must be used to convert the synthesized digital sinewave data into the required output signal, the introduction of the analog circuits makes the layout design of the module very difficult to reach the necessary SNR and the spectral purity of the output signals. Also the complicated architecture of the circuit is the main problem for the possible integration of the phase shifting module as on-chip periphery.

Compared to the DDS concept, the structure of the fixed multi-phase shifting generation concept is quite simple. Although it generates only limited pre-defined phase shifts, it satisfies the requirement of the PMD ranging systems using phase-shifting modulation technique which is most applied in 3D TOF ranging systems. This multi-phase shifting module can be easily integrated on-chip in the future due to its simple structure and the pure digital realization.

5.4 Data processing

As mentioned at the beginning of this chapter, the main part of the data processing module is a 16Bit RISC C164-microprocessor. **Fig. 5.19** shows the configuration of the CPU-processing board. It is the central unit of the PMD ranging system. From the view of the processing tasks it can be divided into the following main function blocks: DDS phase-shifting control, PMD readout timing, PMD analog output signal acquisition and distance information evaluation.

The C164 microprocessor operates at a system clock of 20MHz. Both the phase-shifting control and PMD readout logic are realized by using the CAPCOM units of the microprocessor, an on-chip integrated programmable FPGA periphery which can generate different timing and control pattern without any additional hardware. The register bank of the DDS module is directly mapped into the memory addressing space, so the CPU can either modify the phase and frequency setting by writing the corresponding control registers, or perform extreme fast phase shifting through the additional external phase shifting control interface. Once initiated and configured according to the parameters, the timing control unit runs almost standalone, without any interfering of CPU, generating the required PMD readout timing pattern. Clocked by an internal timer at 2.5MHz, up to 50 μ s PMD reset frame and maximum 1.25MHz readout clock frequency for the PMD line and PMD arrays can be achieved. The data acquisition from the PMD outputs is performed by an external 14 Bit ADC converter, in which both PMD output channels are simultaneously sampled at the end of PMD integration period.

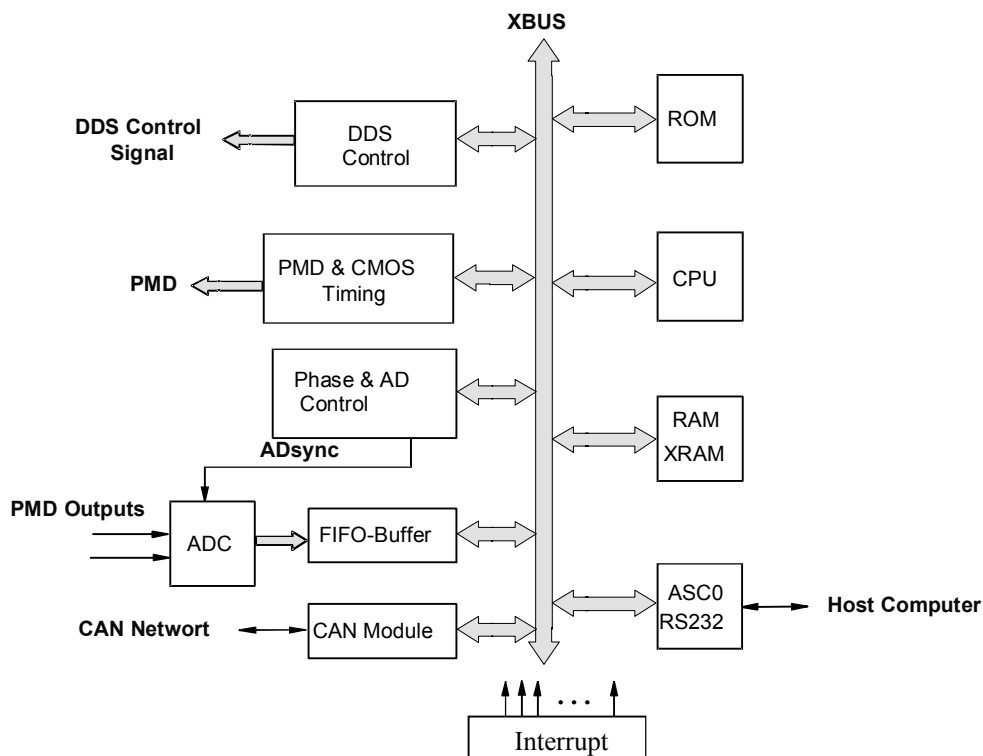


Fig. 5.19 Block diagram of the timing and data processing module of the PMD ranging cameras based on the C164 microprocessor.

Finally, the developed software of the microprocessor evaluates the required depth information of the target, depending on the digitized PMD data, by using the corresponding multi-phase shifts processing algorithm which has been discussed in the previous sections. As mentioned before, we concentrate mainly on the PMD ranging systems based on the phase shifting modulation technique.

5.4.1 Frame synchronization and data buffering

The main task of the module is, in addition to the implementation of the related distance evaluation algorithms, the synchronization of different processes that runs parallel with each other. The most critical and time consuming process for the CPU is the data acquisition of the PMD outputs at end of each integration frame. An PMD integration frame begins with the reset period of the PMD and the phase shifting of the modulation signal followed by the integration period. Since each frame is assigned to the corresponding phase shifts, any loss or false assignment of the digitized PMD information could leads to processing errors of the evaluation algorithm. To avoid any possible loss of data, the PMD digitizing and data acquisition is controlled by the PEC – interrupt routine that responses each sampling request at the end of integration period, suspends all other processes currently running in the CPU and starts immediately the PMD readout cycles, as illustrated in the **Fig. 5.20**.

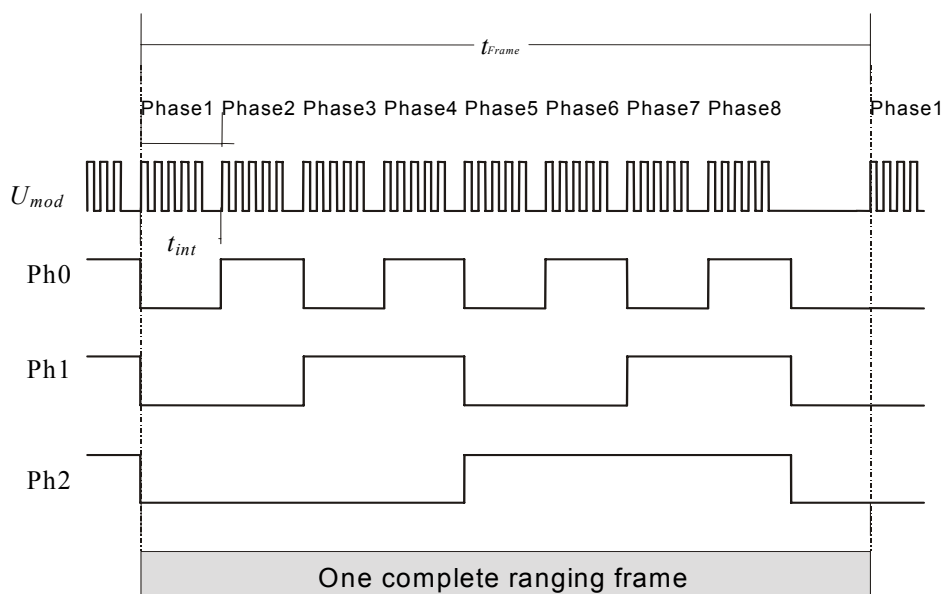


Fig. 5.20 The timing diagram of the data acquisition process of the PMD ranging sensor using phase shifting technique.

For the PMD ranging sensor working with phase shifting modulation technique, the total N phase shifts are divided regularly over a complete 2π modulation period, as discussed in chapter two. After the initiation, the CPU starts with PMD reset period followed by the corresponding PMD integration period. The first phase shifting of the modulation signals with predefined phase step is performed during the PMD reset. At the end of the integration the PMD readout timing is evoked. Clocked by the corresponding readout clock signal, both output channels of each PMD pixel are simultaneously sampled and transferred to the FIFO memory for further processing. The next frame begins then with the second phase shifting. This processing repeats N times until all N phase shifts of the modulation are completed and begins again with the first phase step.

The simplest solution of the data processing is the so called sequential processing in which the CPU firstly starts the evaluation algorithm until the PMD data acquisition of all N phase shifting frames have been completed and waits for the next N frames. If we consider that the PMD integration period lies usually in the order of some hundred microseconds up to some millisecond, the CPU during this time isn't efficiently used for the data processing, which means that this method doesn't make use of the full power of the CPU and leads to a low data processing rate. With the increase of the PMD pixel number in a PMD sensing array (or PMD line), the data stream and the processing time needed for the distance evaluation will rise drastically.

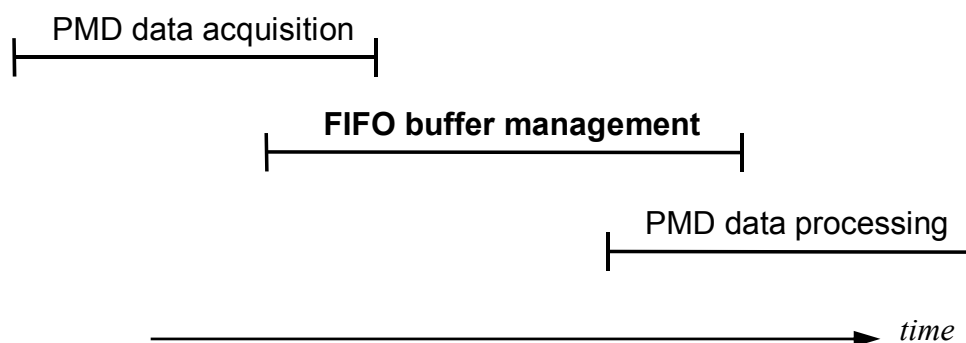


Fig. 5.21 The operating principle of the “pipeline” processing mechanism used in the PMD ranging system.

To avoid the drawbacks of this solution, the “pipeline” mechanism is introduced in the data processing. In this module a FIFO (“First In First Out”) buffer is implemented. The digitized outputs of PMD pixels at the end of each frame fulfill the buffer, and on the other side, the distance evaluation process dispatches the corresponding data from the FIFO- buffer for the processing algorithm. The buffer management routine controls the data accessing and monitors any possible under/overflow of the FIFO buffer. **Fig. 5.21** demonstrated schematically the “pipeline” mechanism of the data processing of the microprocessor. As the results, both the distance evaluation and the data acquisition process runs quasi-parallel in the microprocessor. The highest processing rate could be achieved in this way. The primary physical limitations are band width of the bus system and the CPU frequency.

As the cost we need obviously a large memory block implementing the FIFO buffer. To build an FIFO buffer of length L with 16 Bit precision, the size of the memory block corresponds

$$B_{FIFO} = 4 \cdot N \cdot M^2 \cdot L \text{ (Bytes)} \quad (5.9)$$

where N the phase shifting steps and M the row/column size of the PMD array (assuming an $M \times M$ PMD-matrix). For a 16×16 PMD ranging camera using 8-phase shifting algorithm, the FIFO buffer with length of 1K requires 8MB memory.

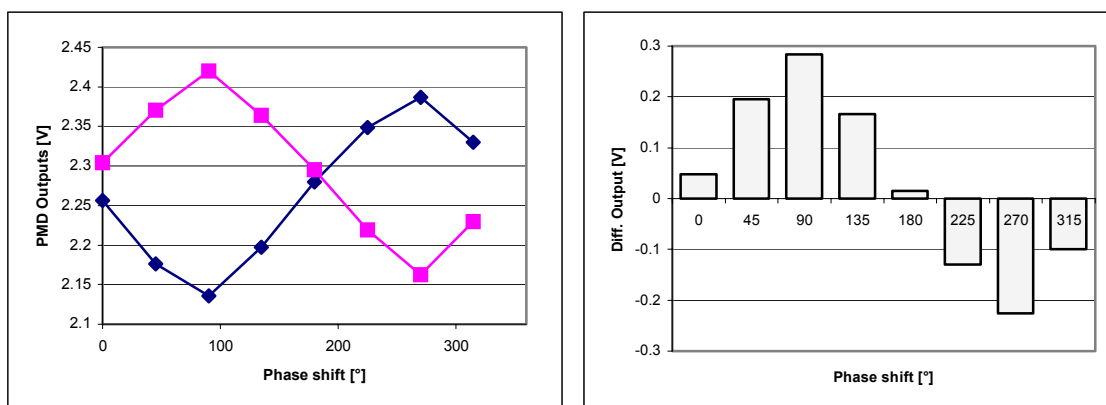


Fig. 5.22 The digitized PMD outputs (a) and the corresponding differential output at the related 8 phase shifts (b).

5.4.2 Distance evaluation algorithm

The main task of the data processing module is, of course, the phase information evaluation in order to obtain the depth information of the target. As have been discussed before, the distance measurement of the PMD ranging system described in this work uses the multi-phase shifting modulation technique and the corresponding phase evaluation algorithm based on the least square method. The 4, 8 as well as 16 phase shifting modulation algorithms are implemented in the PMD ranging system. Square wave modulation was used. **Fig. 5.22** shows the sampled outputs of a PMD pixel in channel a and b and the corresponding differential output related to the 8 – phase shifting steps.

As we know from the discussion in chapter three, since the PMD operates with push - pull modulation signals, the analog output signal U_b of the PMD is, in comparison to the output signal U_a , referred to a phase shift with 180° . So for the 4 - phase shifting modulation algorithm, e.g., only two phase shifting steps (0° and 90°) instead of all 4 phase shifts (0° , 90° , 180° and 270°) are theoretically necessary for the phase evaluation. From equations 2.20 and 2.24 the depth information of the measurement point of the target yields

$$d = \frac{1}{2\pi} \cdot \frac{c}{2f_0} \cdot \arctan \left[\frac{(U_a - U_b)_{90^\circ}}{(U_a - U_b)_{0^\circ}} \right] \quad (5.10)$$

with $c = 3 \times 10^8 \text{ m/s}$ and $f_0 = 20 \text{ MHz}$. However, some factors in practice should be taken into account in the distance evaluation. Firstly the distance errors induced by the FPN noise of the PMD pixels can not be eliminated through equation 5.10. The asymmetrical feature of the actual applied PMD chips in the PMD ranging system, which is dependent of the lateral optical illumination in some cases, as already discussed in the last chapter, could also influence the evaluation results. Such disturbances will induce an additional DC term at the PMD output, resulting in an error phase delay which can not be removed by equation 5.10. To overcome this drawback, the four phase shifting evaluation should be modified based on the differential outputs ΔU_{ab} of PMD corresponding to the phase shifts, instead of directly using the absolute sampled voltages, i.e.

$$d = \frac{1}{2\pi} \cdot \frac{c}{2f_0} \cdot \arctan \left[\frac{\Delta U_{ab,270^\circ} - \Delta U_{ab,90^\circ}}{\Delta U_{ab,180^\circ} - \Delta U_{ab,0^\circ}} \right] \quad (5.11)$$

All the above mentioned sources will arise an additional deviation from the expected value at the related output, saying U_n , the output signals of PMD U_a and U_b can be explained as

$$\begin{aligned} U_a &= U_{a0} + U_{an} \\ U_b &= U_{b0} + U_{bn} \end{aligned} \quad (5.12)$$

where U_{a0} , U_{b0} are the correlated outputs of PMD with pure modulated optical signal.

From equation 5.11 we have

$$d = \frac{1}{2\pi} \cdot \frac{c}{2f_0} \cdot \arctan \left[\frac{(\Delta U_{ab,270^\circ} - \Delta U_{ab,90^\circ}) + (U_{an,270^\circ} + U_{bn,90^\circ} - U_{an,90^\circ} - U_{bn,270^\circ})}{(\Delta U_{ab,180^\circ} - \Delta U_{ab,0^\circ}) + (U_{an,180^\circ} + U_{bn,0^\circ} - U_{an,0^\circ} - U_{bn,180^\circ})} \right] \quad (5.13)$$

with $\Delta U_{ab} = U_{a0} - U_{b0}$. If the integration period of the PMD is short enough, compared to the variation of the optical illumination, which is mostly satisfied in practice, we can consider the terms U_{an} and U_{bn} be remains constant from frame to frame with different phase shifting steps. So the error induced by U_{an} and U_{bn} in the equation 5.13 can be removed.

In the strict sense, it must be pointed out that the induced evaluation error can not be completely removed by equation 5.11. First of all, the reset noise is generally not correlated from reset to reset, normally the CDS (Correlated Double Sampling) technique, which is performed by subtraction of the values sampled during the reset and at the end of integration of the same frame, is used in the practice. Nevertheless, the influence can be significantly suppressed by using the differential outputs in the multi-phase shifting algorithm.

5.4.3 Data filtering and thresholding

The noise performance of the ranging system depends not only on the PMD but also on the quality of the system design. The induced noise and cross-talks from different components in the system themselves are usually stronger than the noise level in the PMD pixel even with very careful system optimization. These noise sources will, as result, influence further the accuracy of the distance evaluation. Although the SNR of

the system will be improved by a factor \sqrt{N} if using the N -step multi-phase shifting evaluation algorithm to achieve higher distance measurement precision, it is necessary to employ additional processing methods to further suppress the influence of noise. The typical consideration of the noise reduction is obviously the implementation of low-pass digital filter. Since the data processing is carried out in the pure digital domain, various digital filter concepts can be applied. Due to its simple structure and under the consideration of the concrete system hardware, the N -tap FIR (Finite Impulse Response) digital filter, as illustrated in **Fig. 5.23**, was implemented in the system.

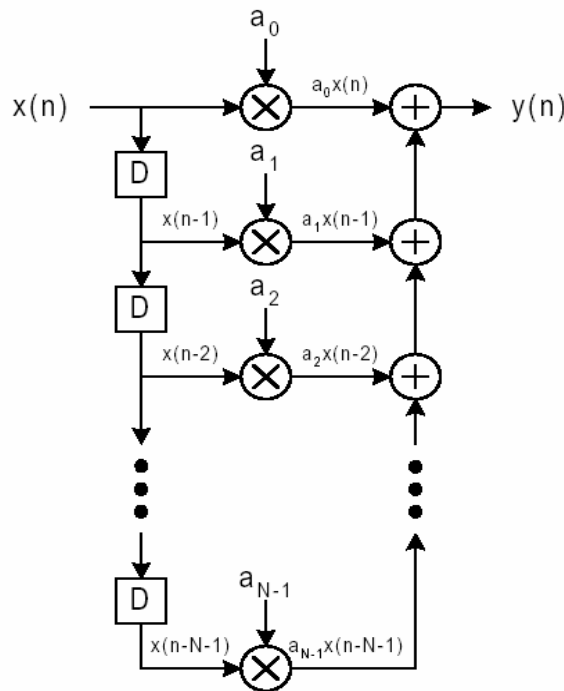


Fig. 5.23 Block diagram of a typical N -tap FIR low-pass digital filter.

The output of the filter can be presented as

$$y(n) = a_0x(n) + a_1x(n-1) + a_2x(n-2) + \dots + a_{N-1}x(n-(N-1)) \quad (5.14)$$

with a_0, a_1, \dots, a_{N-1} the constant coefficients.

By applying the z -transform the transfer-function of the filter is given as

$$H(z) = a_0 + a_1z^{-1} + a_2z^{-2} + \dots + a_{N-1}z^{-(N-1)} \quad (5.15)$$

where $z = e^{-j\omega}$, $\omega = 2\pi f / f_s$ and f_s is the sampling frequency. We see that the filter described by equation 5.14 is nothing else than an averaging function with the moving window of size N , if letting $a_0, a_1, \dots, a_{N-1} = 1/N$. Since PMD output signals are sampled at the end of each integration frame, so the sampling frequency is just the same as the reciprocal of the PMD integration period. For a PMD integration frame of 1ms, the frequency response of the 10-tap filter is drawn in **Fig. 5.24**, in which all the coefficients $a_0, a_1, \dots, a_9 = 0.1$. This filter structure is directly implemented by the software in the microprocessor, where the number of taps of the filter N can be flexibly changed as parameter in order to obtain the maximum noise reduction performance.

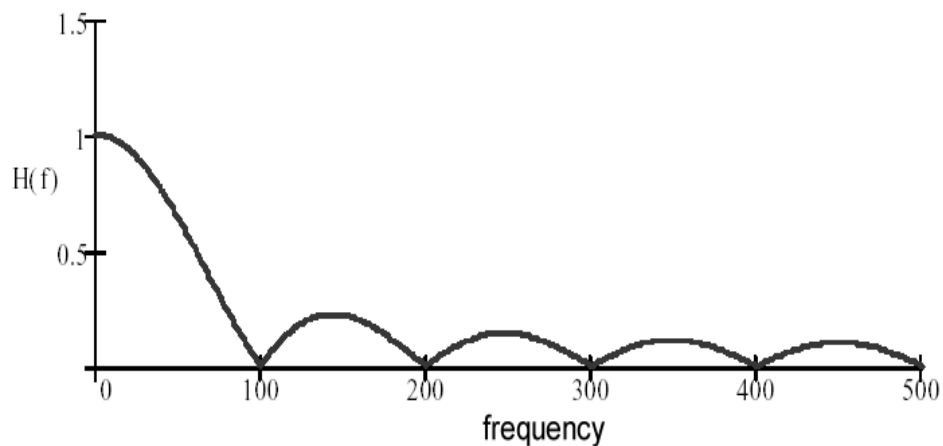


Fig. 5.24 The frequency response of the 10-tap filter for $a_0, \dots, a_9 = 0.1$, and $f_s = 1\text{KHz}$.

From equation 5.14 and 5.15, it is apparent that with increasing the taps N , the rolloff of the frequency response of the FIR filter is becoming sharper, resulting in stronger noise suppression performance. In the time domain, however, this will lead to an increasing overall delay through the filter, and the filter can not follow fast varying input signals. In order to achieve fast response of the system without loss of the accuracy of the distance measurement, the above described FIR filter concept is modified, that the size of the moving window of the LP-filter changes adaptively, depending on variation of the distance value, where the window size N is shrinks to a small size N_{min} ($N_{min} \geq 1$), if the

variation of measured distance values overrides the threshold. Otherwise it increments back to its normal size N . The threshold can be either set fixed or be estimated steady based on the standard deviation of past N measurements. **Fig. 5.25** shows corresponding responses of the adaptive filter in case of step input, in comparison to the normal N -tap filter mentioned above. One can see that the performance of the system is considerably improved.

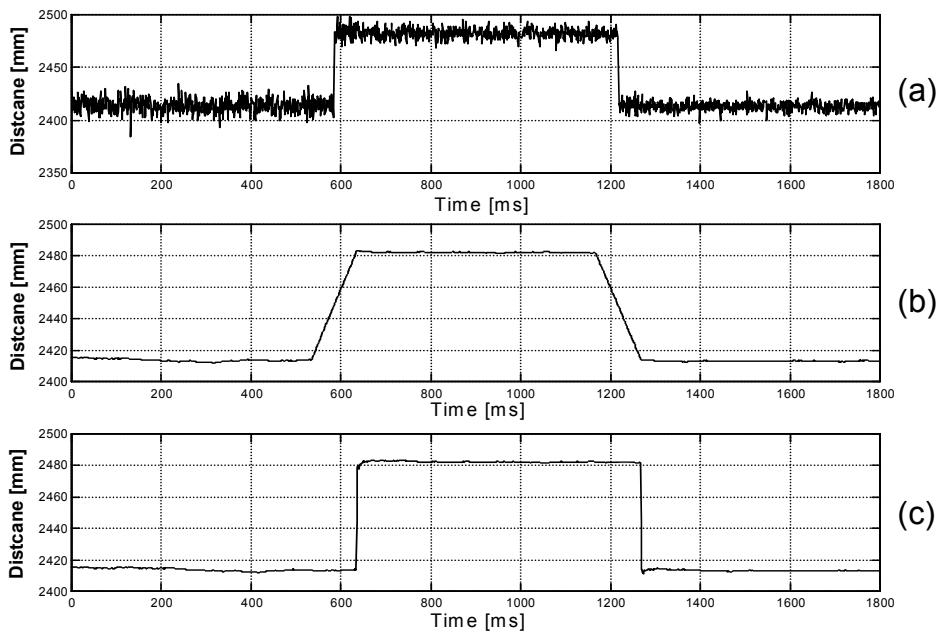


Fig. 5.25 The performance of the system by using the low-pass filter with adaptive thresholding. (a) The original distance value, (b) the responses of a simple FIR filter and (c) the processing result using adaptive filter for the step input.

5.4.4 Sub-sampling technique and adaptive integration control

The sub-sampling is performed during the PMD integration period. As mentioned previously, the PMD integration frame is normally between some $100 \mu\text{s}$ and some milliseconds, dependent of the surface characteristic of the object. Instead of digitizing the PMD outputs only one time at end of the integration, the PMD output is sampled N points with the sampling frequency f_s , where $N = T_{\text{int}} \cdot f_s$, with T_{int} the integration time, as

shown in **Fig. 5.26**. The sum of the total samples which are used for distance evaluation is given by

$$\Delta \bar{U}_{ab} = \frac{1}{N} \cdot \sum_{i=0}^{N-1} \Delta U_{ab}(n-i) \quad (5.16)$$

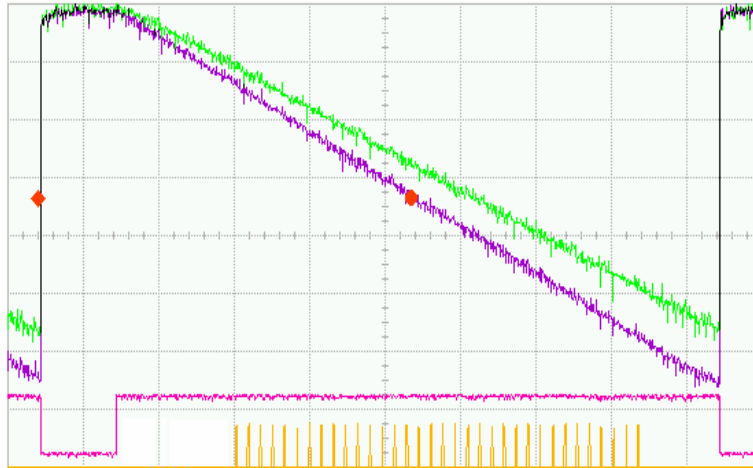


Fig. 5.26 The sub-sampling of the PMD output during an integration period.

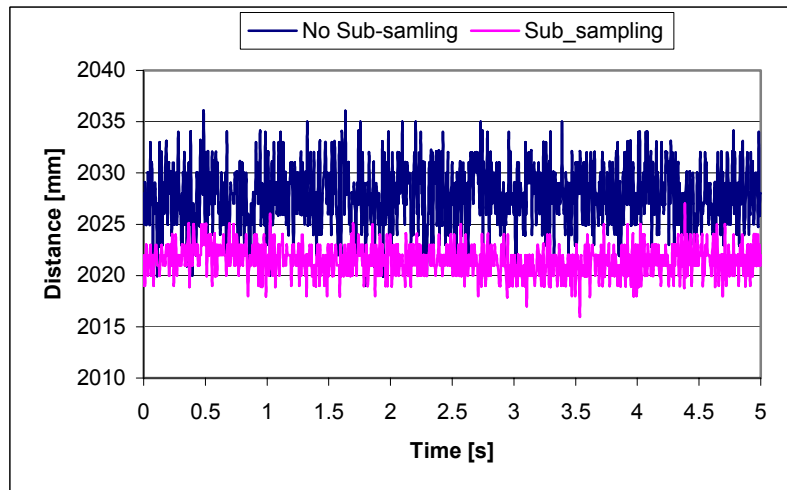


Fig. 5.27 The measurement results of an 1D-PMD ranging camera with the sub-sampling, compared to the measurement with normal evaluation with $T_{\text{int}} = 500 \mu\text{s}$. No distance calibration was applied in the measurement. Two measurements were performed with different distances.

It is apparent that the sub-sampling of PMD is the special form of the N -tap FIR lowpass filter described by equation 5.14 and 5.15 with $a_0, a_1, \dots, a_{N-1} = 1$. However, this realization has a distinct advantage than the implementation of the lowpass filter following the distance evaluation, as discussed previously in the last section. Since the sub-sampling is performed during the integration of the PMD, it introduces not additional overall delay for the data processing, so that the response of the system isn't affected. The measurement results of a 1D-PMD ranging camera with sub-sampling technique, compared to the normal operation are illustrated in **Fig. 5.27**.

For a given integration period T_{int} , the improvement of the sub-sampling is dependent of the sampling frequency f_s as well as the time point of begin of sampling. From the point of view of the signal to noise performance of the system, increasing the sampling frequency f_s means growing the number of total samples N , which corresponds to the improvement of the overall signal to noise performance. On the other hand, however, the sub-sampling referred to equation 5.16 causes also the loss of the equivalent amplitude of the differential output of PMD which in turn causes the degradation of the overall signal to noise ratio, resulting in loss of evaluation precision. As depicted in the **Fig. 5.28**, to obtain the optimal sub-sampling performance of suppression system noise, one should need carefully to choose the start time point t_0 and the corresponding sampling rate f_s .

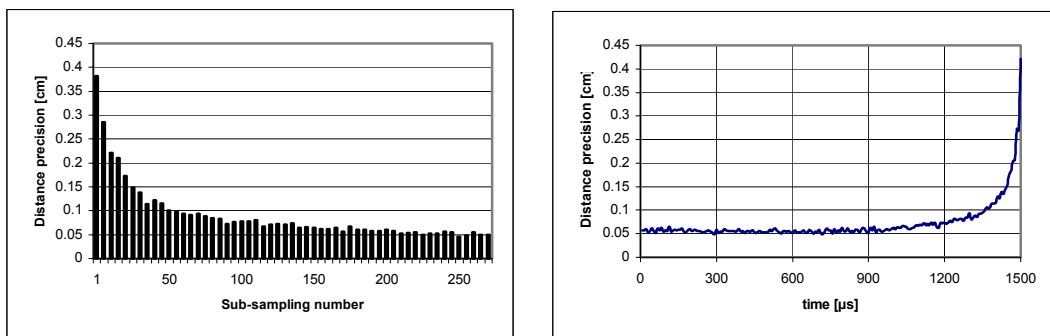


Fig. 5.28 The distance accuracy improvement of the sub-sampling technique. (a) The distance precision related to different sampling frequency (corresponding to the total samples N in the integration period), in case of $t_0 = 0$; (b) the influence by selecting the different time points to start the sub-sampling.

To ensure the higher performance and the reliability of the data processing, the PMD sensor system should have the ability of self adjustment according to the different surface features of the target. As we know that the PMD performs the correlation of the back-scattered optical signal and the electrical gate modulation signal of PMD. The output of PMD over the integration interval T_{int} is given by

$$U_v(\tau) = \frac{Q_v(\tau)}{C_{int}} = \frac{K}{C_{int} T_{int}} \int \eta(\lambda) \cdot P_{opt}(t-\tau) \cdot U_{vm}(t) dt; \text{ for } v = a, b \quad (5.20)$$

where C_{int} is the total equivalent integration capacitance, $P_{opt}(t-\tau)$ the reflected optical signal from the object surface and η the corresponding quantum efficiency. It is apparent that the output is proportional to the power of the reflected optical signal and the integration time. Either long time interval T_{int} or very strong reflection from the target could induce the saturation of the integration (see also **Fig. 4.24**), resulting in non-linearity of the PMD output, which can only be partly compensated, as have been discussed previously, through the multi-phase shifting evaluation algorithm [Xu-1]. To prevent the output of PMD from going into the saturation area of the PMD, the time-adaptive integration was introduced, where the T_{int} changes adaptively according to the power of the reflected optical signal. This feature works together with the sub-sampling technique. For a given power of reflection, although the outputs U_a and U_b of PMD are very different as the phase changes from frame to frame, the sum of them ΣU_{ab} , representing the gray tone, can approximately be considered as constant during the N phase shifting frames. The actual time interval T_{int} is determined in each first frame by sub-sampling the outputs of PMD until the term ΣU_{ab} exceeds the predefined threshold U_{sat} , i.e. $\Sigma U_{ab} \leq U_{sat}$, and the corresponding integration time will be applied for the subsequent $(N-1)$ integration frames.

5.5 2D Range measurement

We present in this section the first 2D non-scanning PMD ranging system using the multi-phase shifting modulation technique. The system architecture of the 2D PMD ranging camera is almost the same as the PMD ranging sensor concept described in the previous sections, with the exception that the modulated light beam of the laser diode is projected into a line to illuminate the scene by an HOE objective. The complete

2D PMD ranging camera is shown in **Fig. 5.29**. Compared to the scene illumination by the LED array, the phase homogeneity of the optical signal is ensured through the HOE element, this is important for the distance ranging system of high measurement precision, especially in the near field, since the phase difference will induce additional distance evaluation error. The phase differences, if using LED array, could either be caused by electrical delays of LED drivers on the PCB or technical variations between the single LEDs.



Fig. 5.29 The first compact 2D PMD ranging system based on the multi-phase shifting modulation technique.

The PMD sensor is based on an actual PMD line with 8 pixels which was fabricated by S-TEC. **Fig. 5.30** shows the chip photo of the PMD line sensor and the corresponding readout timing diagram. After the integration, the outputs of all PMD pixels are serially read out in the order of $A1, B1, A2, B2, \dots, A8, B8$, under the control of the pixel readout clock signal. Due to the eye safety limitation the total optical power of the laser diode is set at ca. 1mW, just the same as that of 1D PMD ranging system. This corresponds, however, the reduction of received optical power of each PMD pixel in the applied PMD line by a factor of about 8 under the same operation condition. To acquire the equivalent power budget as that of the 1D PMD sensor one needs respectively longer integration time.

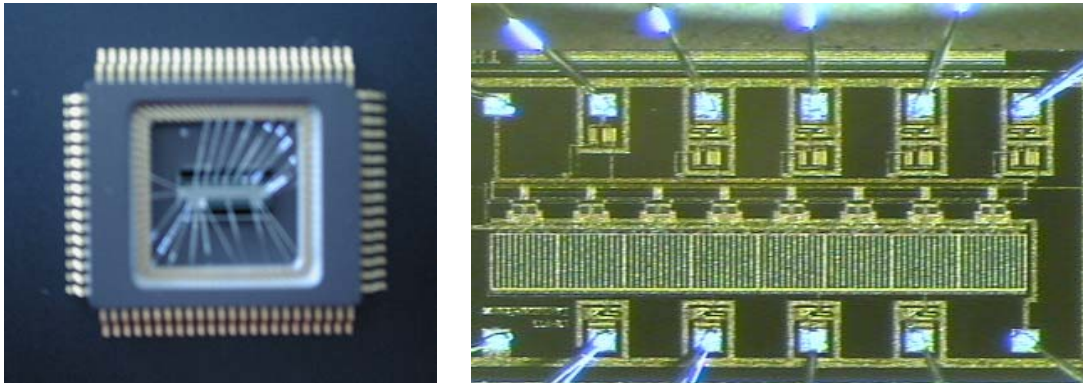


Fig. 5.30 The PMD line sensor with 8 pixels on chip Z4-3. Link: the chip photo, right: the micrograph of the chip.

Fig. 5.31 shows the measured modulation contrast of each PMD pixel of the PMD line sensor under the homogeneous illumination. The PMD operates at the modulation frequency of $f_{mod} = 20$ MHz. The measurement was performed at an average photo current of $i_{photo} = 3$ nA.

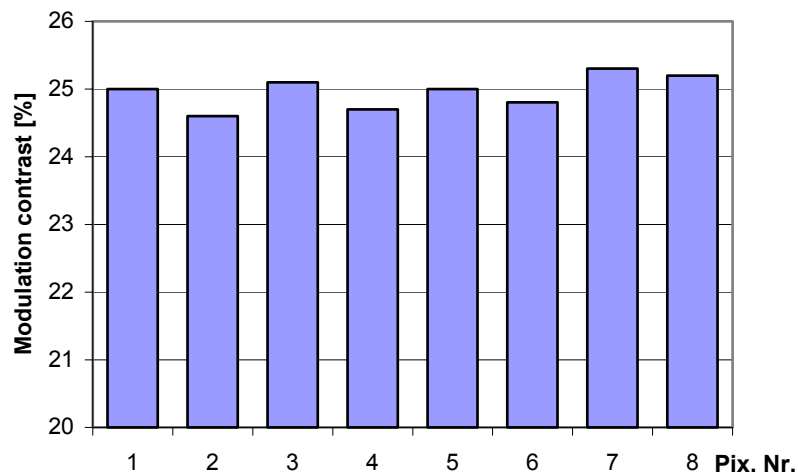


Fig. 5.31 Measurement results of the modulation contrast of the PMD line Z4-3. $\lambda = 635$ nm, $f_{mod} = 20$ MHz, $i_{photo} = 3$ nA.

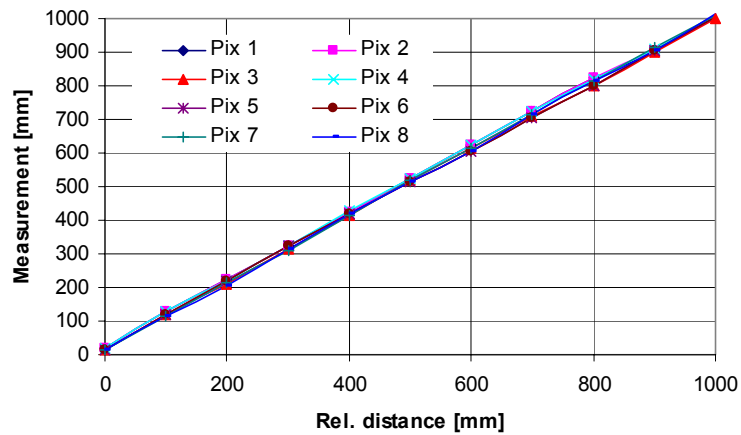


Fig. 5.32 Measurement results of the PMD line ranging sensor Nr.3

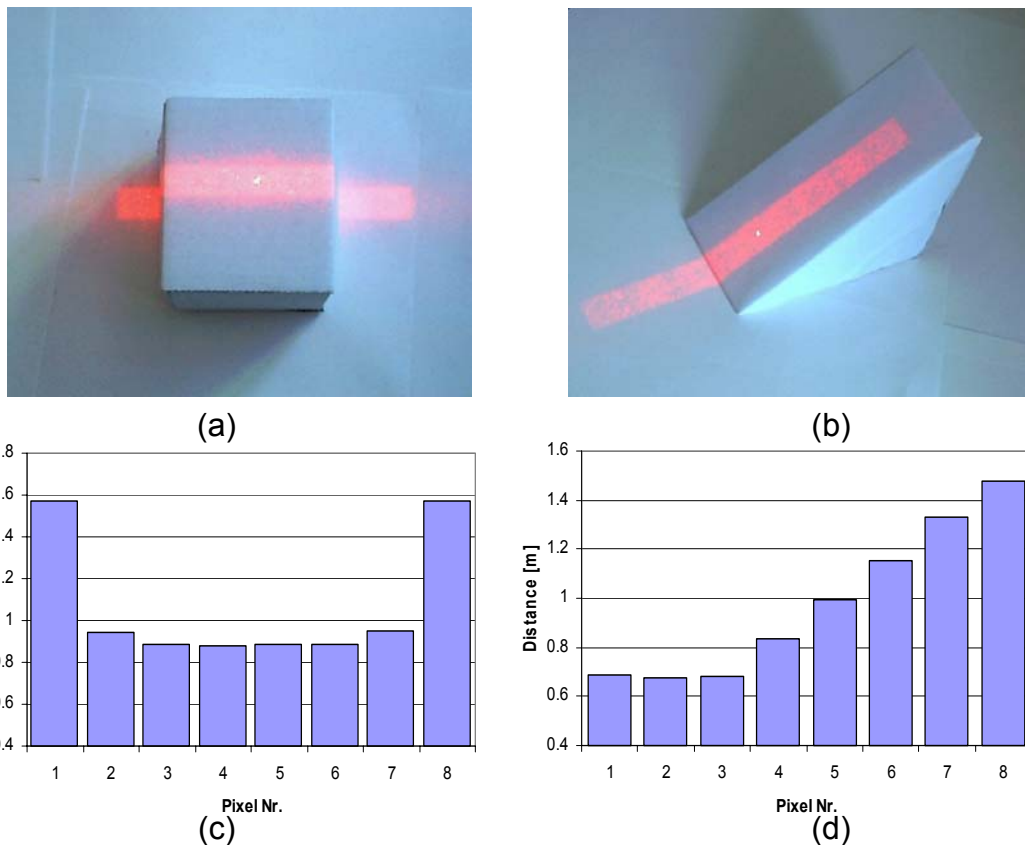


Fig. 5.33 Measurement results of different objects by using a PMD line ranging camera. (c) Measured distance profile of a white paper box (a). (d) The measurement result over the cross-section of an object with triangular shape (b).

Finally we present the results of distance measurements performed the PMD line ranging system described above. The system operates at the modulation frequency of 16.25MHz and the depth information is obtained based on the eight phase shifting evaluation algorithm [Xu-1]. The measurements of all pixels over a distance range of 1 meter are illustrated in **Fig. 5.32**. As target of the measure the white sheet of paper was used. The integration time of each phase shifting frame was fixed at $T_{int} = 15\text{ms}$. The measurement result shows an accuracy of better than 5mm without sub-sampling and averaging, as demonstrated in the **table 5.2**. **Fig. 5.33** shows the measured profiles of cross-sections of two objects of different shapes, one the same as shown in **Fig. 5.36b** and one with shape of triangle, both made of white paperboard.

Table 5.2 Accuracy of the distance measurement of the 2D PMD ranging camera

$\lambda = 635\text{nm}, f_{\text{mod}} = 16.25\text{MHz}, T_{\text{int}} = 20\text{ms}$								
Pixel Nr.	1	2	3	4	5	6	7	8
Std. deviation [mm]	4.86	4.47	4.28	4.18	4.24	4.13	4.63	4.97

The result is based on the measurement within the distance range between 1m and 2m at the white paper sheet by using the 2D-PMD demonstrator Nr. 3.

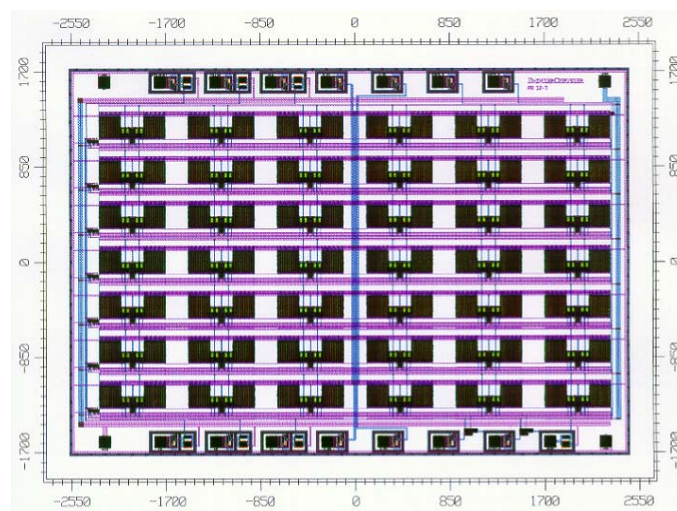


Fig. 5.34 The architectural overview of the PMD array DC7x12

5.6 3D range measurement

Finally, we demonstrate in this section the 3D ranging results directly measured by using the PMD sensing array. The applied chip in the measurement was the first fabricated prototype of the PMD matrix, with totally 7 x 12 PMD pixels integrated on it. **Fig. 5.34** gives the architectural overview of the PMD chip. As shown in the timing diagram of the PMD chip in **Fig. 5.35**, the reset of all the PMD pixels is performed at the beginning of each integration period. The outputs of the PMD pixels are row-wise serially read out through the control of clock signal. The PMD pixel has the same finger structure as those we have discussed in the previous chapters.

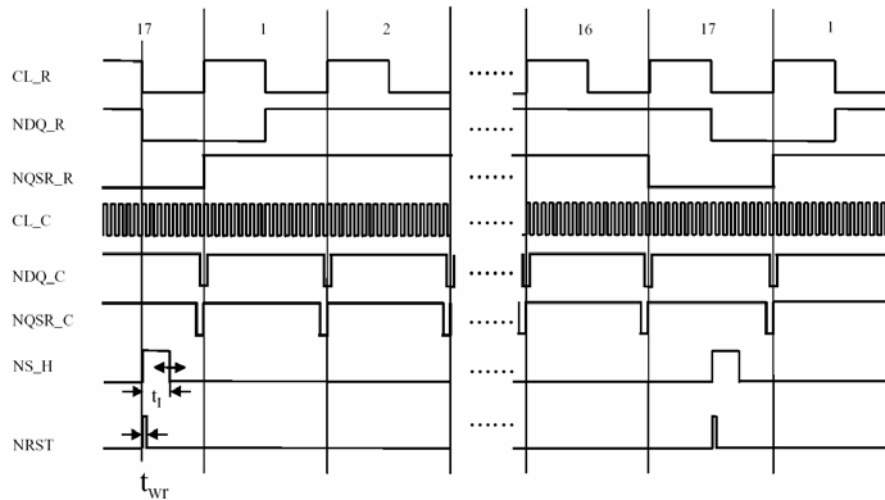


Fig. 5.35 Readout timing of the DC7x12 PMD sensing matrix

The same light source module which was applied in 1D and 2D PMD ranging cameras was used for the area illumination. In contrast to the applications of distance measurement using 1D or 2D PMD line sensor under the same condition, the optical power of the light source which is required for the scene illumination will be drastically higher. Although the laser module which is applied for optical illumination, compared to the LEDs, has the advantage of phase homogeneity, the optical power cannot be increased at will, due to the eye safety limitation in practice, with exceptions of sensor applications in some special environments. So for the same optical power, each PMD pixel in the array receives much less light as in 1D PMD sensor. Therefore, one needs to increase the integration time of PMD, resulting in the degradation of sensing rate of

the system. In order to acquire enough optical intensity for the area illumination, LEDs are usually used as light source. In general, a number of LEDs are arranged to build an LED array of different forms to satisfy distinct scene illuminations. Such LED modules are capable of delivering a total optical power of from some ten milli Watt up to some Watt.

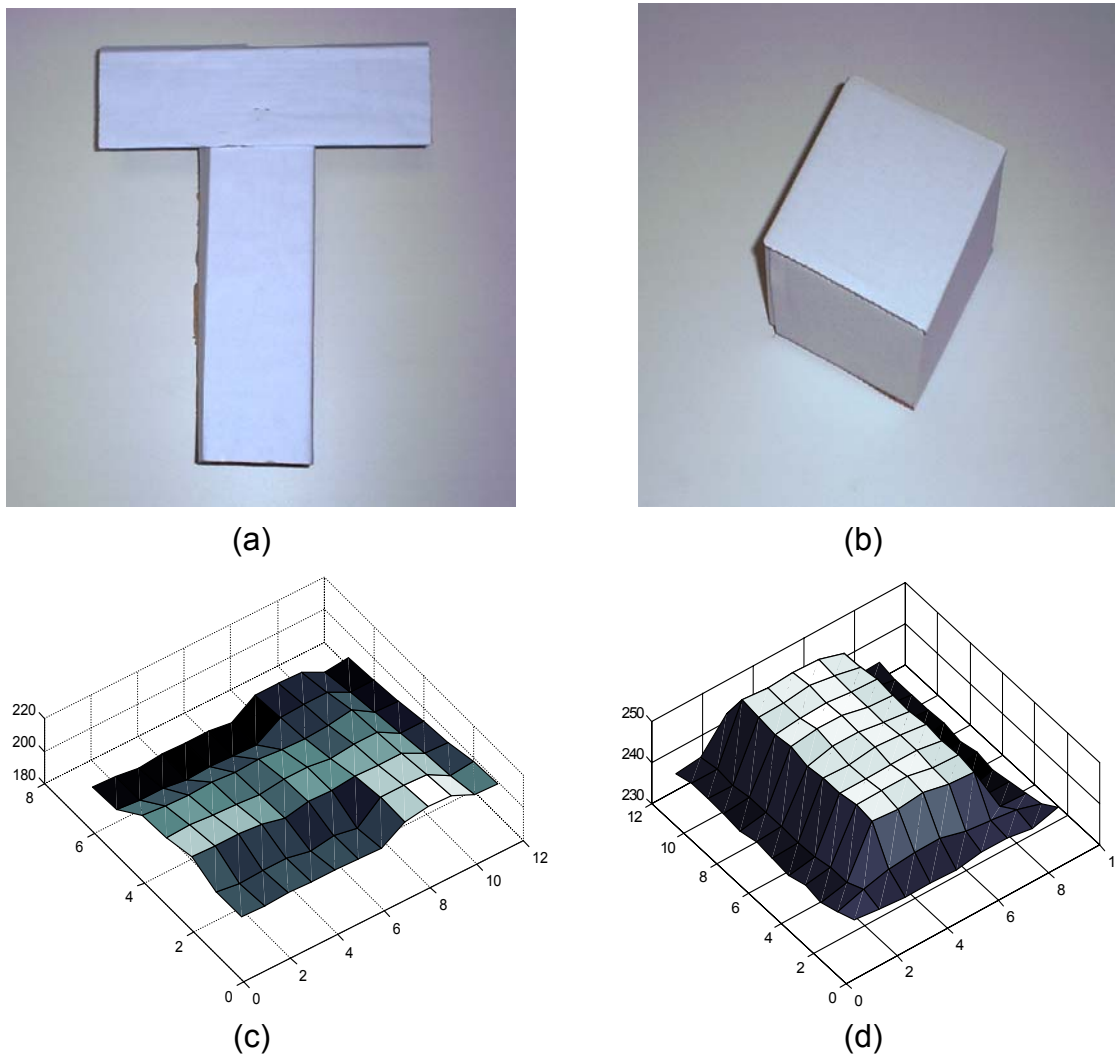


Fig. 5.36 Photos of the test objects and the graphical representation of the 3D information acquired by using a 7x12 PMD array. The scene was illuminated by an laser module of $\lambda = 635\text{nm}$. Both the test objects and the background has the same color.

Similarly to the 1D and 2D PMD ranging cameras, the evaluation of the phase information is based on the 8-phase shifting algorithm. The range measurements of 3D

scenes are illustrated in **Fig. 5.36**. Two objects, made of white paperboard, one box of size $20 \times 32 \times 10.5$ cm and one object of size $20 \times 32 \times 9.5$ cm, with a shape of “T” form, as shown in **Fig. 5.36a**, were used as target in the bright background. As a graphical representation, the acquired corresponding 3D data of the objects are illustrated in **Fig. 5.36b**.

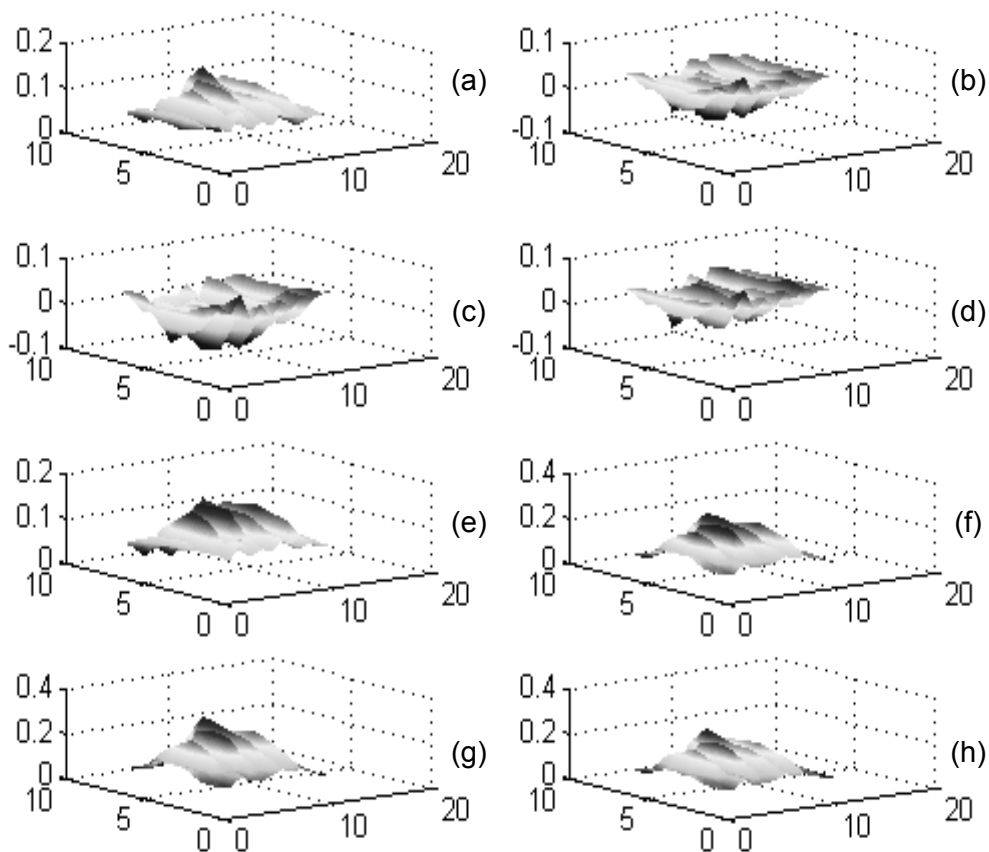


Fig. 5.37 The PMD differential outputs (RF-interferogram) corresponding to the 8 phase shifting frames. The amplitude presented in “z” – axis is drawn in pseudo-color.

The measurement was performed by using 8 – phase shifting technique described in chapter two. The frequency of the square wave modulation is 20MHz which corresponds to an unambiguous distance of 7.5 meter. The differential signals of the PMD matrix between the outputs A and B of each pixel, related to the eight phase

shifting frames, are presented in **Fig. 5.37a – h**, where the amplitude of the differential signals in “z” – axis is drawn in pseudo-color.

As discussed in the previous sections, the output of the PMD includes, in addition to the phase information referred to the corresponding distance and phase shifts, the fix pattern noise (FPN) as well. Since the FPN can be approximately considered uncorrected from frame to frame, the FPN of PMD is simply obtained by summing the differential outputs of all eight phase shifts. Similarly, the summation of the PMD outputs A and B corresponding to all eight phase shifting frames eliminates the AC components induced by different phase shifts and gives therefore the intensity image of the target scene. The resulted FPN, presented as gray scale graph and the obtained intensity image of the test object – the white paper box shown in **Fig. 5.36b** – are shown in **Fig. 5.38** and **Fig. 5.39b** respectively.

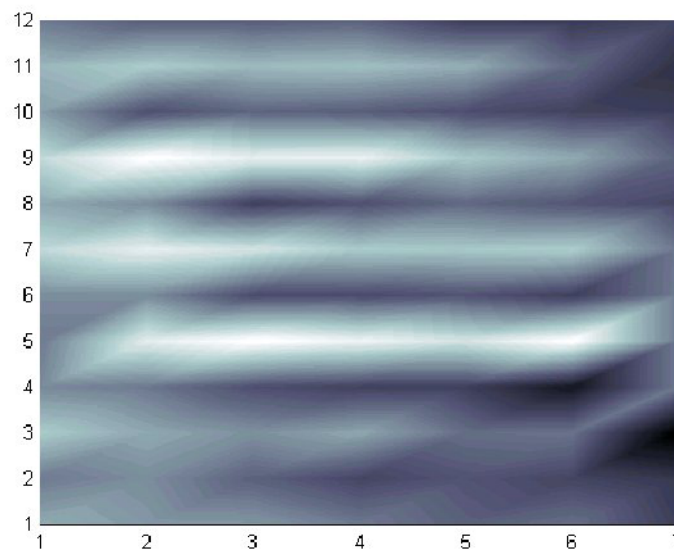
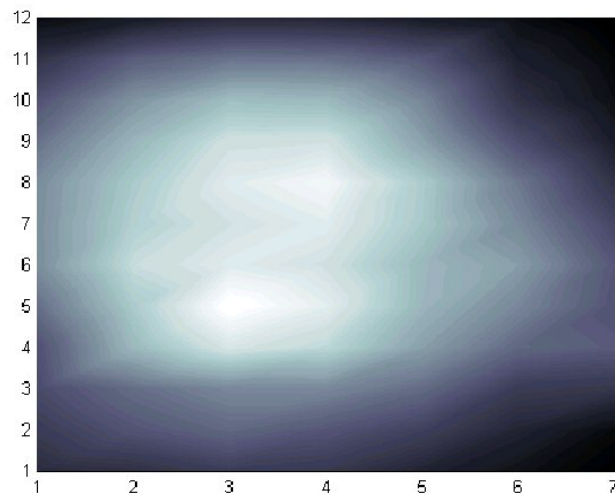


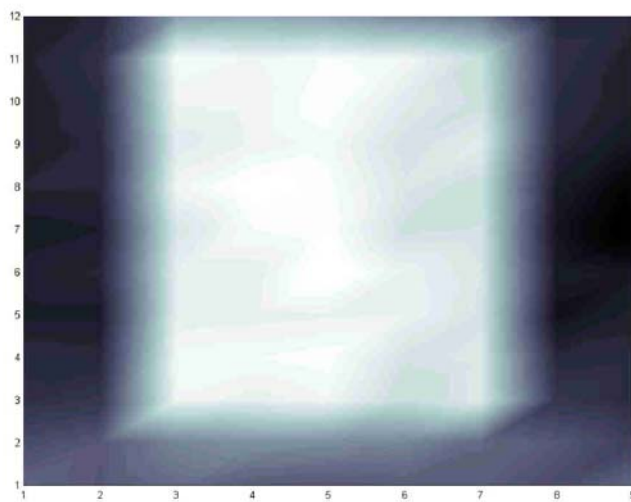
Fig. 5.38 The measured fix pattern noise of the PMD array DC7x12

Although one can rarely identify any geometrical characteristics of the white paper box from the intensity image shown in **Fig. 5.39a**, since the object has the same white color as the background, in comparison, the 3D information of the same test object measured by the PMD matrix is clearly to see. As we know from the previous discussion, the influence of the FPN on the depth information can be considerably suppressed by the

corresponding multi-phase shifting evaluation algorithm. For a correct presentation of the intensity image of the 3D scene, however, similarly to the CCD and CMOS imaging sensors, the FPN could be completely eliminated through the so called correlated double sampling (CDS) technique [HoLu].



(a)



(b)

Fig. 5.39 (a) The intensity image of the white paper box obtained by the 3D PMD array. The influence of FPN is partly corrected by subtracting the FPN shown in (a) from the raw data. (b) The corresponding 3D image of the object drawn in gray scale.

6 The measurement accuracy and error compensation

In chapter 5 we discussed the configuration of the PMD TOF ranging systems with the phase shifting technique and presented the measurement results based on the actual fabricated PMD sensing chips. Finally, we give a discussion about some factors that influence the system performance of the PMD sensors and 3D data correction.

6.1 Distance accuracy of the system

The performance of the PMD ranging system is limited by the noise. The essential noise sources of PMD are shot noise, thermal noise, reset noise and 1/f noise [Xu-1] as well as other system noise sources such as phase jitter noise of the phase shifting module and quantization noise of A/D converter. Following the Gauss error propagation's law, the phase evaluation uncertainty using the multi-phase shifting modulation technique yields

$$\delta\varphi = \sqrt{\sum_{k=1}^N \left(\frac{\partial\varphi}{\partial I_k} \right)^2} \cdot \delta I_k \quad (6.1)$$

in which I_k is the PMD output signal defined by equation 2.19 and δI_k defines the standard deviation. Solving for all N phase values $\psi_k = \frac{2\pi}{N}k$ for $k=1,2,\dots,N$ the obtained relation between the range accuracy of measurement and the modulation contrast as well as system signal to noise SNR is described by [He-1]

$$\delta R = \frac{\lambda_{mod}}{4\pi} \cdot \delta\varphi = \frac{\lambda_{mod}}{4\pi} \cdot \frac{1}{\sqrt{N}} \cdot \frac{1}{SNR} \cdot \sqrt{1 + \frac{2}{K^2}} \quad (6.2)$$

where λ_{mod} is the corresponding wavelength of the modulation frequency, N the total phase shifts and K the equivalent modulation contrast defined by equation 4.12.

The relation above described the absolute limit of the PMD ranging sensors working with the phase shifting technique. One can see from the equation that the measurement accuracy depends not only on the system contrast K but also on SNR which is equivalent to the dynamic range in case of PMD. As discussed previously, the background illumination, the optical power and the modulation depth of the modulated light source, distance and reflectivity of the target, as well as the modulation contrast of

PMD can influence the performance of the PMD ranging system. In contrast to the power of optical signal and the PMD modulation contrast, the background illumination increases the distance uncertainty of the system, because it restricts the system contrast and causes additional quantum noise of the system. The background illumination can be generally reduced by using special optical filters that blocks the light out of the spectrum of the optical modulated signal. This can not completely eliminate the influence of the background illumination, since the spectral distribution of the background usually covers the optical spectrum of the modulated light. An other solution is the PMD pixel with integrated on-chip SBI circuit which based on the fact that the uncorrelated background illumination generates the same photo current during the integration period in the PMD output channels A and B , which can be removed respectively by the SBI, keeping the dynamic range of PMD in the best case unchanged [S-TEC].

The measured distance uncertainty grows with the distance to the object grows. Since, generally, the optical power density of the modulated light source on the illuminated 3D scene decreases with increasing distance to the target, compared to that of background illumination (e.g. daylight) which maintains quasi-constant within the whole measurement range, the measurement uncertainty will also increase due to the loss of system contrast.

As an example, **Fig. 6.1** and **Fig. 6.2** show the influence of the modulation contrast of PMD as well as the background illumination, as single parameters, on the measurement uncertainty over a range of $R = 1 \sim 7\text{m}$. Assuming that the light source with a 100 % modulation depth has a total optical power of $P_{opt} = 1\text{mW}$, emitting at $\lambda = 635\text{nm}$ with an divergence of 20° , where the PMD with finger structure has a quantum efficiency of about $\eta = 0.13\text{A/W}$. The modulation frequency is chosen at $f_{mod} = 20\text{MHz}$ which corresponds to a wavelength of 15m . We use a lens with focal length of $F=30\text{mm}$ and an aperture index $F\# = 1$.

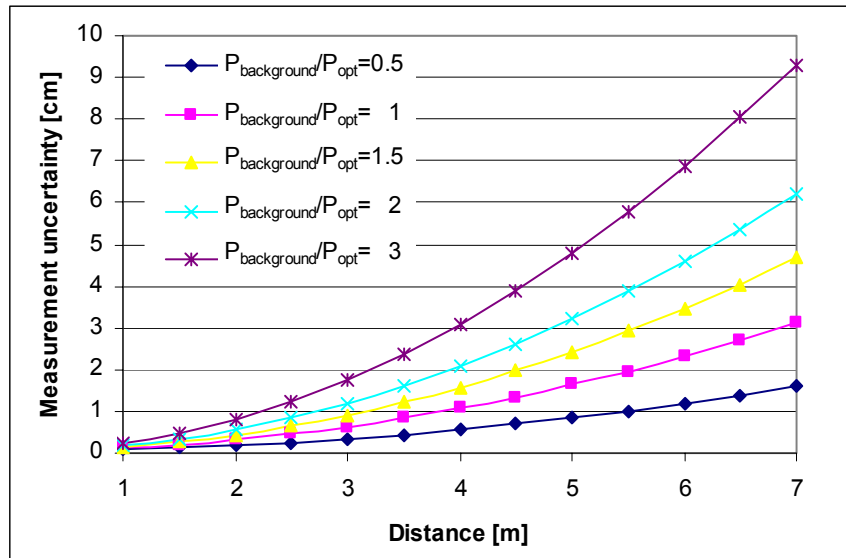


Fig. 6.1 Distance accuracy versus the background illumination over a range of 1 ~ 7m. The power of background illumination is calculated relative to the optical power of light source. $K_{PMD} = 30\%$. $C_{int} = 1\text{pF}$, $f_{mod} = 20\text{MHz}$.

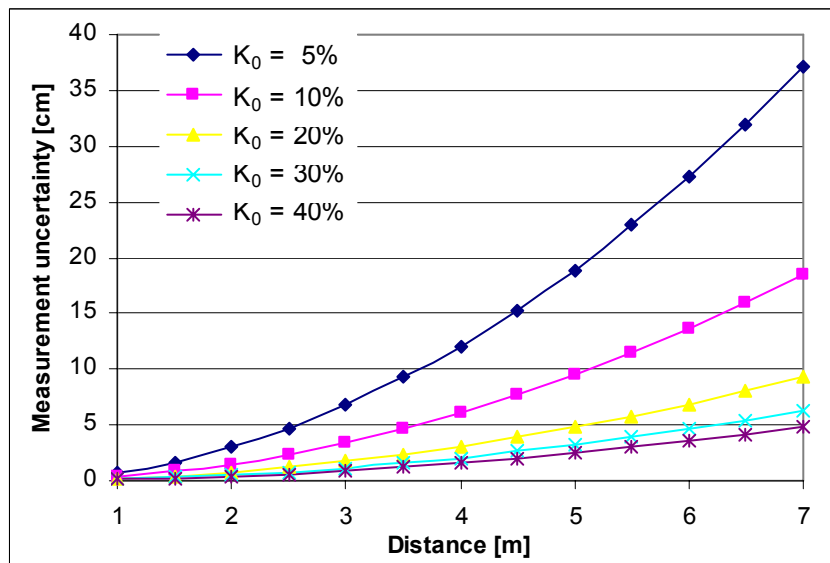


Fig. 6.2 Distance accuracy under the different modulation contrast over a range of 1 ~ 7m. There is no background illumination. The modulation contrast of PMD varies from 5% ~ 50%. $C_{int} = 1\text{pF}$, $f_{mod} = 20\text{MHz}$. $V_{dark} = 0.6\text{mV rms}$, $T_{int} = 2\text{ms}$.

6.2 Distance reference technique

The reference technique is the typical method to calibrate the TOF ranging systems. As we have known that the TOF ranging system obtains the distance from the phase delay information of the optical signal. There are many factors that can influence the measurement precision of the ranging system, such as the signal form aberration induced by the changes of temperature or aging problem of single system components [Olk]. As an example the distance information measured based on some PMD pixels of a PMD line ranging camera are presented in **Fig. 6.3**. The change of the system temperature during the measurement causes not only the change phase relation between the transmitting and receiving channels but also the amplitude of the optical signal, which induces straight forward the distance measurement error.

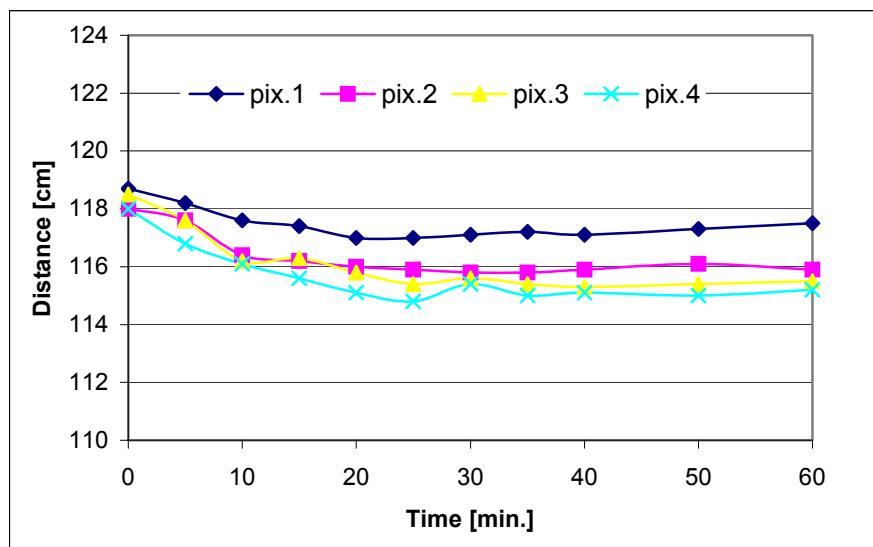


Fig. 6.3 Drift errors of the system due to the change of temperature after power-up, measured based on a 2D PMD line ranging system without referencing technique implemented.

Such drift errors can not be eliminated by the system itself. It is, therefore, necessary to implement the referencing technique to compensate the error. Different concepts of distance referencing can be used for TOF ranging systems [Olk][He-1]. **Fig. 6.4** shows one solution of error compensation through the reference technique in the 3D PMD ranging systems. Compared to the description of PMD ranging system in the previous

chapter, an optical referencing “path” is added directly to the PMD chip in the system. A part of the modulated optical signal from the same light source is branched to the PMD during the reference measurement frame, through a glass fiber. The real distance information of 3D scene is acquired by subtracting the reference data from measurement result. One can see that the drift error induced by the distinct system components can be completely compensated and will not appear in the final measurement result, since both the referencing and the measurement of the target use the same transmitting and receiving channels, the influence of the drifting effect of the system components on both measurements are identical which can then be eliminated from the measured data.

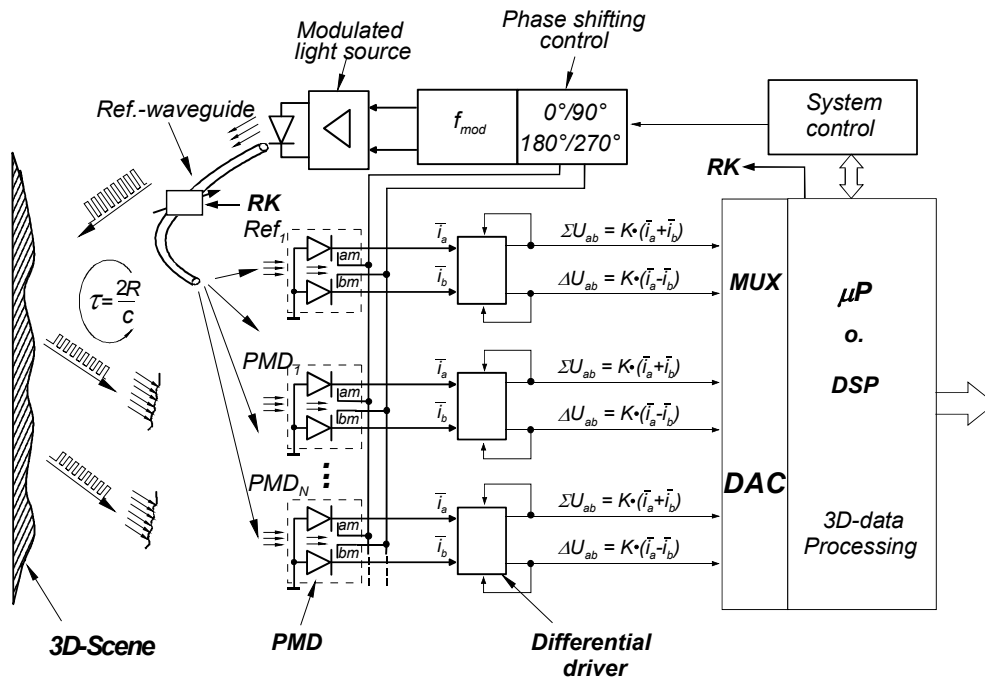


Fig. 6.4 Block diagram of the reference technique for 3D PMD ranging system [Scw-3]

Another variant of the above described reference concept of the 3D PMD ranging system is the separation of the reference channel of the system through one or more PMD pixels used as reference pixel. The on-chip integrated reference PMD pixel has the same feature as other PMD pixels in the array that ensures nearly the same performance of error compensation. In contrast to the conventional ranging systems,

there isn't much more additional technical cost necessary even with the introduction of the referencing technique, due to the unique features of PMD technology.

6.3 Non-linearity error and phase shifting evaluation

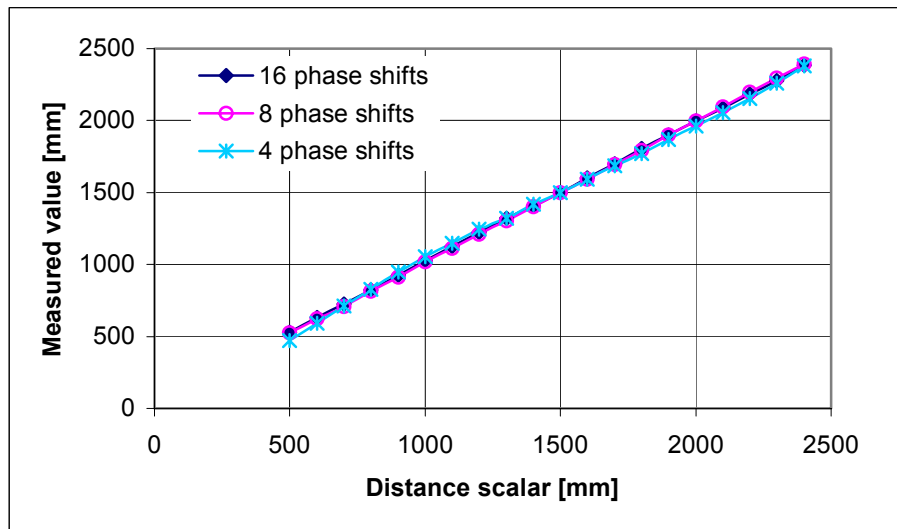
Non-linearity of the system is another main error source for the high accuracy of the distance measurement. As been discussed in the previous chapters, many factors can cause the non-linear performance of the system, such as the optical modulator, demodulator (PMD), signal generator as well as strong variation of the system operation condition (e.g. temperature). In general, non-linearity is a problem that exists in almost every real system. To minimize and reduce the influence of the non-linearity, the first and most important step is of course the improvement of hardware, which ensures the robust operation and a large linear range. Other system processing method such as the adaptive integration time control of PMD, as discussed previously, can further prevent the system the non-linearity induced by the saturation effect. However, such technique is very time- and cost-consuming and therefore not suitable for the application of 3D ranging system using PMD array. For a 3D scene with very strong image contrast, there are still some pixels that will be in saturation after the integration period. As the last insurance, the optimized multi-phase shifting evaluation algorithm plays an very important role in suppressing the non-linear errors of an 3D TOF PMD ranging system.

As result, the non-linearity of the system will induce the distortion of the auto – correlation curve of the system, which is presented in the frequency domain by the appearance of a series of the high order of unexpected harmonics. In addition to the averaging effect of the system noise, the multi-phase shifting evaluation algorithms can reduce considerably the influence of the non-linearity of the system by suppressing the contribution of the corresponding high order harmonics [Xu-1]. Table 6.1 lists the suppression of effect of different harmonics by the multi-phase shifting evaluation. The more phase shifts are used for the data evaluation, the more terms of high order harmonics are to be eliminated, resulting higher ranging accuracy. On the other hand, it means considerably growing the data stream to be evaluated and requiring longer measurement time with the increasing phase shifts, especially for the 3D PMD arrays. Considering the fact that the high order terms of the harmonics in the auto-correlation

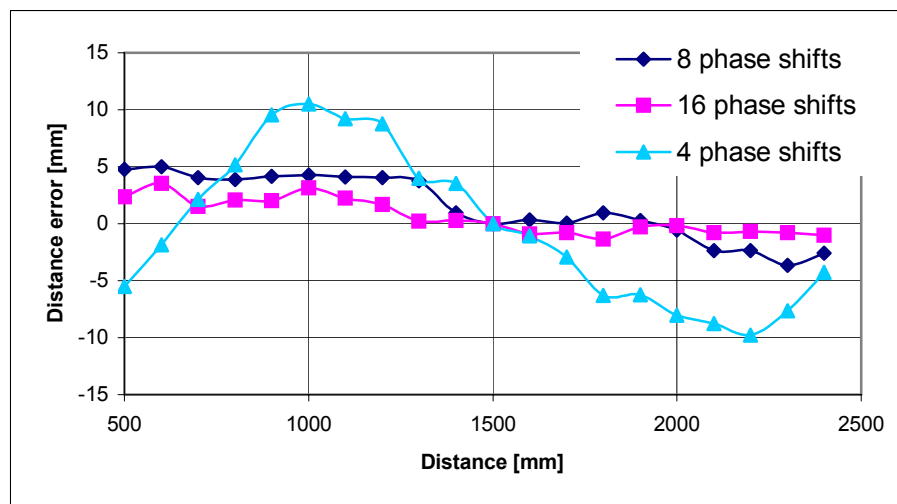
curve induced by the non-linearity of the system normally vanish very quickly, the phase shifting technique of less than 8 steps can satisfy the requirement in most 3D applications. **Fig. 6.5** shows the measurement results over a range of nearly two meters, using 4, 8 and 16 phase shifting evaluation algorithms respectively, based on an early developed 1D PMD ranging system with strong non-linear distortion and system noise of about 0.25mV rms. The modulation contrast of the PMD pixel was about 22%. A 12Bit-AD converter was used. The laser diode outputs a maximum optical power of 1mW at $\lambda=635\text{nm}$. The measurement result coincides very well with the simulation under the same condition. One can see that the evaluation with 8 phase shifting steps has considerably compensated the errors induced by the non-linearity and achieved satisfied result.

Table 6.1 The Influence of high orders of harmonics on the data evaluation [Xu-1]

N Phase step number	$\Delta\psi_k$ Phase step	Orders of harmonics											
		✓: Harmonic contributes to the data evaluation 0: Harmonic does not affect the data evaluation											
		1	2	3	4	5	6	7	8	9	10	11	12
3	$2\pi/3$	✓	✓	0	✓	✓	0	✓	✓	0	✓	✓	0
4	$2\pi/4$	✓	0	✓	0	✓	0	✓	0	✓	0	✓	0
5	$2\pi/5$	✓	0	0	✓	0	✓	0	0	✓	0	✓	0
6	$2\pi/6$	✓	0	0	0	✓	0	✓	0	0	0	✓	0
7	$2\pi/7$	✓	0	0	0	0	✓	0	✓	0	0	0	0
8	$2\pi/8$	✓	0	0	0	0	0	✓	0	✓	0	0	0
9	$2\pi/9$	✓	0	0	0	0	0	0	✓	0	✓	0	0
10	$2\pi/10$	✓	0	0	0	0	0	0	0	✓	0	✓	0



(a)



(b)

Fig. 6.5 The measurement results using 4-, 8- and 16-phase shifting evaluation algorithm. (a) The measured distance using corresponding evaluation algorithms. (b) The evaluation error based on different algorithm. Target: white paperboard. $T_{int} = 2.5\text{ms}$. $f_{mod} = 20\text{MHz}$. PMD chip: STP20-2F-No.7-T2. $K_{PMD} \approx 22\%$.

6.4 3D data calibration

For an 3D ranging camera, the measured distance value of each pixel in the sensing matrix corresponds to the distance from the related pixel $P'(u, v)$ to the point $P(x, y, z)$ of

the 3D scene through the focal center C of the lens, as shown in **Fig. 6.6**. Generally, we understand the distance of each point on the target as the distance of that point perpendicular to the sensing matrix of the 3D ranging cameras which is usually located in the focus plane of the lens system. The depth error from the real depth information of a point off the optical axis grows with the increasing distance. Therefore, it is necessary to calibrate the measured data for a correct representation of the 3D scene.

Neglecting the optical aberration effect of the lens and the triangular effect due to geometrical location of the source of illumination which is reasonable for measurement in the far field, the relationship between the point $P(x, y, z)$ on the target scene and its image $P'(u, v)$ at the focus plane can be described through the transformation between the so called world coordinate system and the image coordinate system. As illustrated in **Fig. 6.6**, the origin of the camera coordinate system is chosen in the focal center of the lens system with its xy -plane parallel to the uv -plane of the sensor coordinate system. The z -axes of both coordinate systems are located in the optical axis. The relationship can be then written as

$$\frac{f}{z} = \frac{u}{x} = \frac{v}{y} \quad (6.3)$$

which can be rewritten linearly as

$$\begin{bmatrix} s \cdot u \\ s \cdot v \\ s \end{bmatrix} = \begin{bmatrix} f & 0 & 0 & 0 \\ 0 & f & 0 & 0 \\ 0 & 0 & 1 & 0 \end{bmatrix} \begin{bmatrix} x \\ y \\ z \\ 1 \end{bmatrix} \quad (6.4)$$

where f is the focal length of the optical system and $s \neq 1$. For a camera coordinate system which is centered usually at one of the corners of the sensing array, say the left bottom corner, the parameters in the old system can simply be transformed into the new system through

$$\begin{bmatrix} s \cdot u' \\ s \cdot v' \\ s \end{bmatrix} = \begin{bmatrix} -f & 0 & u_0 & 0 \\ 0 & -f & v_0 & 0 \\ 0 & 0 & 1 & 0 \end{bmatrix} \begin{bmatrix} x \\ y \\ z \\ 1 \end{bmatrix} \quad (6.5)$$

in which (u_0, v_0) is the position in the old coordinate system. For the simplicity we still use the relationship defined by equation 6.4 for the following discussion. It is apparent that the depth information of the point $P(x, y, z)$ corresponds the z -value and the distance between the sensing plane and the focal plane, i.e. the focal length f . Since the measured distance $l_{x,y}$ is the distance from point $P'(u, v)$ through the focal center C to point $P(x, y, z)$, the corresponding real distance $d_{x,y}$ can be then described by

$$d_{x,y} = \left(l_{x,y} - \sqrt{u^2 + v^2 + f^2} \right) \cdot \cos \alpha \quad (6.6)$$

where α defines the angel between \overline{OP} and the z - axis, which can be calculated according to the pixel coordinates (u, v)

$$\alpha = \arctg \left(\frac{f}{\sqrt{u^2 + v^2}} \right) \quad (6.7)$$

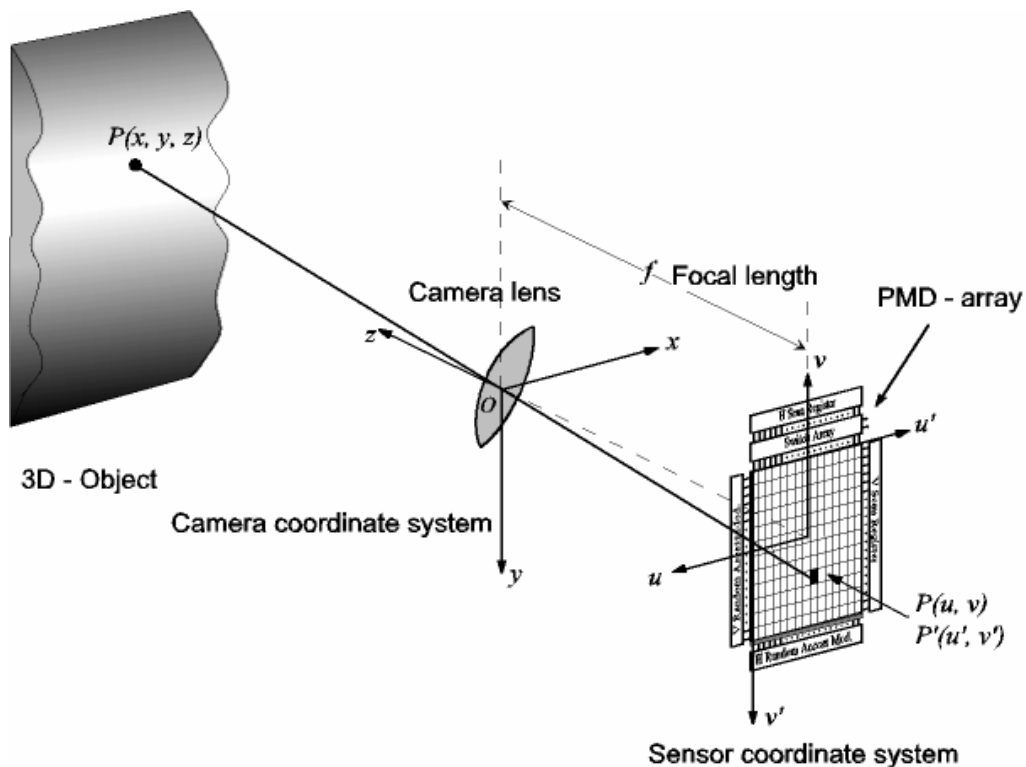


Fig. 6.6 The camera model for 3D-data calibration

6.5 Smearing effect and the depth of field

In the view of the optical imaging, for a TOF PMD ranging system, the modulated light transmitted from the light source which is reflected by the object surface is focused by a lens system to a light spot with size d_{img} at the PMD chip. It is apparent that both the size and the position of the object image varies with the changes of the distance of the object to the ranging system due to the following factors: geometrical arrangement of the light source and the receiver, focusing range of the lens system and lens aberration. For an 1D ranging system, the induced lateral and longitudinal shift and size variation of the light spot means merely the fluctuation of the received optical power. In the case of 3D PMD ranging system, however, this will cause smearing of the depth information at some PMD pixels, since a PMD pixel mixes in principle all the received optical components reflected from the target. This can be explained by following equation

$$I(\bar{t}_d) = \sum \Gamma_i [1 + M_i \cos(2\pi f_0 t_{d,i})] \quad \text{for } i = 1, 2, 3, \dots \quad (6.8)$$

As the result of correlation, the output of PMD contains not only the depth information of area that should be imaged to the PMD pixel but also the terms from the neighborhoods due to the optical aberration if part of 3D scene is not really sharp focused. **Fig. 6.7** shows the measured cross section of a box made of white paperboard by a 2D PMD line ranging system described in last chapter. The object was located in the position so that part of the object surface was out of depth of field of the camera. One can see that the measured depth information on the sharp edge of the box is smeared due to the problems discussed above. This example shows how important is the depth of field of the lens system for 3D ranging system as it is in case of 2D imaging sensors. As illustrated in **Fig. 6.8**, the depth of field for a given optical system with focal length f , lens aperture D_L and the pixel size d_{pixel} is defined by equation

$$\Delta g = g_0 \cdot f^2 \cdot \left[\frac{1}{f^2 + F\# \cdot d_{pixel} \cdot (g_0 + f)} - \frac{1}{f^2 - F\# \cdot d_{pixel} \cdot (g_0 + f)} \right] \quad (6.9)$$

where $F\# = f/D_L$ defines the f -value of the lens and g_0 the object distance at sharp focusing.

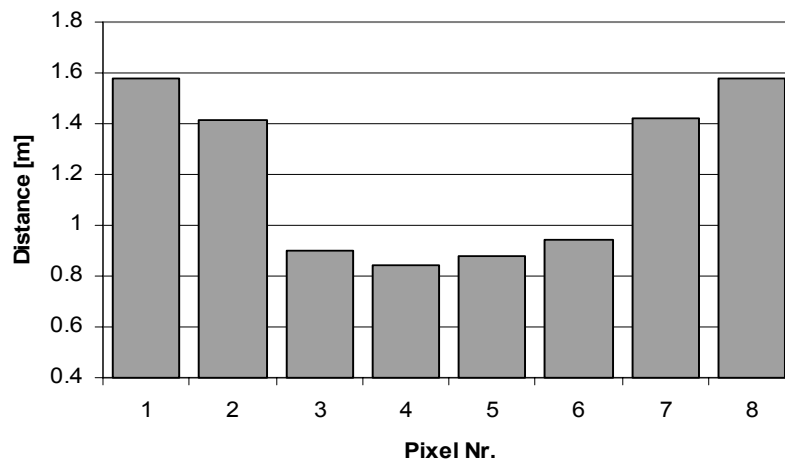


Fig. 6.7 The measurement error of depth information due to the insufficient depth of field of the applied objective in a PMD line sensor. The measured edge of the test object is therefore smeared.

From equation 6.9 we can see that the depth of field Δg is a term dependent of the focal length, entrance pupil of the objective and the pixel size in the sensing array. For a large depth of field Δg usually small lens aperture or large focal length, in other words, large f -value is necessary. However, for our purpose the lens system with large entrance pupil if possible is always desired in order to receive more optical power. Therefore, one should give special consideration for the lens system in the 3D TOF ranging system design depending on the requirement of single 3D applications.

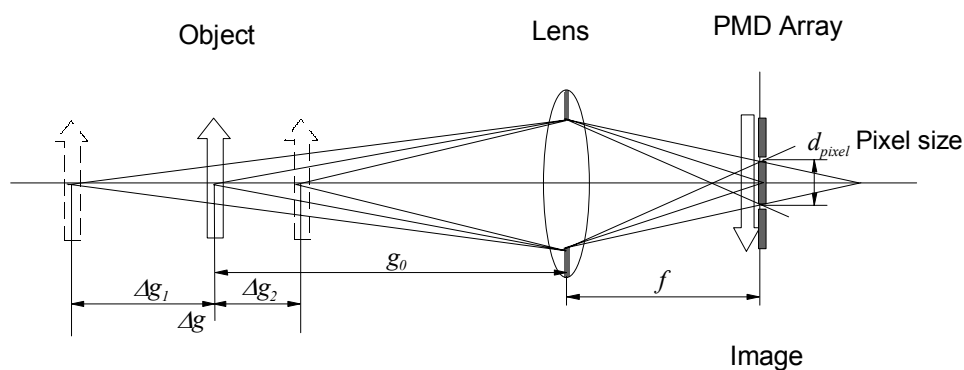


Fig. 6.8 Depth of field in a camera system with focal length f and pixel size d_{pixel} .

6.6 Discussion

We discussed in this section the main factors which influence the measurement accuracy of the PMD ranging cameras and the 3D data calibration for the correct reconstruction of the 3D scene. Large modulation contrast of PMD contributes to higher measurement accuracy of distance. The background illumination, on the other hand, restricts the distance resolution, which must be suppressed any way. The realization of PMD with on-chip SBI unit ensures the maximum dynamic range of PMD nearly independent of the background illumination. Similarly to other TOF ranging systems, the referencing technique is also necessary for the PMD ranging systems to compensate the drift errors and other errors induced through variation of system parameters as well. However, the implementation of the referencing technique can be, due to the unique features of PMD, considerably simplified. The multi-phase shifting evaluation algorithm averages not only the influence of noise improving further the measurement accuracy but suppresses substantially the errors caused by the non-linearity problem of the system. The more the phase shifts are applied for evaluation, the stronger is the suppression of non-linearity error and the more time is needed for one measurement. In practice, 4- or 8- phase shifting evaluation technique are widely accepted in the measurement.

7 Summary and perspective

In this thesis we have investigated the performance of the PMD device as electro-optical mixer and realization of different solid PMD ranging sensors for 1D-, 2D- as well as 3D-measurement based on the phase shifting modulation technique.

We give first at the beginning of this work an overview of the different range measurement techniques, their corresponding advantages and drawbacks and the typical applications in distinct industrial areas. Furthermore, as the main time-of-flight (TOF) ranging technique used in this work, the phase shifting modulation technique (homodyne mixing technique) and the related range evaluation method are discussed more in details.

With permanently increasing demands for 3D-data acquisition in the industry more and more new 3D ranging systems based on the techniques discussed in chapter two have been developed. As one of the most important measurement techniques, the new non-scanning optical 3D-ranging systems based on time-of-flight are nowadays intensively investigated. The key component of such 3D ranging systems is the 2D electro-optical mixer. The typical drawbacks of many 2D EO-mixer based ranging systems such as high operation voltage, system complexity and high cost restrict their applications in the industry. A new novel 2D-mixer concept – Photonic Mixer Device (PMD) – based on the creative idea from Prof. R. Schwarte opens a complete new area in the 3D-sensing technique. Realized on the basis of standard CMOS technology, the PMD device overcomes nearly most drawbacks of the traditional distance measurement systems and brings us a new generation of extremely fast, robust and low-cost 3D solid state ranging systems. In chapter three we described the typical structure and the operation principle of CMOS-PMD followed by a brief discussion about the features of PMD device.

In chapter 4 we reported the experimental investigation of performance of PMD device realized in different structures. As the measurement results showed, the investigation confirmed all the expectations and simulations in a series of preceding researches [Bux-1][Scw-4][Xu-1]. The PMD test pixels have shown a large linearity area in the middle of transfer characteristic and needed very low modulation voltage of merely about 500 ~

600 mV (peak to peak), in contrast to up to 1000V in the case of Pockels cell. With the further optimization of PMD design the properties of PMD device has considerably improved. Although the optimized short channel PMD finger structure has relative lower modulation contrast than the typical long channel 2-gate PMD pixel, it demonstrated very exciting performance in the high modulation frequencies. We have measured the 3dB modulation frequency bandwidth of the short channel PMD finger structure better than 100MHz at 3nA photo current, compared to only about 2MHz by the 2-gate long channel PMD pixel. The finger structure PMD showed very low lateral sensitivity as well. We have measured a dynamic range of better than 70dB with very low dark current of about 0.13pA at room temperature. The PMD pixel has demonstrated still astonishing good modulation performance at very weak optical illumination (in the order of some pA) as well as significant anti-interfering effect due to its unique feature of correlated balance sampling (CBS).

We presented in chapter five the development of PMD ranging systems based on different actually fabricated PMD chips. The advantageous properties of the PMD considerably simplify the realization of 3D ranging systems and make the modular system design of 3D imaging sensors possible. With the same functional modules one can easily implement 1D, 2D as well as 3D ranging sensors based on corresponding PMD chips for different applications. The practice has demonstrated also from the point of view of engineering the outstanding ability of PMD. Based on an PMD pixel fabricated in the third chip design, we have reached an distance accuracy of the PMD ranging system up to 1.5mm with the modulation frequency of only 16.25MHz and 12bit A/D converter, without any further data processing. Compared to the low PMD noise level, the system noise is rather more important for the improvement of ranging accuracy. We discussed in the last chapter some problems that will influence the measurement precision of PMD ranging systems and the considerations for further improvement.

In the dissertation my work focused on the experimental investigations of performance of PMD device and deals with merely the 3D PMD ranging systems based on the phase shifting modulation technique. As already mentioned in the discussions in this paper, a variety of other ranging techniques can also be used in the range measurement based on the PMD device, e.g. PMD-PLL and PMD-DLL laser ranging systems [Bux-2][Rin-1].

3D data acquisition based on PMD is just only one of the possible applications of PMD device. Due to its outstanding correlation functionality, PMD is also suitable for configuration of optical interfaces in the communication technique. It is reasonable to expect that the PMD could find more and more industrial applications in the future.

Whatever the applications of PMD in the industry, one thing is beyond any doubt: the novel PMD concept has opened us a complete new area in the micro sensorial technique. We convince ourselves that with the continuous development of the modern semiconductor technology and further optimization of PMD design the dream of high quality, high performance, low cost and high robust 3D ranging cameras and other applications based on PMD technology, similar the CCD imaging sensors nowadays, will not so far from our lives.

References

- [Boy] W. Boyle, G. E. Smith, Charge coupled semiconductor devices. Bell Syst. Tech. Jour., Vol. 49, pp. 587-593, 1970.
- [Bre-1] B. Breuckmann, Bildverarbeitung und optische Meßtechnik in der industriellen Praxis. München: Franzis-Verlag, 1993
- [Bre-2] B. Breuckmann, Grundlagen der bildgebenden optischen 3D-Meßtechnik. Tagungsunterlagen Aktuelle Entwicklungen und industrieller Einsatz der Bildverarbeitung. S. 247ff, Aachen, MIT Management 1996
- [Bux-1] B. Buxbaum, R. Schwarte, Z. Xu, T. Ringbeck, H. Heinol, J. Schulte, W. Tai, Z. Zhang, X. Luan, J. Fricke, Charge Transfer Simulation in PMD-Structures. Sensor 99, 1999.
- [Bux-2] B. Buxbaum, R. Schwarte, T. Ringbeck, X. Luan, Z. Zhang, Z. Xu, H. Heß, Synchronization in Spread Spectrum Laser Radar Systems based on PMD-DLL, SPIE's 14th Annual International Symposium: Aero Sense 2000, 24.-28. April 2000 · Orlando, USA.
- [Bux-3] B. Buxbaum, R. Schwarte, T. Ringbeck, H. Heinol, Z. Xu, J. Olk, W. Tai, Z. Zhang, X. Luan, A new approach in optical broadband communication systems: A highly integrated optical phase locked loop based on a mixing and correlating sensor, the Photonic Mixer Device (PMD). OPTO 98, pp. 59-64, Erfurt 1998.
- [Bux-4] B. Buxbaum, R. Schwarte, T. Ringbeck, PMD-PLL: receiver structure for incoherent communication and ranging systems. SPIE – Photonics East 99.
- [Bux-5] B. Buxbaum, R. Schwarte, T. Ringbeck, M. Grothof, X. Luan, MSM-PMD as correlation receiver in a new 3D-ranging system, SPIE- Laser Radar Techniques, Remote Sensing 2001, Toulouse 2001.
- [Can] J. Canny, A computational aproach to edge detection, IEEE Trans. on Pat. Ana. Mach. Intell., Vol. PAMI-8, pp 300-331, 1986.
- [Dän] R. Dändliker, K. Hug, J. Politch, E. Zimmermann. High accuracy distance measurements with multiple-wavelength interferometry. Optical Engineering, Vol. 34, No. 8, p 2407, 1995.
- [DoHä] R. G. Dorsch, G. Häusler, J. M. Herrmann, Laser triangulation: fundamental uncertainty in distance measurement. Applied Optics, Vol. 33, No. 7, 1 March 1994.
- [Dor] R. G. Dorsch *et al*, Laser triangulation: fundamental uncertainty in distance measurement. Applied Optics, Vol. 33, pp1306-1314, 1994.
- [DrHä] T. Dresel, G. Häusler, H. Venzke, Three-dimensional sensing of rough surfaces by coherence radar. Applied Optics, Vol. 31 No.7, 1 March 1992

-
- [Eng] K. Engelhardt, Methoden und Systeme der optischen 3D-Meßtechnik. Ingenieurvermessung '92. Beiträge zum XI. Internationalen Kurs für Ingenieurvermessung (Zürich), S. II 1/1-II 1/12, Bonn: Ferd. Dümmler Verlag, 1992
- [Faug] O. Faugeras, Three-Dimensional Computer Vision – A Geometric Viewpoint. The MIT Press, 1993.
- [Fos] E. Fossum, Active Pixel Sensors: Are CCDs Dinosaurs?, Proceedings of the SPIE, Vol. 1900, pp. 2-14, 1993.
- [Frk] J. U. Fricke, Halbleitertechnische Modellbildung (MEDICI), Analyse und Beschreibung zum Photomischdetektor (PMD)-Korrelationspixel einer 3D-Festkörperkamera, Diplomarbeit, University of Siegen, 1998
- [Gru] A. Gruen, H. Kahmen. Optical 3D-measurement techniques II- Wichmann-Verlag, Karlsruhe, 1993.
- [He-1] H. Heinol, Untersuchung und Entwicklung von modulationslaufzeitbasierten 3D-Sichtsystemen, PhD thesis, to be published, Siegen, 2001
- [He-2] H. Heinol, Z. Xu, R. Schwarte, T. Ringbeck, Elektrooptische Korrelationseinheit großer Apertur zur schnellen 3D-Objektvermessung: Experimentelle Ergebnisse, Tagungsband DGZfP/GMA -Optische Formerfassung, VDI/VDE-GMA, Langen 1997
- [He-3] H. Heinol, Z. Xu, R. Schwarte, J. Olk, R. Klein, Electro-optical correlation arrangement for fast 3D cameras: properties and facilities of this electro-optical mixer device, SPIE-EOS – Sensors, Sensor Systems, and Sensor Data Processing, München, 1997
- [HoLu] G. R. Hopkinson and D. H. Lumb, Noise reduction techniques for CCD image sensors, Journal Phys. E. Sci. Instrum, vol. 15, p. 1214, 1982.
- [Ins] Instrument systems: Spectro 320 Universal spectrum analyser, User handbook, 1994
- [Kle] R. Klein, Ein laseroptisches Entfernungsmeßverfahren mit frequenzvariabler Pseudo-Noise-Modulation, PhD thesis, Siegen 1993
- [Kra] J. Kramer, Photo-ASICs: Integrated optical metrology systems with industrial CMOS Technology. Ph.D. Dissertation ETH Zurich, Switzerland, No. 10186, 1993
- [Lan] R. Lange, 3D Time-Of-Flight distance measurement with custom solid-state imaging sensors in COMS/CCD-technology, Dissertation, Universität-GH-Siegen, 2000
- [Li] J. Li, Rauschoptimierung von Laserentfernungsmeßsystemen unter besonderer Berücksichtigung einer laufzeitvariablen PN-Modulation, Dissertation an der Universität GH Siegen, Fachbereich Elektrotechnik und Informatik, 1995.

- [Lim] J. S. Lim, Two-dimensional signal and image processing, PTR Prentice-Hall, Inc., New York, 1990
- [Luhm] T. Luhmann, Digitale Photogrammetrie in der 3D-Industriemesstechnik, 10. Heidelberger Bildverarbeitungs Forum, Siegen, 1999.
- [Malz] R. Malz. Codierte Lichtstructures für 3D-Messtechnik and Inspektion. Thesis, Institute for Technical Optics, University of Stuttgart, Germany, 1992.
- [Mar] M. Maron, Numerical Analysis – A practical Approach, Macmillan Publishing Co., Inc., 1982
- [Miya] R. Miyagawa, T. Kanade, CCD-Based Range-Finding Sensor, IEEE Transactions on Electron Devices, Vol. 44, No. 10, pp1648-1652, 1997.
- [NiSa] H. Nicholas and H. Samuelli, An Analysis of the Output Spectrum of Direct Digital Frequency Synthesizers in the Presence of Phase-Accumulator Truncation, 41th Annual Frequency Control Symposium, 1987.
- [OFHB] Handbuch OF 1, Verfahren für die optische Formerfassung. Deutsche Gesellschaft für zerstörungsfreie Prüfung e.V. DGZfP, 1.HE11/95, 1995
- [Olk] J. Olk, Untersuchung von Laufzeitentfernungsmesssystemen unter besonderer Berücksichtigung des Referenzproblems, ZESS Forschungsberichte, Band 5, Shaker-Verlag, Universität-GH Siegen 1997.
- [Raz] B. Razavi, Monolithic Phase-Locked Loops and Clock Recovery Circuits, IEEE Press, New York, 1996.
- [Rin-1] T. Ringbeck, B. Buxbaum, A highly integrated monolithic electro-optical PLL in CMOS-technology (PMD-PLL) for communication and ranging systems, Opto'2000 – 4th International Conference on Optoelectronics, Optical Sensors & Measuring Techniques, Erfurt 2000
- [Rin-2] T. Ringback, R. Schwarte, B. Buxbaum, X. Luan, W. Tai, Z. Zhang, A new Opto-electrical Phase Locked Loop for Phase / Frequency Detection in Rotation and Range Measurement Applications, Sensor 2001
- [Sal] B. Saleh, Fundamentals of Photonics, ISBN 0-471-83965-5, John Willey & Sons, 1991
- [ScI] J. Schulte, Intelligente Bildsensoren in TFA-Technologie am Beispiel eines Äquidensitätenextraktors, Dissertation, University of Siegen, Fachbereich Elektrotechnik und Informatik, 1995.
- [Scm] J. Schmitt, K. Creath, Extended averaging technique for derivation of error-compensation algorithms in phase-shifting interferometry, Applied Optics, Vol. 34, No. 19, 1995

-
- [Scu] E. Schubert. Mehrfachfarbcodierte Triangulationsverfahren zur topometrischen Erfassung und Vermessung von 3D-Objekten. Dissertation am ZESS der Universität-GH Siegen, 1996.
- [Scw-1] R. Schwarte, Principle of 3-D imaging techniques, Handbook of computer vision and applications. B. Jähne, H. Haussecker and P. Geissler (Eds.), Academic Press, 1999
- [Scw-2] R. Schwarte. Überblick und Vergleich aktueller Verfahren der optischen Formerfassung. DGZfP-GMA-Fachtagung in Langen, 1997
- [Scw-3] R. Schwarte, H. Heinol, Z. Xu, A New Fast, Precise and Flexible 3D-Camera Concept Using RF-Modulated and Incoherent Illumination, Kongreßband SENSOR 95, AMA Fachverband für Sensorik, pp. 177-182, Nürnberg 1995.
- [Scw-4] R. Schwarte, H. Heinol, Z. Xu, K. Hartmann, A new active 3D-Vision system based on rf-modulation interferometry of incoherent light, SPIE -Intelligent Robots and Computer Vision XIV, Vol. 2588, pp. 126-134, Philadelphia 1995.
- [Scw-5] R. Schwarte, Z. Xu, H. Heinol, J. Olk, B. Buxbaum, New optical four-quadrant phase-detector integrated into a photogate array for small and precise 3D-cameras, SPIE-Multimedia Processing and Applications: Three-Dimensional Image Capture, Vol. 3023, pp. 119-128, San Jose, 1997
- [Scw-6] R. Schwarte, Z. Xu, H. Heinol, J. Olk, R. Klein, B. Buxbaum, H. Fischer, J. Schulte, A new electrooptical Mixing and Correlating Sensor: Facilities and Applications of this Photonic Mixer Device (PMD), SPIE-EOS: Sensors, Sensor Systems, and Sensor Data Processing, Vol. 3100, S. 245-253, München 1997.
- [Scw-7] R. Schwarte, Dynamic 3D-Vision, IEEE Int. Symp. on Electron Devices for Microwave and Opto-electronic Applications, EDMO 2001, Wien
- [Spi] T. Spirig, P. Seitz, O. Vietze, F. Heitger, The Lock-In CCD – two dimensional synchronous detection of light, IEEE Journal of Quantum Electronics, Vol. 31, No. 9, pp 1705-1708, 1995
- [S-TEC] S-TEC GmbH: PMD Research Report, Siegen, 1999
- [Sze] S. Sze, Physics of semiconductor device, 2nd edition, John Wiley & Sons, 1981
- [Tai] W. Tai, Untersuchungen von 3D-PMD-Kameras unter besonderer Berücksichtigung der optischen Optimierung, Dissertation, Universität-GH-Siegen, Shaker Verlag, 2000
- [Teu] A. Theuwissen, Solid-State Imaging with Charge-Coupled Devices, *Kluwer Academic Publishers*, (1995).
- [Vie] O. Vietz, Active pixel image sensors with application specific performance based on the standard silicon CMOS processes, PhD thesis, ETH Zurich, 1997.

- [Wahl] F. M. Wahl, A coded light approach for depth map acquisition. Proc. DAGM-Symposium Mustererkennung 1986, Informatik-Fachberichte, Springer-Verlag, 1986.
- [WeGu] H. M. Wey and W. Guggenbühl, An improved correlated double sampling circuit for low noise charge-coupled devices, IEEE Transactions on Circuits and Systems, vol. 37, pp. 1559–1565, Dezember 1990.
- [Wolf] H. Wolf, Getting 3D-Shape by coded light approach in combination with phaseshifting. Numerisation 3D/Human Modelling, Salon et Congress sur la Numerisation 3D, Paris, 1997.
- [Xu-1] Z. Xu, Investigation of 3D-Imaging Systems Based on Modulated Light and Optical RF-Interferometry (ORFI) – ZESS – Forschungsberichte, Shaker Verlag Aachen, ISBN 3-8265-6736-6, 1999.
- [Xu-2] Z. Xu, H. Heinol, R. Schwarte, O. Loffeld, An Enhanced Multi-probing Recovering Algorithm Based on Color Mixed Non-linear Modulation and its Application in a 3D-Vision System. SPIE -Intelligent Robots and Computer Vision XIV, Vol. 2588, pp. 200-207, Philadelphia 1995.
- [Zim] M. Zimmer, Neues Verfahren zur Phasen/Digital-Umsetzung. Elektronik, pp. 58-64, Vol. 12, 1989.